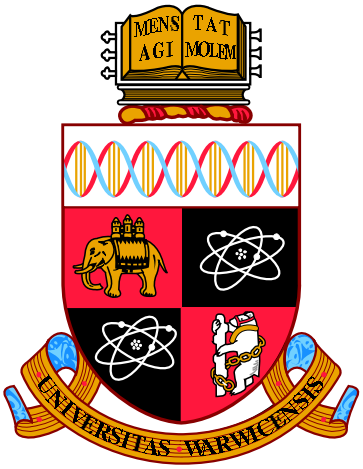

Observation of the decay $B^0 \to \bar{D}^0 K^+ K^-$ with the LHCb detector at CERN

by

Mark Whitehead

Thesis

Submitted to the University of Warwick

for the degree of

Doctor of Philosophy

Department of Physics

June 2012

THE UNIVERSITY OF WARWICK

Contents

List of Tables

List of Figures

Acknowledgments

Firstly, I would like to thank my supervisor, Tim Gershon, for all of his help, ideas and support over the past years. I am also thankful for his careful reading of this document over the past year and for giving me the opportunity to work in such an exciting field of physics. I also owe a great debt to my second supervisors Paul Harrison and Michal Kreps, the former for getting me started in the LHCb collaboration and the latter for help with `NeuroBayes` and reading and commenting on this document. A massive thank you is reserved for Tom Latham for all of his expert help, I'd certainly not be half the researcher that I am today without his limitless patience. I thank Anton Poluektov for his help and guidance when I was just starting the analysis presented here. Thank you to the rest of the Warwick LHCb group, John Back and my fellow students Matt, Dave, Matt, Tom, Dan and Rafael for the fun times and knowledge that we have shared.

Secondly I would like to thank the members of the LHCb collaboration for their dedication and expertise that made my analysis possible. In particular I'd like to thank Gloria Corti and Patrick Robbe for their help, patience and belief in me. I reserve a special mention for the ladies of the UK liaison office at CERN. Without the help of Celine Le Bon and Mary Elizabeth Shewry I would never have made it to Geneva.

My eternal gratitude goes to my wonderful parents, Miles and Angela, for helping me to get to this point in my life. Thank you so much for your love, support and enduring belief in me. Thank you also to my twin brother, best friend, and partner in crime, Leigh for all that you have done for me over the years. I also thank my wonderful girlfriend, Emma, for all of the help and support over the last

couple of years and for making my time in Geneva special. Finally, a quick thank you goes to the lads from Kent, you know who you are.

I would like to dedicate this work to my departed grandparents Violet Whitehead and Peter Hatfull. I'm sorry that you couldn't be here to share this journey.

Declarations

The work presented in this thesis is all of my own work, unless it is specifically referenced to the contrary. This thesis has not been submitted, in any form, to this or any other university for another qualification.

Mark Whitehead

Abstract

The first observation of the decay mode $B^0 \to \bar{D}^0 K^+ K^-$ is presented using 0.62 fb^{-1} of data collected by the LHCb detector in 2011. The branching fraction is measured with respect to the topologically similar decay mode, $B^0 \to \bar{D}^0 \pi^+ \pi^-$. The ratio of branching fractions is measured to be

$$\frac{\mathcal{B}\left(B^0 \to \bar{D}^0 K^+ K^-\right)}{\mathcal{B}\left(B^0 \to \bar{D}^0 \pi^+ \pi^-\right)} = 0.056 \pm 0.011 \pm 0.007,$$

where the first uncertainty is statistical and the second is systematic. Using the world average value for the denominator yields

$$\mathcal{B}\left(B^0 \to \bar{D}^0 K^+ K^-\right) = (4.7 \pm 0.9 \pm 0.6 \pm 0.5) \times 10^{-5},$$

where the third uncertainty is from $\mathcal{B}\left(B^0 \to \bar{D}^0 \pi^+ \pi^-\right)$. Secondly, evidence for the $B_s^0 \to \bar{D}^0 K^+ K^-$ decay mode is presented. The branching fraction ratio with respect to $B^0 \to \bar{D}^0 K^+ K^-$ is found to be

$$\frac{\mathcal{B}\left(B_s^0 \to \bar{D}^0 K^+ K^-\right)}{\mathcal{B}\left(B^0 \to \bar{D}^0 K^+ K^-\right)} = 0.90 \pm 0.27 \pm 0.20,$$

where the first uncertainty is statistical and the second is systematic.

Preface

The Standard Model of particle physics is a great success of modern science. It describes a wide range of particle interactions and processes to excellent precision. However, it has become increasing clear that the Standard Model is not a complete theory. For example, evidence of *dark matter* by astronomers suggest that new particles must be present in the universe, but the Standard Model provides no excellent candidates for this dark matter. A second problem that is more relevant to this thesis is the dominance of matter over antimatter in the universe. The observed asymmetry between matter and antimatter is not fully described by the Standard Model. A process known as CP violation can explain a very small portion of this matter asymmetry, but more sources of CP violation must be found within or beyond the Standard Model.

The LHCb detector, based at the LHC at CERN, was designed to perform precise measurements of B hadron decays. This includes measurements of CP violation in both the beauty and charm sectors. The measurements presented in this thesis represent a starting point towards studies of CP violation in $B^0_{(s)} \to Dhh'$ decays. The focus of this thesis is on tree-level decays that are not sensitive to effects beyond the Standard Model. It is important to understand how much CP violation is included within the Standard Model before contributions from beyond it can be fully understood.

Chapter 1 provides an introduction to the Standard Model of particle physics and a detailed discussion of CP violation. The importance of studying $B^0_{(s)} \to Dhh'$ processes is also described. Following in Chapter 2 is an overview of the LHCb detector and the LHC accelerator complex. Discussion of the analysis begins in

Chapter 3 with details on the event selection used to create the final data samples of $B^0 \to \bar{D}^0\pi^+\pi^-$ and $B^0_{(s)} \to \bar{D}^0 K^+ K^-$ events. Chapter 4 covers the wide range of background studies that were performed to understand the origins of selected events. The fitting strategy used to extract the signal yields is described in Chapter 5. The results are presented in Chapter 6, which include a measurement of the $B^0 \to \bar{D}^0 K^+ K^-$ branching fraction and a branching fraction ratio of $B^0 \to \bar{D}^0 K^+ K^-$ and $B^0_s \to \bar{D}^0 K^+ K^-$. Sources of systematic uncertainties are considered in Chapter 7. A conclusion is provided in Chapter 8 to discuss the results and to look ahead to future prospects of similar studies. Finally, Appendix A is used to describe the simulation of the LHCb vertex detector geometry.

Chapter 1

Theory

1.1 The Standard Model

The Standard Model of particle physics is a quantum field gauge theory that describes how particles interact with each other via the strong, weak and electromagnetic interactions. It should be noted that gravitational effects do not enter the Standard Model due to the extremely weak effects they have on individual particles.

The Standard Model includes several fundamental particles, twelve of which are known as *fermions*, the six *leptons* and six *quarks*. The properties of the twelve fermions are summarised in Tab. 1.1. The fermions are arranged, by convention, into three generations, where generations two and three may be thought of as higher mass copies of the particles in generation one. For example, the muon has the same quantum numbers as the electron, but is a factor two hundred times more massive. All of the fermions have been observed in experiments, the top quark was the last quark to be discovered in 1995 at the Tevatron [1, 2]. The tau neutrino was the last lepton to be observed, discovered in 2000 by the Direct Observation of NU Tau (DONUT) experiment at Fermilab [3]. Every fermion in the Standard Model has an associated antiparticle that has the same mass but opposite quantum numbers, such as charge. The remaining fundamental particles are the gauge *bosons* that are responsible for mediating the three forces described by the Standard Model; weak, strong and electromagnetic. The gauge bosons are summarised in Tab. 1.2. Finally, there is one boson that has not yet been discovered experimentally, the Higgs boson. The Higgs is unique among Standard Model bosons because it is not associated with an interaction. Instead it is part of the Higgs mechanism [4], which allows particles to obtain mass.

Quantum electrodynamics (QED) is the theory that describes the interac-

Generation	Fermion	Electric charge	Mass (MeV/c^2)
I	Electron e	-1	0.510998910(13)
	Electron neutrino ν_e	0	Not known
	Up quark u	$+\frac{2}{3}$	$2.5^{+0.6}_{-0.8}$
	Down quark d	$-\frac{1}{3}$	$5.0^{+0.7}_{-0.9}$
II	Muon μ	-1	105.658367(4)
	Muon neutrino ν_μ	0	Not known
	Charm quark c	$+\frac{2}{3}$	1290^{+50}_{-110}
	Strange quark s	$-\frac{1}{3}$	100^{+30}_{-20}
III	Tau τ	-1	1776.82 ± 0.16
	Tau neutrino ν_τ	0	Not known
	Top quark t	$+\frac{2}{3}$	172900^{+600}_{-900}
	Bottom quark b	$-\frac{1}{3}$	4190^{+180}_{-60}

Table 1.1: The three fermion generations in the Standard Model. Masses are taken from the Particle Data Group (PDG) [5].

Gauge boson	Force	Mass (GeV/c^2)
Photon	Electromagnetic	0
Gluon	Strong	0
$W^\pm$	Weak (charged current)	80.399 ± 0.023
Z^0	Weak (neutral current)	91.1876 ± 0.0021

Table 1.2: The gauge bosons in the Standard Model. Masses are from Ref. [5]

tions of charged particles and was the subject of the 1965 Nobel prize for S. Tomonaga, J. Schwinger and R. P. Feynman [6]. Theories of the weak interaction, to describe beta decay and quark flavour changing decays, were ultimately united with QED. Unification of the two interactions was an excellent success for the Standard Model and the so called electroweak (EW) theory yielded the 1979 Nobel prize for S. L. Glashow, A. Salam and S. Weinberg [6] and the 1999 Nobel prize for G. t'Hooft and M. J. G. Veltman [6]. Quantum Chromodynamics, the theory of the strong force which acts on particles with colour charge, was the subject of the 2004 Nobel prize for D. J. Gross, H. D. Politzer and F. Wilczek [6].

All fermions may interact via the weak interaction and those with electric charge also via the electromagnetic interaction. However, quarks are the only fermions to feel the strong interaction because they have *colour* charge and the lep-

tons do not. Colour charge comes in three different types, *red*, *green* and *blue*. The opposite charges to these are simply anti-red, anti-green and anti-blue.

One feature of the strong force is that quarks may not exist as free particles, but instead are always bound in colourless combinations called *hadrons*. There are two types of hadrons, those with one quark and one anti-quark are called *mesons* and those with three quarks are known as *baryons*. This property is known as confinement and means that the amount of energy required to separate a pair of quarks becomes so large that another pair of quarks is created.

There are hundreds of hadrons that are known today, from the well known baryons; the proton(uud) and neutron(udd) to rarer states such as $\Omega_b^-(ssb)$. There are several groups of mesons; for example, light unflavoured, strange, charm and bottom. The groups come from the presence of; only u and d quarks, an s quark, a c quark and a b quark respectively. Strange, charm and bottom mesons are labelled K, D and B respectively. Extra subgroups can then be created by having, for example, c and s quarks to make charmed, strange mesons. Table 1.3 gives a summary of some common ground state mesons that appear throughout this thesis. Quantum numbers can be assigned based on the type of quarks present in a hadron, for example S is used to track the number of strange quarks. Note that the top quark does not hadronise because it decays before hadronisation can take place.

Group	**Meson**	**Mass (MeV/c^2)**
Light unflavoured	π^0	134.9766 ± 0.0006
	$\pi^\pm$	139.57018 ± 0.00035
Strange	K^0	497.614 ± 0.024
	$K^\pm$	493.677 ± 0.016
Charm	D^0	1864.83 ± 0.14
	$D^\pm$	1869.60 ± 0.16
Charmed, strange	$D_s^\pm$	1968.47 ± 0.33
Bottom	B^0	5279.50 ± 0.30
	$B^\pm$	5279.17 ± 0.29
Bottom, strange	B_s^0	5366.3 ± 0.6

Table 1.3: A summary of the ground-state pseudoscalar mesons from the most common meson groups. Masses are the current world average values from Ref. [5].

Despite being thoroughly tested over the last few decades some questions remain unanswered by the Standard Model. These include: Why is the universe dominated by matter? Why are there three generations of quarks and leptons?

Which particles can explain the presence of dark matter? The experiments at the LHC will, hopefully, test the Standard Model more precisely than ever before and expand our knowledge in all of these areas.

1.2 Charge-Parity violation

Charge-parity (CP) is the combination of two operators, charge conjugation (C) and parity (P). The C operator exchanges a particle for its own antiparticle and the P operator reverses all spatial coordinates. Both the strong and electromagnetic interactions conserve C and P independently.

Charge conjugation is maximally violated by the weak interaction. An example of this is that under charge conjugation a left-handed neutrino would become a left-handed anti-neutrino. Experimentally it is known that anti-neutrinos are right-handed, and since neutrinos only interact via the weak interaction then it must be maximally violated. For more details please see Refs. [7, 8].

Following the prediction from T.D. Lee and C.N. Yang [9], parity violation was first observed in 1957 by C.S. Wu et al. [10] by looking at the beta decay of polarised ^{60}Co nuclei. They found that there was an asymmetry in the angular distribution of electrons emitted by the nuclei between θ and $180^\circ - \theta$, where θ was the angle between the electron momentum and the spin of the nucleus. As with charge conjugation, parity is also maximally violated by the weak interaction. This can be explained by noting that the mirror image of a left-handed particle is right-handed and is therefore forbidden to be produced via the weak interaction.

Following the fall of C and P conservation by the weak interaction, it was thought that the combined CP operator would be conserved by all interactions. CP conservation implies that particles and antiparticles behave in identical ways.

In 1955 M. Gell-Mann and A. Pais [11] suggested that neutral kaons must be considered as a mixture of two particles, each with a distinct lifetime and decay modes. Previously, neutral hadrons belonged to two distinct groups under C operations; those like the π^0 that turn into themselves or those with distinct anti-particles such as the neutron. The neutron, however, has distinct states because the magnetic moment distinguishes between particle and anti-particle absolutely. The proposed neutral kaon states are now known as K_L and K_S, where the L stands for long and the S for short, describing the relative lifetimes of the states. This proposal was confirmed by Lande et al. [12] in 1956 with the observation of the long lived kaon, K_L. The short lived kaon, K_S, had been seen previously but the observation of a lifetime difference between the states was the proof that Gell-Mann and Pais had

been correct.

In 1964 the first evidence of CP violation was published by J.H. Christenson et al. [13]. The paper reports a search for the CP forbidden decay of the long lived neutral kaon, K_L, known to decay to the CP allowed three pion final state. CP violation would be observed if K_L was seen to decay to two pions. The kaon mass states, K_S and K_L, are defined as

$$|K_S\rangle = p|K^0\rangle + q|\bar{K^0}\rangle,\ |K_L\rangle = p|K^0\rangle - q|\bar{K^0}\rangle, \tag{1.1}$$

where p and q are scaling factors that would have equal magnitudes if there was no CP violation in the neutral kaon system. Note that p and q must obey the relation $|p|^2 + |q|^2 = 1$. In this case, K_S, the CP even state, is expected to decay to $\pi^+\pi^-$ because this is a CP even final state. The K_L on the other hand would be a CP odd state and so must not decay to the CP even final state of $\pi^+\pi^-$. If K_L were seen to decay to $\pi^+\pi^-$ then CP violation would be observed.

The experiment found evidence that the K_L could decay to the CP forbidden two pion final state, demonstrating that CP was violated at some small level. Figure 1.1 shows the angular distribution of $K_L \to \pi^+\pi^-$ candidates from the original paper, with a clear excess of two body events found at the kaon mass.

Violation of CP symmetry in the weak sector is, however, very small and is certainly many orders of magnitude away from explaining the matter-antimatter asymmetry in the universe [14]. Currently, CP violation is the only known method that could have generated such an asymmetry. It does, however, show that particles do behave differently to their antiparticles in some situations. New sources of CP violation from within the Standard Model or in theories beyond it must be found.

There are, in fact, several distinct types of CP violation which are summarised below.

1.2.1 Direct CP violation

Direct CP violation occurs when the decay rate of a particle is different to that of the CP-conjugate decay. In other words, for a B meson, $\Gamma(B \to f) \neq \Gamma(\bar{B} \to \bar{f})$. The set of amplitudes that contribute to the decay enter the total amplitude each with a strong phase, δ and a weak phase ϕ. A weak phase is defined as a phase that changes sign under CP and a strong phase is defined as a phase that does not change sign under CP. Given that only the weak phase changes sign under CP and

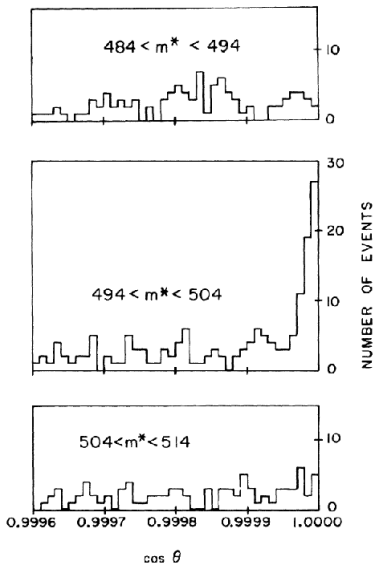

Figure 1.1: The angular distribution of two pion events in three mass ranges, below the kaon mass (top), around the known kaon mass (centre) and above the kaon mass (bottom). The central plot shows the discovery of the K_L decaying to the two pion final state with an excess of events at $\cos\theta = 1$ in the kaon mass region. The axis, $\cos\theta$, refers to the cosine of the angle between the momentum of the K_L and the sum of the momenta of the two pions. Reproduced from Ref. [13].

that the weak phases of f and B may be neglected, the ratio of amplitudes is:

$$\left|\frac{\bar{A}_{\bar{f}}}{A_f}\right| = \left|\frac{\sum_j |B_j| e^{i(\delta_j - \phi_j)}}{\sum_j |B_j| e^{i(\delta_j + \phi_j)}}\right|, \tag{1.2}$$

where $\bar{A}_{\bar{f}}$ and A_f are the amplitudes for the $\bar{B} \to \bar{f}$, $B \to f$ decays respectively, which are composed of contributing amplitudes, B_j, carrying strong and weak phases δ_j and ϕ_j. If two or more amplitudes with different weak and strong phases occur then the ratio of total amplitudes is not equal to one. This difference between the decay of matter and antimatter particles is called direct CP violation and it is the only mechanism for CP violation available to charged mesons.

1.2.2 Indirect CP violation

Indirect CP violation derives from mixing of neutral mesons, where the mass eigenstates are mixtures of CP eigenstates. Before considering CP violation, an overview of neutral meson mixing is shown below.

Neutral meson mixing

To illustrate the mixing mechanism the B^0–$\overline{B}^0$ system will be considered. Note that the same framework applies to other neutral meson systems. Figure 1.2 shows the two lowest order Feynman diagrams that contribute to neutral meson mixing in the B^0 system. Consider a state that is a superposition of states B^0 and $\overline{B}^0$ at time

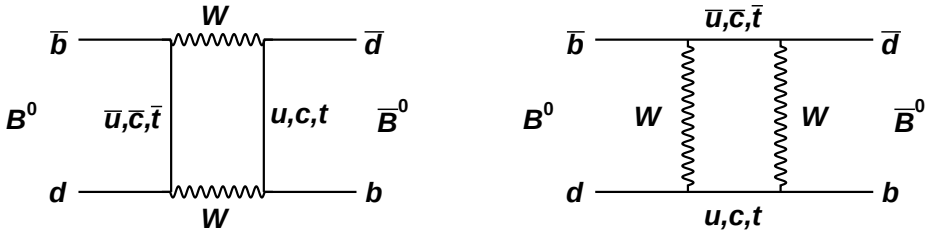

Figure 1.2: Feynman diagrams for $B^0 \to \overline{B}^0$ mixing.

$t = 0$,

$$|\psi(0)\rangle = a(0)|B^0\rangle + b(0)|\overline{B}^0\rangle, \tag{1.3}$$

where $a(0)$ and $b(0)$ are constants. The state ψ will evolve with time to include components for all possible decay modes f_n as

$$|\psi(t)\rangle = a(t)|B^0\rangle + b(t)|\overline{B}^0\rangle + c(t)|f_1\rangle + d(t)|f_2\rangle + \dots . \tag{1.4}$$

The interesting terms in this equation are those relating to the B meson states and not the f_n states. These may be neglected if the timescales of interest are much longer than the typical timescale of a strong interaction. This approximation is valid since the timescale of the strong interaction is many orders of magnitude shorter than the weak interaction. The time evolution of the state can be simplified to a 2×2 effective Hamiltonian [5],

$$H = M - \frac{i}{2}\Gamma\,, \tag{1.5}$$

where M and Γ are matrices associated with transitions of $(B^0, \overline{B}^0) \to (B^0, \overline{B}^0)$. Diagonal elements contain information of flavour conserving processes such as $B^0 \to B^0$ and non-diagonal elements detail flavour changing processes such as $B^0 \to \overline{B}^0$.

The physical eigenstates of H, B^0 and $\overline{B}^0$, can be specified in terms of mass eigenstates,

$$|B_L\rangle \propto p\sqrt{1-z}|B^0\rangle + q\sqrt{1+z}|\overline{B}^0\rangle \tag{1.6}$$

and

$$|B_H\rangle \propto p\sqrt{1+z}|B^0\rangle - q\sqrt{1-z}|\overline{B}^0\rangle\,. \tag{1.7}$$

Here B_L and B_H are the light and heavy mass states respectively. Complex parameters p, q and z are introduced to described the mixture of B^0 and $\overline{B}^0$ in the mass states. Note that in the absence of CP violation $z = 0$ and $|p|^2 + |q|^2 = 1$, as shown in Eq. 1.1.

Finally, two quantities can be defined to express the mass and decay width differences between the two mass states,

$$\Delta m = m_{B_H} - m_{B_L} \tag{1.8}$$

and

$$\Delta\Gamma = \Gamma_{B_H} - \Gamma_{B_L}\,. \tag{1.9}$$

Where m_{B_H} (m_{B_L}) is the mass of the heavy (light) state and Γ_{B_H} (Γ_{B_L}) is the decay width of the heavy (light) mass state.

CP violation in mixing

This is the type of CP violation seen in the neutral kaon system described in Sec. 1.2. CP violation from mixing is caused when $B^0 \to \bar{B}^0 \neq \bar{B}^0 \to B^0$. In other words, the number of B^0 mesons mixing to $\bar{B}^0$ is not equal to number of $\bar{B}^0$ mesons mixing to B^0. More formally, it occurs when $|p| \neq |q|$ and $z \neq 0$ in Eqs. 1.6 and 1.7. In the B^0 meson system this type of indirect CP violation is expected to be small because Δm_d is very small.

CP violation from interference of decays with and without mixing

A second type of indirect CP violation occurs from interference between decays of both particle and antiparticle to the same final state. Consider the following decay modes, $B^0 \to f_{CP}$ and $B^0 \to \bar{B^0} \to f_{CP}$, where f_{CP} is a CP eigenstate. Here, CP violation occurs due to interference between mixing and decay amplitudes. A parameter, $\lambda_{f_{CP}}$, is used to describe this interference and is defined as:

$$\lambda_{f_{CP}} = \frac{q\bar{A}_{f_{CP}}}{pA_{f_{CP}}}, \tag{1.10}$$

where $A_{f_{CP}}$ and $\bar{A}_{f_{CP}}$ are the decay amplitudes for $B^0 \to f_{CP}$ and $\bar{B^0} \to f_{CP}$ and p and q have the usual meanings. If both direct CP violation and CP violation in mixing for the given mode are zero then $|\lambda_{f_{CP}}| = 1$. However, a phase difference be-

tween the decay and mixing amplitudes can still cause CP violation since $\mathrm{Im}(\lambda_{f_{CP}})$ can be non-zero. In this case, the time dependent CP violation asymmetry, $a_{f_{CP}}$ is defined as:

$$a_{f_{CP}} = \mathrm{Im}\left(\lambda_{f_{CP}}\right) \sin\left(\Delta m t\right), \tag{1.11}$$

where Δm is the mass difference between the two mass states involved in the mixing and t is time. This type of CP violation has been measured in the B^0 system by the B factories [15, 16].

1.3 Quark mixing

1.3.1 Cabibbo and the Glashow-Illiopoulos-Maiani mechanism

The physical quark generations,

$$\begin{pmatrix} u \\ d \end{pmatrix}, \begin{pmatrix} c \\ s \end{pmatrix}, \begin{pmatrix} t \\ b \end{pmatrix}, \tag{1.12}$$

are not treated independently in the charged current weak interaction, so there is no conservation of quark generation.

The lepton sector is different, with no charged current interactions coupling leptons from one generation to another in the limit of zero neutrino mass. However, neutrinos do have non-zero masses, and the observation of neutrino oscillations [5] show that there is some coupling of generations in the lepton sector. This allows for charged current interactions to change a muon into an electron. However, the cross section for such a process is completely negligible given that it requires a neutrino to oscillate in a loop process. Neutrino oscillations are a long distance effect, so the probability of a neutrino oscillating inside a loop process is approximately zero. Charged current interactions across quark generations were shown by decays of the lightest kaons, ($K^{\pm}$), where the s quark decayed to a u quark.

In 1963, at a time when only three quarks; u, d and s, were known, Cabibbo [17] suggested that quark states, d' and s', that undergo the weak interaction, are defined as:

$$\begin{pmatrix} d' \\ s' \end{pmatrix} = \begin{pmatrix} \cos\theta_C & \sin\theta_C \\ -\sin\theta_C & \cos\theta_C \end{pmatrix} \begin{pmatrix} d \\ s \end{pmatrix}, \tag{1.13}$$

here the q' represent the rotated quark states that couple to the weak charged current, θ_C is the Cabibbo angle and the q are the physical quark states. The

rotated states that couple to the weak interaction can be written explicitly as:

$$d' = d\cos\theta_C + s\sin\theta_C, \tag{1.14}$$

$$s' = -d\sin\theta_C + s\cos\theta_C. \tag{1.15}$$

Experimentally, $\sin(\theta_C)$, is known to be approximately 0.2 which explains the observed suppression of $\Delta S = 1$ decays with respect to $\Delta S = 0$ decays. $\Delta S = 1$ simply means that an s quark has decayed to a quark of different flavour. This type of suppression is know as Cabibbo suppression and means that the decay of an s quark to a u quark is suppressed with respect to the equivalent $d \to u$ decay. For example,

$$\frac{\Gamma\left(K^+ \to \mu^+\nu_\mu\right)}{\Gamma\left(\pi^+ \to \mu^+\nu_\mu\right)} \propto \sin^2\theta_C, \tag{1.16}$$

shows the suppression of a $\Delta S = 1$ decay resulting from the Cabibbo suppression effect of the $K^+(u\bar{s})$ coupling to the W^+ compared with the $\pi^+(u\bar{d})$. The notation $\Gamma(X \to YZ)$ means the rate of particle X decaying to daughters Y and Z. It should be noted that Eq. 1.16 requires that phase space and helicity suppression corrections have to be included to allow for meaningful comparison to experiments.

Cabibbo's idea was extended into the Glashow-Illiopoulos-Maiani (GIM) mechanism [18] in 1970 which predicted the existence of the c quark. The motivation behind the GIM mechanism was to ensure that there were no $s \to d$ transitions that change quark flavour but not the charge of the quark to first order. The lack of observed decay rates showed that flavour changing neutral currents were either forbidden or heavily suppressed. The GIM mechanism explains, for example, the highly suppressed rate of the $K_L \to \mu^-\mu^+$ decay which is measured to be

$$\Gamma\left(K_L^0 \to \mu^+\mu^-\right) = (6.84 \pm 0.11) \times 10^{-9}. \tag{1.17}$$

The suppression of Eq. 1.17 occurs because this second order decay may proceed via $d \to u \to s$ and $d \to c \to s$ transitions, introducing factors $\cos\theta_C \sin\theta_C$ and $-\sin\theta_C \cos\theta_C$ respectively. If the predicted c quark had an identical mass to the u quark then this process would be forbidden as the amplitudes would cancel exactly. However, the mass difference allows the process at the observed heavily suppressed rate compared to the three quark model. Note that this argument ignores the small contribution of the top quark which was unknown at the time. It should also be noted that neither the Cabibbo theory nor the GIM mechanism incorporate CP violation.

1.3.2 Cabibbo-Kobayashi-Maskawa (CKM) matrix

A full explanation of the CP violation observed in the kaon system arrived in 1973 in the form of the Cabibbo-Kobayashi-Maskawa (CKM) matrix [17, 19]. Couplings of quarks to the charged current weak interaction are of the form

$$L_W = \frac{g}{2\sqrt{2}} \sum_{ij} \bar{U}_{L,i} \gamma^\mu D_{L,j} W_\mu^+ + h.c., \tag{1.18}$$

where U_L are left-handed up-type quark fields, D_L are left-handed down-type quark fields and i and j sum over the three quark generations. L_W is the Lagrangian density and the $h.c.$ notation means the equation also includes the Hermitian conjugate of the terms shown. Consider also the interaction between the quark fields and the Higgs field, ϕ. This relation, known as the Yukawa coupling [20], may be written as

$$L_Y = \sum_{ij} Y_{U,ij} \bar{Q}_{L,i} \phi U_{R,j} + \sum_{ij} Y_{D,ij} \bar{Q}_{L,i} \phi^* D_{R,j} + h.c., \tag{1.19}$$

where

$$Q_L = \begin{pmatrix} U_L \\ D_L \end{pmatrix}. \tag{1.20}$$

The terms Y_U and Y_D are the complex 3×3 Yukawa coupling matrices for up and down-type quark fields respectively. $U_{R(L)}$ and $D_{R(L)}$ are the right(left)-handed quark fields and ϕ is the doublet of Higgs fields. The quark mass terms appear in Eq. 1.19 once the Higgs field has a non-zero expectation value, this occurs when

$$\phi = \begin{pmatrix} 0 \\ \frac{v}{\sqrt{2}} \end{pmatrix}. \tag{1.21}$$

Using Eq. 1.19 and Eq. 1.21 it is straightforward to write down the mass terms for the up and down type quarks which are

$$M_U = \frac{v Y_U}{\sqrt{2}},\ M_D = \frac{v Y_D}{\sqrt{2}}, \tag{1.22}$$

where M_U is the up-type quark mass matrix and M_D the down-type mass matrix. So far the quark fields have been flavour eigenstates. To access the physical quark states the basis must be switched to mass eigenstates, which is achieved by diagonalising the mass matrices using four unitary matrices:

$$M_U^{\text{diag}} = V_{U,L} M_U V_{U,R}^\dagger,\ M_D^{\text{diag}} = V_{D,L} M_U V_{D,R}^\dagger. \tag{1.23}$$

The four unitary matrices, $V_{U/D,R/L}$, may then be used to transform the left-handed and right-handed quark fields into mass eigenstates:

$$U_L^{\text{mass}} = V_{U,L}U_L,\ U_R^{\text{mass}} = V_{U,R}U_R, \tag{1.24}$$

$$D_L^{\text{mass}} = V_{D,L}D_L,\ D_R^{\text{mass}} = V_{D,R}D_R. \tag{1.25}$$

The quark fields with superscript labels mass are the mass eigenstates obtained by transforming the flavour eigenstates with unitary matrices. The quark mass eigenstates in Eq. 1.24 and Eq. 1.25 can now be used to substitute for the quark fields in terms of flavour eigenstates in Eq. 1.18.

$$L_W = \frac{g}{2\sqrt{2}} \sum_{ij} \bar{U}_{L,i}^{\text{mass}} V_{U,L,ij} \gamma^\mu V_{D,L,ij}^\dagger D_{L,j}^{\text{mass}} W_\mu^+ + h.c., \tag{1.26}$$

which becomes

$$L_W = \frac{g}{2\sqrt{2}} \sum_{ij} V_{ij} \bar{U}_{L,i}^{\text{mass}} \gamma^\mu D_{L,j}^{\text{mass}} W_\mu^+ + h.c., \tag{1.27}$$

where

$$V = V_{U,L}V_{D,L}^\dagger = V_{CKM}, \tag{1.28}$$

is known as the CKM matrix. The CKM matrix is a unitary 3×3 matrix, reflecting the three generations of quarks. The CKM matrix can be written in terms of nine elements and the common notation is

$$V_{CKM} = \begin{pmatrix} V_{ud} & V_{us} & V_{ub} \\ V_{cd} & V_{cs} & V_{cb} \\ V_{td} & V_{ts} & V_{tb} \end{pmatrix}. \tag{1.29}$$

The elements in Eq. 1.29 represent the couplings between quarks in charged current weak interactions. For example, V_{cb} describes the coupling of a c quark to a b quark. The values of the CKM matrix elements are not predicted by the SM, although it is shown later that there are only four independent parameters. Therefore, it is important that they are measured accurately by experiment. A summary of the processes used to measure the magnitudes of the CKM matrix elements are presented in Tab. 1.4. The current world average values [5] of the magnitudes of the CKM matrix elements are

Element	Method of extraction	Measured Value
V_{ud}	Nuclear beta decay	0.97425 ± 0.00022
V_{us}	Leptonic and semileptonic kaon decays	0.2255 ± 0.0024
V_{ub}	Semileptonic B^0 and B^+ decays	0.00389 ± 0.00044
V_{cd}	Semileptonic charm decays	0.230 ± 0.011
V_{cs}	(Semi)leptonic decays of $(D^0)D_s^+$	1.023 ± 0.036
V_{cb}	Semileptonic B^0 and B^+ decays	0.0406 ± 0.0013
V_{td}	B^0-$\bar{B}^0$ oscillation frequency	$0.211 \pm 0.001 \pm 0.005$*
V_{ts}	B_s^0-$\bar{B}_s^0$ oscillation frequency	$0.211 \pm 0.001 \pm 0.005$*
V_{tb}	Single top production	0.88 ± 0.07

Table 1.4: Examples of the types of decays used to measure the elements of the CKM matrix. Measured values from [5]. *Presented measurement is V_{td}/V_{ts}.

$$|V_{CKM}| = \begin{pmatrix} 0.97428 \pm 0.00015 & 0.2253 \pm 0.0007 & 0.00347^{+0.00016}_{-0.00012} \\ 0.2252 \pm 0.0007 & 0.97345^{+0.00015}_{-0.00016} & 0.0410^{+0.0011}_{-0.0007} \\ 0.00862^{+0.00026}_{-0.00020} & 0.0403^{+0.0011}_{-0.0007} & 0.999152^{+0.000030}_{-0.000045} \end{pmatrix}. \quad (1.30)$$

These are the results of a global fit to the Standard Model using measurements and constraints such as unitarity. Alternatively, the CKM matrix may be written in terms of three mixing angles and a CP violating phase. This is done by considering that each V_{ij} can be a complex parameter, allowing for a total of eighteen free parameters. Unitarity removes nine of these, five of the remaining six complex phases may be rotated away by redefinition of the quark fields, leaving only the three mixing angles and one phase. It is worth noting again that what follows requires that the CKM matrix is unitary. Only with at least three quark generations are there enough free parameters to include CP violation in the theory of flavour changing weak decays. The standard choice of parametrisation from Chau and Keung [21] is

$$V = \begin{pmatrix} c_{12}c_{13} & s_{12}c_{13} & s_{13}e^{-i\delta} \\ -s_{12}c_{23} - c_{12}s_{23}s_{13}e^{+i\delta} & c_{12}c_{23} - s_{12}s_{23}s_{13}e^{+i\delta} & s_{23}c_{13} \\ s_{12}s_{23} - c_{12}c_{23}s_{13}e^{+i\delta} & -c_{12}s_{23} - s_{12}c_{23}s_{13}e^{+i\delta} & c_{23}c_{13} \end{pmatrix}, \quad (1.31)$$

where $c_{ij} = \cos\theta_{ij}$, $s_{ij} = \sin\theta_{ij}$ and the term δ is a complex phase that encompasses all CP violating contributions in the SM from quark flavour changing processes.

The relative sizes of the s_{ij} terms in Eq. 1.31 are known experimentally to fulfil the relation $s_{13} \ll s_{23} \ll s_{12} \ll 1$ [5]. This experimental hierarchy can be

Parameter	Best fit value
λ	0.2253 ± 0.0007
A	$0.808^{+0.022}_{-0.015}$
$\bar{\rho}$	$0.132^{+0.022}_{-0.014}$
$\bar{\eta}$	0.341 ± 0.013

Table 1.5: The global fit values of the Wolfenstein parameters [5].

exploited by using the Wolfenstein [22] parametrisation such that the CKM matrix becomes, to order λ^3,

$$V = \begin{pmatrix} 1 - \frac{\lambda^2}{2} & \lambda & A\lambda^3 (\rho - i\eta) \\ -\lambda & 1 - \frac{\lambda^2}{2} & A\lambda^2 \\ A\lambda^3 (1 - \rho - i\eta) & -A\lambda^2 & 1 \end{pmatrix}. \tag{1.32}$$

The following definitions were used to write Eq. 1.32:

$$s_{12} = \lambda = \frac{|V_{us}|}{\sqrt{|V_{ud}|^2 + |V_{us}|^2}}, \quad s_{23} = A\lambda^2 = \lambda \left| \frac{V_{cb}}{V_{us}} \right|,$$

$$s_{13} e^{i\delta} = V_{ub}^* = A\lambda^3 (\rho + i\eta) = \frac{A\lambda^3 (\bar{\rho} + i\bar{\eta}) \sqrt{1 - A^2\lambda^4}}{\sqrt{1 - \lambda^2} [1 - A^2\lambda^4 (\bar{\rho} + i\bar{\eta})]}. \tag{1.33}$$

The Wolfenstein parametrisation introduces four new parameters, A, λ, ρ and η. $\lambda \approx V_{us}$, A is a scaling factor between order λ and higher order terms and ρ and η are introduced at order λ^3 to parametrise the complex phase. The related parameters $\bar{\rho}$ and $\bar{\eta}$ are defined in Eq. 1.37. It should be noted that in terms of these four parameters the CKM matrix is unitary to any order of λ. The values of the CKM matrix elements in terms of the Wolfenstein parameterisation are extracted in a global fit and are shown in Tab. 1.5.

1.4 Unitarity triangle

Two relations can be found by imposing unitarity on the CKM matrix elements:

$$\Sigma_i V_{ij} V_{ik}^* = \delta_{jk}, \; \Sigma_j V_{ij} V_{kj}^* = \delta_{ik}, \tag{1.34}$$

which are formed by summing rows and columns of the CKM matrix elements and imposing unitarity. Six unitarity triangles (UTs) can be defined from these

expressions for the cases where $\delta_{jk} = 0$ and $\delta_{ik} = 0$. The areas of all of the triangles are the same, with a value equal to half that of the Jarlskog invariant J [23]. J is a convention independent measure of the amount of CP violation and is defined by

$$\mathrm{Im}\left[V_{ij}V_{kl}V_{il}^{*}V_{kj}^{*}\right] = J\sum_{m,n}\epsilon_{ikm}\epsilon_{jln}, \tag{1.35}$$

where ϵ_{abc} is a Levi-Civita symbol. The most commonly used of the unitarity triangles is the one given by

$$V_{ud}V_{ub}^{*} + V_{cd}V_{cb}^{*} + V_{td}V_{tb}^{*} = 0, \tag{1.36}$$

and it is shown in Fig. 1.3. By dividing by the best known length from measurements of CKM matrix elements, $V_{cd}V_{cb}^{*}$, the vertices of the triangle become (0,0), (0,1) and $(\bar{\rho},\bar{\eta})$. Parameters $\bar{\rho}$ and $\bar{\eta}$ are

$$\bar{\rho} \approx \rho\left(1 - \frac{\lambda^2}{2}\right),\ \bar{\eta} \approx \eta\left(1 - \frac{\lambda^2}{2}\right). \tag{1.37}$$

Given that the area of the triangle is related to CP violation in the SM, the lengths and angles of the UT must be accurately determined. The least accurately determined parameter of the triangle is the angle γ, at the (0,0) vertex. A summary of the current experimental status of the three angles α, β and γ can be seen in Tab. 1.6. The second set of angles shown on the figure, ϕ_i, are a set of alternative names used by the Belle experiment.

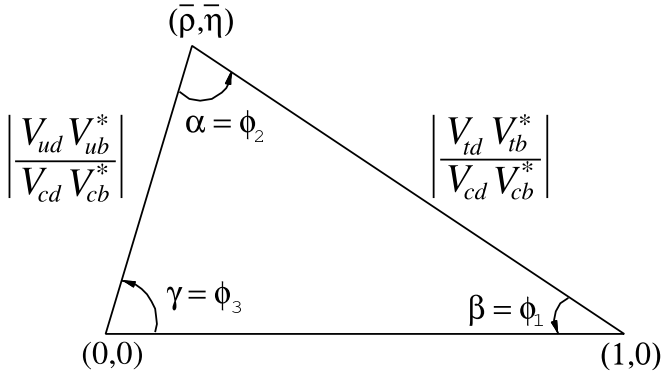

Figure 1.3: A sketch of the unitarity triangle, reproduced from Ref. [5].

Angle	Measurement (°)
α	$89.0^{+4.4}_{-4.2}$
β	68.6 ± 0.8
γ	73^{+22}_{-25}

Table 1.6: Current experimental status of the unitarity triangle angles from Ref [5].

The angles can be expressed in terms of the CKM elements:

$$\alpha = \arg\left(-\frac{V_{td}V_{tb}^*}{V_{ud}V_{ub}^*}\right),\ \beta = \arg\left(-\frac{V_{cd}V_{cb}^*}{V_{td}V_{tb}^*}\right),\ \gamma = \arg\left(-\frac{V_{ud}V_{ub}^*}{V_{cd}V_{cb}^*}\right). \tag{1.38}$$

From these equations it is clear that each angle must be measured using decay modes featuring the CKM matrix elements that appear in the definition. For example, Eq. 1.38 shows that γ only depends on CKM matrix elements from certain B hadron decays. In fact γ can be measured from tree level processes because it has no dependence on elements involving the top quark, which only appear in loop level processes. This makes γ unique amongst CP violation observables. More details on decay modes used to measure γ are given in section 1.6.

Figure 1.4 shows the constraints on the $\bar{\rho}$-$\bar{\eta}$ plane coming from knowledge of the various parameters that are labelled [24]. It is clear from the figure that the least accurate constraint on the plane comes from the angle γ.

1.5 Analysis techniques

Several analysis techniques and methods are discussed in this thesis so an overview of them is presented here. Dalitz plots are introduced in Sec. 1.5.1, the principles of neural networks are explored in Sec. 1.5.2 and the `sPlot` method is introduced in Sec. 1.5.3.

1.5.1 Dalitz plots

The Dalitz plot analysis technique [25] is used to calculate the amplitudes of resonant two-body decays of, for example, B and D mesons contributing to a three-body final state. The Dalitz plot is named after R. H. Dalitz who pioneered the use of these methods. For example, the decay $D^+ \to K^-K^+\pi^+$ can proceed via resonant two-body decays such as $D^+ \to \phi(1020)\pi^+$ and $D^+ \to K^+\overline{K}^*(892)^0$. The Dalitz plot of $D^+ \to K^-K^+\pi^+$, from LHCb [26], is shown in Fig 1.5.

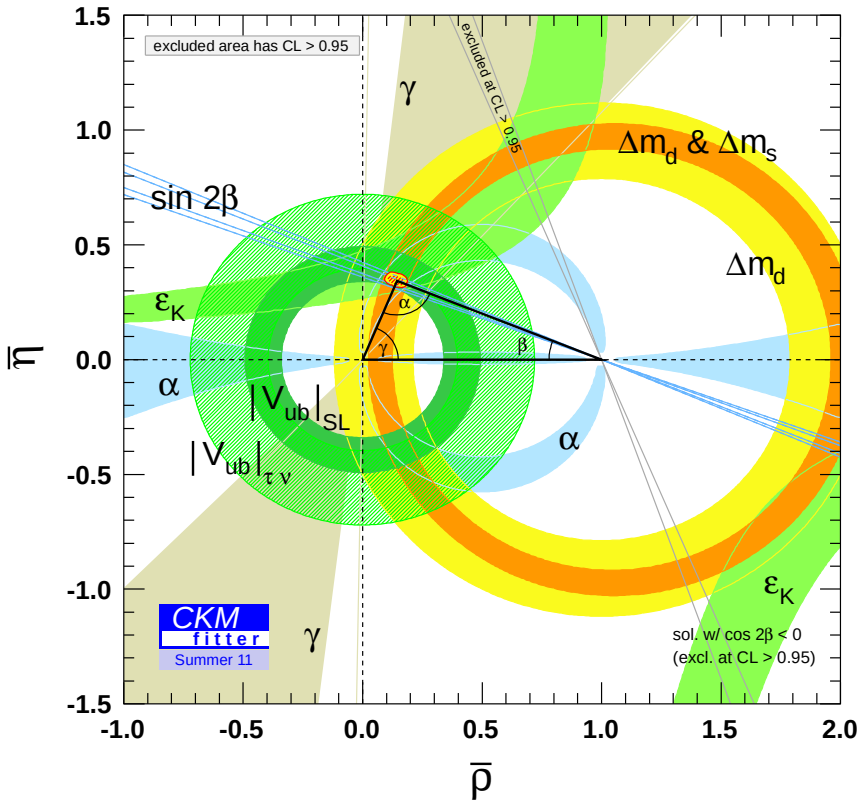

Figure 1.4: A plot of the $\bar{\rho}$-$\bar{\eta}$ plane, showing the experimental constraints on the SM. Each band represents the best fit to the parameter as labelled. The unitarity triangle is also shown. Taken from the `CKMfitter` group [24].

Consider now a decay of a spin zero particle to three pseudoscalar particles, $B \to abc$. The decay rate is

$$d\Gamma = \frac{1}{32\,(2\pi)^3\, m_B^3} |\mathcal{M}|^2 dm_{ab}^2 dm_{bc}^2, \tag{1.39}$$

where m_{ab} is the invariant mass of daughters a and b and m_B is the mass of the B meson. $\mathcal{M}$ is the scattering matrix element that contains all of the dynamics of the decay. The Dalitz plot is then defined as the two dimensional scatter plot of m_{ab}^2 and m_{bc}^2, although it should be noted that any combination of the invariant mass pairs could be used. If $|\mathcal{M}|^2$ is constant then the kinematically allowed region of the Dalitz plot is uniformally populated with events. Any structures that appear, such as bands at fixed invariant masses, are due to the resonant dynamics and not kinematics. The kinematically allowed region of the Dalitz plot is constrained by

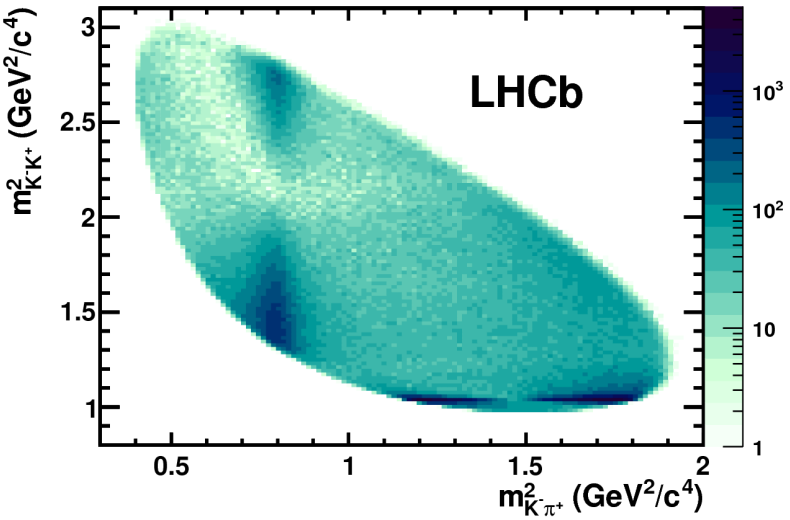

Figure 1.5: $D^+ \to K^-K^+\pi^+$ Dalitz plot where the vertical band is from the decay $D^+ \to K^+\bar{K}^*(892)^0$ with $\bar{K}^*(892)^0 \to K^-\pi^+$ and the horizontal band from $D^+ \to \phi(1020)\pi^+$ with $\phi(1020) \to K^+K^-$ events. Reproduced from Ref. [26].

the conservation of energy and momentum, and it may be shown that:

$$M_B^2 + M_a^2 + M_b^2 + M_c^2 = m_{ab}^2 + m_{ac}^2 + m_{bc}^2, \tag{1.40}$$

where M_x is the mass of particle x. Equation 1.40 shows that for a three-body final state there are three pairs of invariant masses that may be used as axes on a Dalitz plot. Three Dalitz plots may be defined from these, (m_{ab}^2, m_{ac}^2), (m_{ab}^2, m_{bc}^2) and (m_{ac}^2, m_{bc}^2). One of these definitions is then chosen based upon the physics being studied.

The boundary of the Dalitz plot seen in Fig 1.5 shows the kinematically allowed region. The diagonal Dalitz plot boundary, close to the LHCb label, is actually the third axis $m_{K^+\pi^-}^2$. Diagonal bands that appear on Dalitz plots correspond to a resonance on the third axis. The bands, that correspond to resonances, in Fig. 1.5 also appear to have structure. The type of band produced by a resonance is related to the angular momentum of the state. Scalar resonances produce a single band without further structures. Vector resonances produce a band with a two lobe structure, as seen in Fig. 1.5. Tensor resonances produce bands with three lobe structure. This derives from the conservation of angular momentum of the resonance to the daughter particles.

To determine phase information a fit must be performed over the Dalitz plot to extract the resonant structures seen in the plot. The most common way to form

the Dalitz plot amplitude is using the isobar model. The isobar model calculates the total amplitude as a sum of amplitudes from the two-body resonant decays as

$$\mathcal{A}\left(m_{ab}^2, m_{ac}^2\right) = \sum_{i=1}^{N} c_i F_i\left(m_{ab}^2, m_{ac}^2\right), \tag{1.41}$$

$$\bar{\mathcal{A}}\left(m_{ab}^2, m_{ac}^2\right) = \sum_{i=1}^{N} \bar{c_i} \bar{F_i}\left(m_{ab}^2, m_{ac}^2\right), \tag{1.42}$$

where F_i are amplitudes from each resonance containing the dynamics of the decay and c_i are complex coefficients describing the relative phase and magnitude of each resonant decay mode. There are two main methods used to model these resonances, in order to fit them and extract information from the Dalitz plot. The simplest method is to parametrise them with Breit-Wigner functions, which are suitable for isolated resonances. A more general method is to use the K-matrix formalism [27, 28], which is better suited for broad resonances that may overlap. This method utilises the Flatte distribution to preserve unitarity, which is violated when Breit-Wigner functions overlap. The choice of model introduces uncertainties so it must be carefully considered to minimise the effect on the measurement being made.

1.5.2 Neural networks

Neural networks were inspired by a simple model of how the human brain functions. They use a series of nodes that are connected together to mimic the vast network neurons in the human brain. In the context of particle physics, the principle of using neural networks is as follows. The network can be trained, using a set of input quantities, to learn the difference between different categories of events in a single dataset. For example, simulated samples can show the neural network how signal and background events look in terms of the given input variables. Once the neural network has determined the difference, it can then apply this knowledge to a different dataset.

1.5.3 `sPlot`

The `sPlot` technique is a method to unfold various categories of events in a data sample. Consider a data sample containing two sources of events, signal and background, that are peaking and flat across a quantity x respectively. By performing a fit to the distribution of x, with a Probability Density Function (PDF) for both signal and background shapes, the `sPlot` technique allows the categories to be separated on an event-by-event basis. This is achieved using the PDFs, fitted yields

and the correlation matrix from the fit to calculate a weight for each event. These weights, or `sWeights`, are normalised so that the sum of the `sWeights` is equal to the fitted yield. In fact, `sWeights` can be assigned for any PDF included in the fit, for example both signal and background. Note that the sum of `sWeights` for a given event is equal to one.

Using this technique it is possible to create distributions that contain only the signal events. For example, in this thesis the `sPlot` technique is used to create background subtracted Dalitz plot distributions in Sec. 6.1.

1.6 Measuring the angle γ at LHCb

To determine the value of γ both tree level and loop level processes may be studied. Tree level measurements are expected to be of the Standard Model value of γ while loop processes can also probe new physics, due to the possible presence of new particles in the loops. This means that the value of γ as measured by loop decays will be altered by the effects of new physics, if they are present. The focus of this thesis is to use tree level processes, in order to constrain the Standard Model value of γ. Without accurate knowledge of this parameter, the presence of new physics in loop processes cannot be separated from the Standard Model effects. In order to find new physics the Standard Model must first be constrained and understood. In fact, by improving the measurement of γ the area of the unitarity triangle can be measured to extract the total amount of CP violation described by the Standard Model using a process insensitive to new physics.

Equation 1.38 shows that the angle γ depends on the relative phases between the CKM matrix elements V_{ud}, V_{ub}, V_{cd} and V_{cb}. To make a measurement of γ from tree level decays, B hadrons decaying to final states through both $b \to u$ and $b \to c$ transitions can be studied. At LHCb there are two categories of measurements used to measure γ, time-independent and time-dependent methods, described in Sec. 1.6.1 and Sec. 1.6.2 respectively.

1.6.1 Time-independent methods

Time-independent extractions of γ are based on measurements of direct CP violation (Sec. 1.2.1). Consider the decay mode $\bar{B}^0 \to D\bar{K}^{*0}$, as shown in Fig. 1.6, where D represents both D^0 and $\bar{D}^0$ decaying to the same final states. The figure shows that $\bar{B}^0$ may decay into two final states, $D^0\bar{K}^{*0}$ and $\bar{D}^0\bar{K}^{*0}$, that interfere with each other when the D mesons decay into a common final state. The difference in

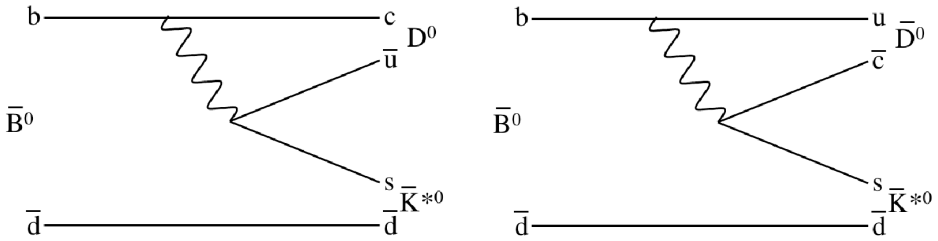

Figure 1.6: Feynman diagrams for the tree level processes $\bar{B^0} \to D^0 \bar{K}^{*0}$ (left) and $\bar{B^0} \to \bar{D^0} \bar{K}^{*0}$ (right). Reproduced from Ref. [29].

the weak-phase between the diagrams is $-\gamma$, coming from the weak-phase difference between the CKM matrix elements involved in the $b \to u$ and $b \to c$ transitions.

The amplitudes for the two processes are

$$A\left(\bar{B^0} \to D^0 \bar{K}^{*0}\right) = A_B, \tag{1.43}$$

$$A\left(\bar{B^0} \to \bar{D^0} \bar{K}^{*0}\right) = A_B r_B e^{i(\delta_B - \gamma)}, \tag{1.44}$$

where r_B is the ratio of the magnitudes of the two amplitudes and δ_B is the strong-phase difference between the two amplitudes. The parameter r_B depends on the CKM matrix elements involved in each decay mode and hadronic factors. Only one phase difference, δ_B, can be measured so the standard convention is to set the strong-phase of the favoured amplitude to zero. In this example, Eq. 1.43 is the favoured mode and Eq. 1.44 the suppressed mode, resulting from the r_B factor. The dependence on γ is clear as it appears in the expression for the suppressed mode, Eq. 1.44. It is important to note that the sign of γ flips when the B^0 versions of Eqs. 1.43 and 1.44 are considered.

A second pair of decay modes, $B^- \to D^0 K^-$ and $B^- \to \bar{D^0} K^+$, can also be used to extract γ in the same way. The Feynman diagrams for these decays are very similar to those shown in Fig. 1.6 with the spectator quark changed from $\bar{d}$ to $\bar{u}$. For both the neutral and charged B case, the measurement of γ itself depends on the decay modes of the D mesons. Three different methods are discussed below; GLW (Gronau, London and Wyler) [30, 31], ADS (Atwood, Dunietz and Soni) [32] and the Dalitz plot analysis technique [33, 34]. For some background on Dalitz plots please see Sec. 1.5.1.

GLW method

The GLW method refers to using the decay of D mesons to CP eigenstates, such as the CP even $\pi^+\pi^-$ and K^+K^- states. Firstly consider the D meson in terms of

CP eigenstates:

$$D^0 \to \frac{1}{\sqrt{2}}\left(D_1 + D_2\right) \tag{1.45}$$

and

$$\bar{D^0} \to \frac{1}{\sqrt{2}}\left(D_1 - D_2\right), \tag{1.46}$$

where D_1 is the CP even eigenstate and D_2 is the CP odd eigenstate. The decay width for D mesons going to a CP eigenstate such as the CP even mode K^+K^- in the decay chain $B^\pm \to DK^\pm$ can be written as:

$$\Gamma\left(B^\pm \to D_1 K^\pm\right) = |A_B|^2|A_1|^2|1 + r_B e^{\pm i\gamma} e^{i\delta_B}|^2 \tag{1.47}$$

and for the CP odd states such as $K_S\pi^0$ as:

$$\Gamma\left(B^\pm \to D_2 K^\pm\right) = |A_B|^2|A_2|^2|1 - r_B e^{\pm i\gamma} e^{i\delta_B}|^2, \tag{1.48}$$

where A_B, r_B and δ_B have the same meanings as in Eq. 1.43 and Eq. 1.44 but for the $B^\pm \to DK^\pm$ decay mode instead. Consider now both the CP even decay (+) and CP odd decay (-), Eqs. 1.47 and 1.48, and define a CP asymmetry between the partial widths of the B^+ and B^- decay modes

$$A_{CP\pm} = \frac{\Gamma(B^- \to D_{CP\pm}K^-) - \Gamma(B^+ \to D_{CP\pm}K^+)}{\Gamma(B^- \to D_{CP\pm}K^-) + \Gamma(B^+ \to D_{CP\pm}K^+)} = \frac{\pm 2 r_B \sin\delta_B \sin\gamma}{1 + r_B^2 \pm 2 r_B \cos\delta_B \cos\gamma} \tag{1.49}$$

and a charge averaged rate ratio:

$$R_{CP\pm} = \frac{\Gamma\left(B^- \to D_{CP\pm}K^-\right) + \Gamma\left(B^+ \to D_{CP\pm}K^+\right)}{\Gamma\left(B^- \to D^0K^-\right) + \Gamma\left(B^+ \to \bar{D}^0K^+\right)} = 1 + r_B^2 \pm 2 r_B \cos\delta_B \cos\gamma. \tag{1.50}$$

The angle γ can be extracted from these CP violating observables by measuring the rates and using knowledge of δ_B and r_B from other observables, such as those found in the ADS method, described below. A problem with the GLW method is that the asymmetry defined by Eq. 1.49 is small and therefore difficult to measure accurately. This is caused by the heavy suppression of the $b \to u$ decay compared to the $b \to c$ decay.

The GLW method has been used for $B^+ \to D^{(*)}K^{(*)+}$ modes at the B factories [35, 36] and in hadronic environments at CDF [37] and LHCb [38]. However, these analyses do not actually present measurements of γ at this stage, instead measuring the four parameters $A_{CP\pm}$ and $R_{CP\pm}$. This is to allow the measurements of the observables, $A_{CP\pm}$ and $R_{CP\pm}$, to be averaged and improved before calculating

γ. These are summarised in Fig. 1.7. From Eqs. 1.49 and 1.50 it is clear that this is the first step towards a measurement of γ.

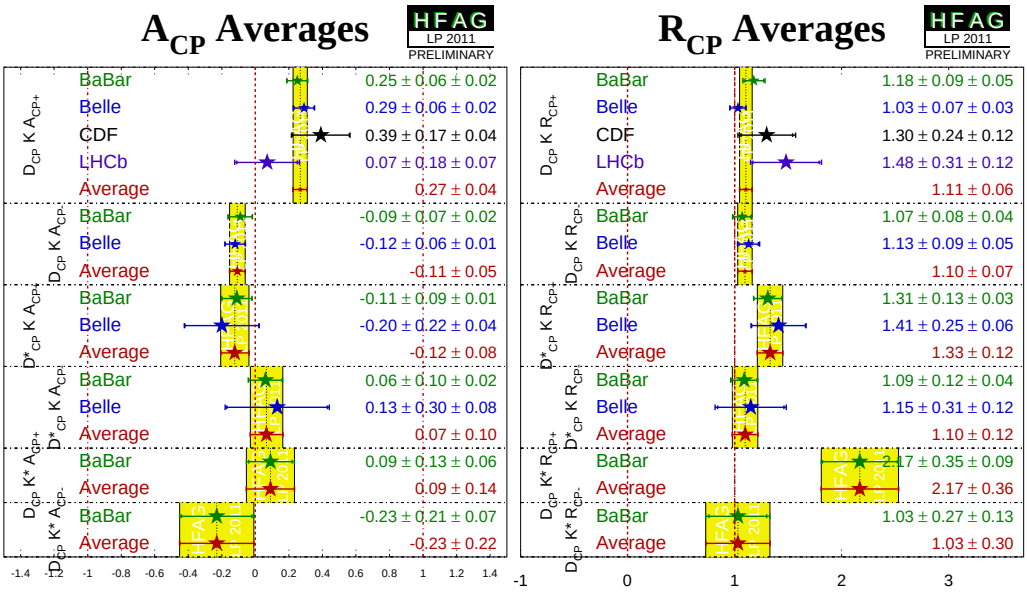

Figure 1.7: Comparison of current (left) A_{CP} and (right) R_{CP} measurements from the GLW method. Reproduced from Ref. [39].

ADS method

The ADS method describes the use of flavour specific D meson decays, such as $K^-\pi^+$, where four modes can be measured. Two Cabibbo favoured (CF) modes, $D^0 \to K^-\pi^+$ and $\bar{D}^0 \to K^+\pi^-$, and two doubly Cabibbo suppressed (DCS) modes, $D^0 \to K^+\pi^-$ and $\bar{D}^0 \to K^-\pi^+$. These modes can be used to balance the effect of r_B which suppresses one of the B meson decays by introducing a new ratio, r_D, which is the ratio between CF and DCS decays of the D mesons. This procedure allows the two partial amplitudes for a process to be of approximately the same magnitude, which enhances interference and may, therefore, increase the amount of CP violation.

Consider again the decay modes $B^\pm \to DK^\pm$, this time with $D \to K^+\pi^-$ and $D \to K^-\pi^+$ for B^- and B^+ respectively. The partial widths of the four decay modes can be written as

$$\Gamma\left(B^- \to D_{K\pi}K^-\right) = |A_B|^2|A_D|^2\left(r_D^2 + r_B^2 + 2r_B r_D\cos\left(\delta_B + \delta_D - \gamma\right)\right) \quad (1.51)$$

and

$$\Gamma\left(B^+ \to D_{K\pi}K^+\right) = |A_B|^2|A_D|^2\left(r_D^2 + r_B^2 - 2r_B r_D\cos\left(\delta_B + \delta_D + \gamma\right)\right), \quad (1.52)$$

where δ_D is the strong phase difference between the DCS and CF decay modes of the D meson. Combining Eq. 1.51 and Eq. 1.52 leaves seven parameters as unknowns, excluding the strong phases. To extract γ using the ADS method, more decay modes of the D mesons can be considered to increase the number of equations without doubling the number of unknowns each time. For example, $D \to K^+\pi^-\pi^+\pi^-$ and $D \to K^+\pi^-\pi^0$ can be used. The number of unknowns can also be reduced by using input from measurements of D decays. The parameters r_D and δ_D are both known experimentally for several D decay modes from the CLEO_c experiment [40]. In addition, $|A_B|$ and $|A_D|$ cancel by appearing in each of Eqs. 1.51 and 1.52 as a constant multiplier, reducing the effective number of unknowns to three.

Alternatively, some experimental observables may be defined using the rates defined above. Firstly, charge specific ratios may be defined to measure the rate of $B^\pm$ decays with the DCS D decay measured relative to the CF D decay mode:

$$R^\pm = \frac{\Gamma(B^\pm \to D_{K^\mp\pi^\pm}K^\pm)}{\Gamma(B^\pm \to D_{K^\pm\pi^\mp}K^\pm)} = r_D^2 + r_B^2 + 2r_B r_D\cos(\delta_B \pm \gamma), \quad (1.53)$$

and these can then be used to define the rate ratio

$$R_{ADS} = \frac{R^+ + R^-}{2} = r_D^2 + r_B^2 + 2r_B r_D\cos(\delta_D + \delta_B)\cos(\gamma) \quad (1.54)$$

and the CP asymmetry

$$A_{ADS} = \frac{R^- - R^+}{R^- + R^+} = \frac{2r_B r_D\sin(\delta_D + \delta_B)\sin(\gamma)}{r_D^2 + r_B^2 + 2r_B r_D\cos(\delta_D + \delta_B)\cos(\gamma)}. \quad (1.55)$$

Analyses of $B^+ \to D^{(*)}K^{(*)+}$ decay modes using the ADS method have been performed at the B factories [41, 42] and also in hadronic environments at, for example, CDF [43] and LHCb [44]. Similarly to the GLW method, these studies have not yielded a measurement of γ yet, but focus on observation of the DCS decay modes and the relative rates of the two. R_{ADS} and A_{ADS} have been measured in such analyses and a comparison of the measurements is shown in Fig. 1.8.

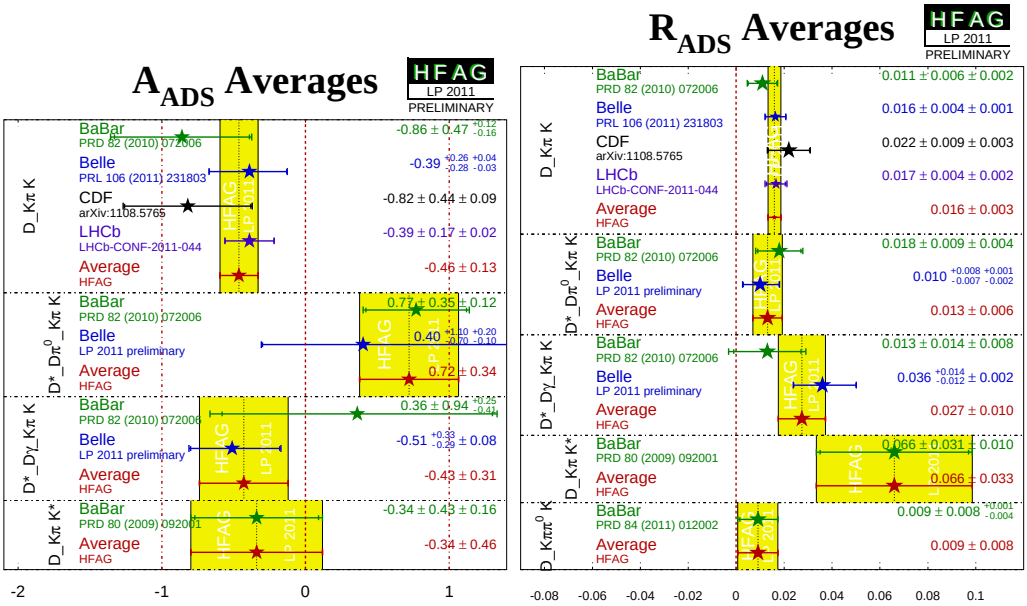

Figure 1.8: Comparison of current A_{ADS} (left) and R_{ADS} (right) measurements. Reproduced from Ref. [39].

Dalitz plot analysis

The angle γ can also be measured by performing a Dalitz plot analysis of three body self-conjugate D decays [45]. Clear resonant structure and a comparatively large branching fraction make $D \to K^0_S\pi^+\pi^-$ the most attractive option. The fit can then be performed as a likelihood fit or a binned fit with systematic uncertainties arising from model dependency and strong-phase parameters respectively. An introduction to Dalitz plot analysis was presented in Sec. 1.5.1.

Consider now the decay $B^\pm \to D\left(K^0_S\pi^+\pi^-\right)K^\pm$, for which the partial decay width is

$$\Gamma\left(B^- \to D_{K^0_S\pi^+\pi^-}K^-\right) = Y\left[A_D^{(+-)} + r_B^2 A_{\bar{D}}^{(-+)} + 2r_B Re\left(A_D^{(+-)}A_{\bar{D}}^{*(-+)}e^{i(\delta_B-\gamma)}\right)\right], \tag{1.56}$$

where

$$Y = \frac{dm_+^2\, dm_-^2}{32\,(2\pi)^3\, M^3}, \tag{1.57}$$

and

$$A_D^{(+-)} = A_D\left(m_+^2, m_-^2\right). \tag{1.58}$$

In Eqs. 1.56 and 1.58 the term $A_D\left(m_+^2, m_-^2\right)$ is the complex amplitude of the D^0 at a given point on the Dalitz plot. The terms m_+^2 and m_-^2 are the invariant mass squares for the particle combinations $K^0_S\pi^+$ and $K^0_S\pi^-$ respectively. All other symbols have

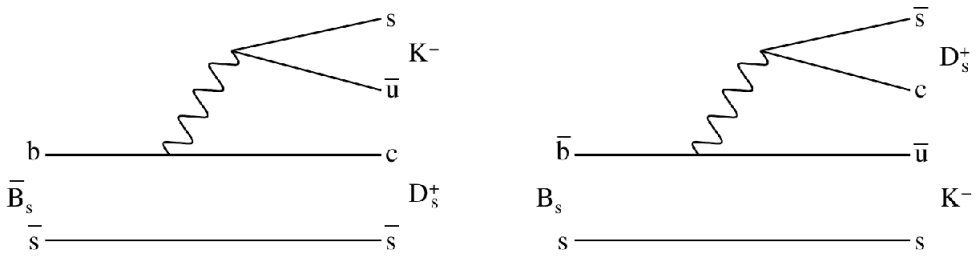

Figure 1.9: Feynman diagrams for $B_s^0 \to D_s^+ K^-$ (left) and $\bar{B}_s^0 \to D_s^+ K^-$ (right). Reproduced from [29].

the same meanings as previously discussed in this section. The dependence on γ is clear and it can be obtained using an unbinned maximum likelihood fit to one, or several, B decay channel(s).

The Dalitz plot analysis method has been employed by the B factories to make the most accurate determinations of γ. The results of the analyses are:

- BaBar: $\gamma = (68 \pm 14 \pm 4 \pm 3)^\circ$, using DK^+, D^*K^+ and DK^{*+} modes [33];
- Belle: $\gamma = (78^{+11}_{-12} \pm 4 \pm 9)^\circ$, using DK^+ and D^*K^+ modes [34].

The uncertainties are, from left to right, statistical, systematic and the model-dependence of the D decay used.

1.6.2 Time-dependent methods

Time-dependent measurements of γ at LHCb exploit $b \to u$ and $b \to c$ decays that interfere due to oscillations of the neutral $B_{d,s}$ mesons such that both the particle and antiparticle decay to the same final state, as discussed in section 1.2.2. Figure 1.9 shows an example of this where both B_s^0 and $\bar{B}_s^0$ decay to $D_s^+ K^-$. Sensitivity to γ comes from interference between decays that occur before and after mixing, hence introducing a time dependence. This particular decay mode is sensitive to $\gamma - \phi_s$ where ϕ_s is the phase from B_s^0-$\bar{B}_s^0$ mixing. However, ϕ_s will be measured using other decay modes such as $B_s^0 \to J/\psi\phi$, allowing γ to be determined.

B^0 mesons can also be used to measure γ in this way. For example B^0 and $\bar{B}^0$ can both decay to the following final states; $D^-\pi^+$ and $D^+\pi^-$. In this case it is actually $\gamma + 2\beta$ that is measured but Tab. 1.6 shows that β is well measured, allowing a value for γ to be obtained.

1.7 $B_{(d,s)} \to Dhh'$ modes

Decays of neutral B mesons of the form $B_{(d,s)} \to Dhh'$, where h and h' are a charged pion, charged kaon or proton, are interesting for many reasons.

Firstly, they can provide information on the dynamics of B meson decays. Secondly, they provide sensitivity to CP violation and angles of the unitarity triangle. In addition they can provide sensitivity to the B_s^0 mixing phase, ϕ_s. Below is a summary of the various $B_{(d,s)} \to Dhh'$ decay modes and the most interesting measurements that can be made:

- $B^0 \to D\pi^+\pi^-$ can be used to measure β using a time dependent method. This is discussed in, for example, Refs. [46, 47].
- $B^0 \to DK^+\pi^-$ provides sensitivity to measure γ using a time integrated method. See, for example, Refs. [48, 49].
- $B_s^0 \to DK^+K^-$ can yield measurements of ϕ_s and γ through time dependent and time integrated methods respectively. For details please see, for example, Ref. [50].
- The other modes such as $B_s^0 \to DK^+\pi^-$ and $B^0 \to \bar{D}^0K^+K^-$ are equally important because they will appear as backgrounds in the γ sensitive channels listed above.

The current status of the $B_{(d,s)} \to Dhh'$ branching fractions is shown in Tab. 1.7. It shows that the status is good for the B^0 meson, taking advantage of measurements from the B factories. However, there is much more work to do for the B_s^0. The missing branching fraction in the B^0 system is $\bar{D}^0K^+K^-$, which will be addressed as the focus of this thesis.

A first observation and measurement of the branching fraction of $B^0 \to \bar{D}^0K^+K^-$ is interesting because it is currently unknown. More importantly, an analysis of this type would be the first step on the road to measuring γ and β_s using the sister decay $B_s^0 \to \bar{D}^0K^+K^-$. Indeed, characterising the B^0 contribution to the DK^+K^- final state is of vital importance in making an accurate measurement of the B_s^0 mode. In fact, it could also be a useful starting point for any future analyses of $B_{(d,s)} \to Dhh'$ modes at LHCb. Evidence for the $B_s^0 \to \bar{D}^0K^+K^-$ decay mode would also be an excellent result to show that further dedicated studies of this decay mode are possible.

The Feynman diagrams of two possible intermediate decays that could contribute to the $B^0 \to \bar{D}^0K^+K^-$ final state are shown in Fig. 1.10. Since the decay is,

Mode	Branching fraction	Reference
	B^0	
$\bar{D}^0\pi^+\pi^-$	$(8.4 \pm 0.4 \pm 0.8) \times 10^{-4}$	[51]
$\bar{D}^0\rho^0$	$(3.19 \pm 0.20 \pm 0.45) \times 10^{-4}$	[51]
$D_2^*(2460)^-\pi^+$ (†)	$(2.15 \pm 0.17 \pm 0.31) \times 10^{-4}$	[51]
$\bar{D}^0K^+\pi^-$	$(8.8 \pm 1.5 \pm 0.9) \times 10^{-5}$	[52]
$\bar{D}^0K^{*0}$	$(4.2 \pm 0.6) \times 10^{-5}$	[5, 39]
$D_2^*(2460)^-K^+$ (†)	$(1.83 \pm 0.40 \pm 0.31) \times 10^{-5}$	[52]
$D^0K^+\pi^-$	$< 1.9 \times 10^{-5}$	[52]
D^0K^{*0}	$< 1.1 \times 10^{-5}$	[53]
$\bar{D}^0K^+K^-$	No measurement	
$\bar{D}^0\phi$	$< 1.2 \times 10^{-5}$	[54]
$\bar{D}^0p\bar{p}$	$(1.02 \pm 0.04 \pm 0.06) \times 10^{-4}$	[55]
	B_s^0	
$\bar{D}^0\pi^+\pi^-$	No measurement	
$\bar{D}^0\rho^0$	No measurement	
$\bar{D}^0K^-\pi^+$	No measurement	
$\bar{D}^0\bar{K}^{*0}$	$(4.72 \pm 1.07 \pm 0.48 \pm 0.37 \pm 0.74) \times 10^{-4}$	[56]
$D^0K^-\pi^+$	No measurement	
$D^0\bar{K}^{*0}$	No measurement	
$\bar{D}^0K^+K^-$	No measurement	
$\bar{D}^0\phi$	No measurement	
$\bar{D}^0p\bar{p}$	No measurement	

Table 1.7: Current experimental status of branching fraction measurements of $B \to Dhh^{(\prime)}$ decays. Quantities denoted by (†) are product branching fractions to the given three-body final state.

as yet, unmeasured these are only possible diagrams, which have not been proved correct or otherwise. On the left is an example W-exchange diagram where the $D_{s2}^{*-}(2573)$ decays to $\bar{D}^0K^-$. On the right is a colour suppressed tree process proceeding via an $a_0^0(980)$ meson which decays to K^+K^-. Colour suppression means that the quarks produced from the W boson decay are forced to have a certain colour change, to allow the final state mesons to be colourless. This causes a suppression of the rate because the W can produce quark pairs with (red anti-red), (blue anti-blue) and (green anti-green) colour charge, but only one of these is valid. The $a_0^0(980)$ has quantum numbers $J^{PC} = 0^{++}$, and a pole mass close to the threshold for KK production. The lineshape is therefore complicated, with a narrow width below the

KK threshold that becomes wider above threshold.

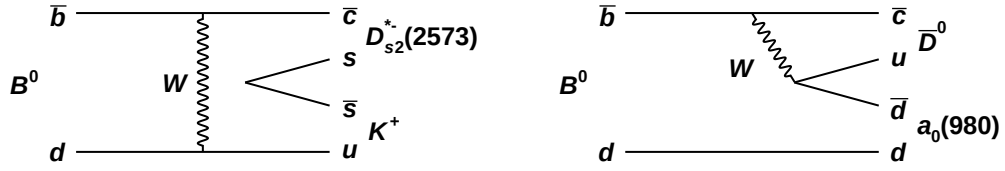

Figure 1.10: Feynman diagrams for $B^0 \to \bar{D}^0 K^+ K^-$ via W-exchange (left), and rescattering from colour-suppressed decay (right).

The diagram on the left of Fig. 1.10 shows an example of $s\bar{s}$ production in B^0 meson decays. This mechanism has been observed by Belle [57] in, for example, the decay $B^+ \to \bar{D}^0 K^+ \bar{K}^0$, with a large branching fraction:

$$\mathcal{B}(B^+ \to \bar{D}^0 K^+ \bar{K}^0) = (5.5 \pm 1.4 \pm 0.8) \times 10^{-4} \,. \tag{1.59}$$

This suggests that other decays of B^0 and B^+ mesons could also occur through $s\bar{s}$ production with large branching fractions.

1.8 Summary

This chapter has given an overview of the Standard Model and a more in depth description of the areas of particle physics most relevant to the work that follows in later chapters. The history of CP violation has been covered, leading on to the current state of CP violation studies with the CKM matrix and the unitarity triangle. Some methods of extracting the unitarity triangle angle γ have been discussed, with a focus on time-independent, tree level decays. Finally the current status of $B_{(d,s)} \to Dhh'$ decay modes was considered and the first observation and measurement of the $B^0 \to \bar{D}^0 K^+ K^-$ branching fraction introduced as the analysis documented in this thesis.

Chapter 2

The LHCb detector and the LHC accelerator

The Large Hadron Collider beauty (LHCb) experiment [58] is one of four main experiments based at the Large Hadron Collider (LHC) [59] at the European Organization for Nuclear Research (CERN) [60]. It is positioned at Intersection Point 8 of the LHC, where DELPHI [61] was housed on the Large Electron-Positron (LEP) collider. The LHC and LHCb detector are described in greater detail in sections 2.1 and 2.2 respectively.

2.1 The Large Hadron Collider

The LHC is a superconducting proton-proton collider located at the CERN laboratory on the French-Swiss border, just outside Geneva. The LHC is located in the old LEP tunnel, between 45 m and 170 m underground and is a 26.7 km ring. It is the highest energy particle accelerator in the world with a maximum design centre of mass energy of 14 TeV at a peak luminosity of 10^{34} cm^{-2}s^{-1}. Luminosity is defined as

$$L = fn\frac{N_1 N_2}{A} \tag{2.1}$$

where f is the revolution frequency, n is the number of proton bunches in each beam, N_i is the number of protons in each bunch for beam i and A is the cross sectional area of the beams. However, the data taken during 2010 and 2011 was at half of this energy, a centre of mass energy of 7 TeV. The peak luminosity delivered by the LHC during this period is shown in Fig. 2.1, with values at the end of the year approaching 4×10^{33} cm^{-2}s^{-1} for the general purpose detectors.

The four main experiments based at the LHC are; two general purpose detectors, A Toroidal LHC ApparatuS (ATLAS) [62] and the Compact Muon Solenoid (CMS) [63]; A Lead Ion Collider Experiment (ALICE) [64] and finally LHCb, the focus of this thesis.

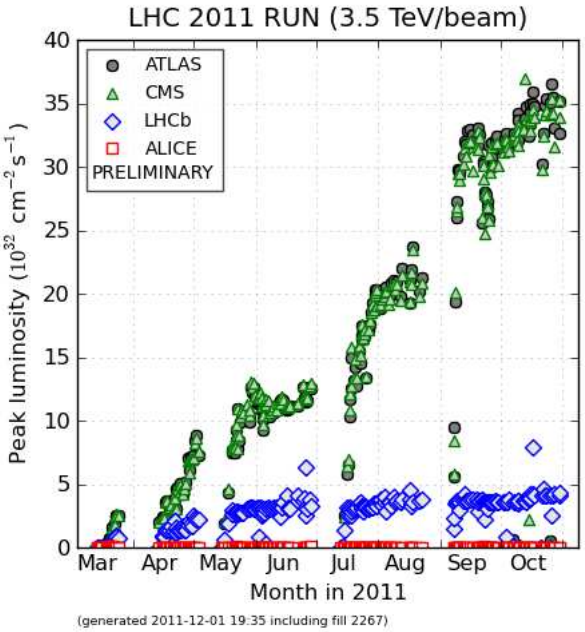

Figure 2.1: Peak luminosity achieved by the LHC during 2011 running. Figure reproduced from Ref. [65].

The LHC is the last stage in a series of smaller accelerators. It is fed by the CERN injector chain: LINear ACcelerator 2 (LINAC2) [66] → Proton Synchrotron Booster (PSB) [67] → Proton Synchrotron (PS) [68] → Super Proton Synchrotron (SPS) [69]. The injection chain is shown schematically in Fig. 2.2. The energy reached by each stage of the chain is 50 MeV, 1.4 GeV, 25 GeV and 450 GeV by the LINAC2, PSB, PS and SPS respectively. The protons are then injected into two counter rotating beams in the LHC and accelerated up to a maximum energy of 7 TeV per beam. Protons are injected into the LHC in bunches, with many bunches forming the two beams. Once the beam has been injected, the bunches of protons are collided at the experimental halls until the number of remaining protons falls low enough that the beams are dumped and injection begins again. The period between beam injection and a beam dump is known as a fill.

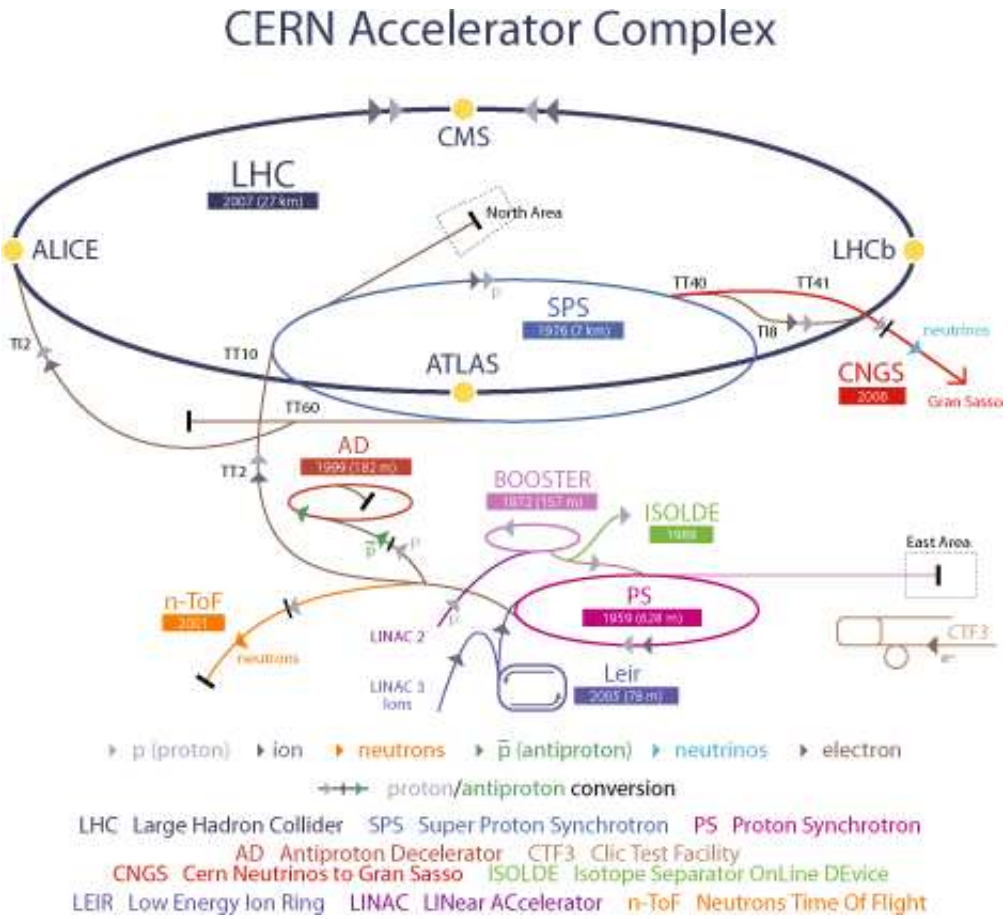

Figure 2.2: The CERN particle accelerator complex. The LHC injection chain can be seen, with the LINAC2 in purple, the PSB (labelled BOOSTER) in lilac, the PS in pink and the SPS in blue. The yellow dots mark the locations of the four major experiments currently running at the LHC. Figure taken from [70].

2.2 LHCb detector

The LHCb detector is a single arm spectrometer that has a forward angular coverage from 10 mrad to 250 (300) mrad in the vertical (horizontal) plane. The layout of the LHCb detector is shown in Fig. 2.3, with the z coordinate increasing from left to right along the beam line and the y coordinate vertically.

The LHCb detector was designed to run at a luminosity of 2×10^{32} cm^{-2}s^{-1}, a factor fifty lower than the maximum design luminosity of the LHC machine. This means that events with single p-p interactions per bunch crossing dominate, allowing for simpler analysis compared to events with multiple interactions. This is achieved by changing the beam displacement at the interaction point. This process, known as

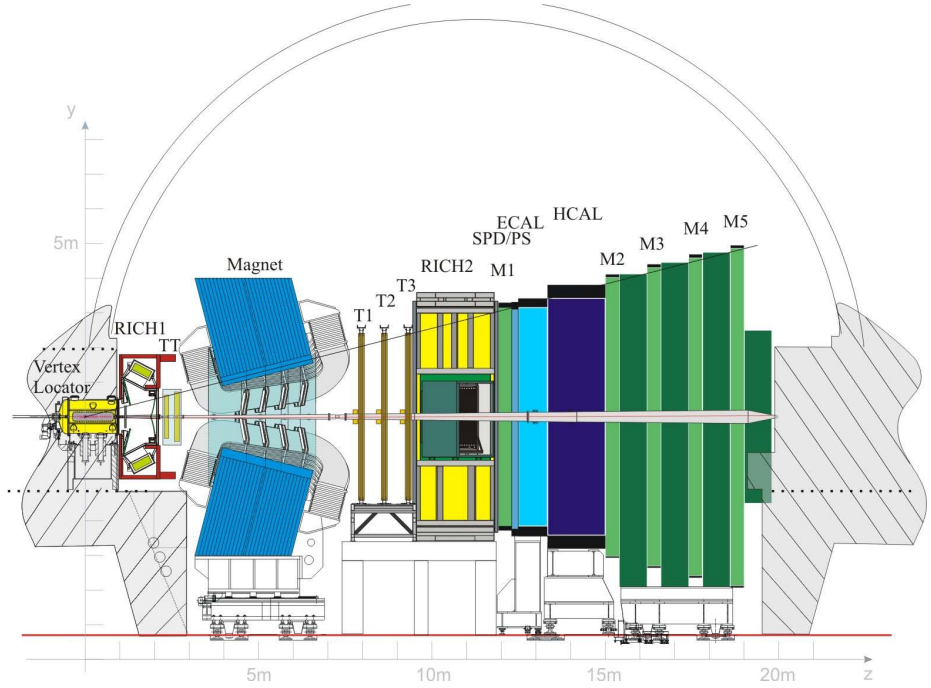

Figure 2.3: The layout of the LHCb detector with all of the sub detectors labelled. Figure from Ref. [58].

luminosity levelling, allows LHCb to receive a constant luminosity throughout a fill. An example of this is shown in Fig 2.4, where the luminosity at LHCb is flat and that of ATLAS and CMS falls exponentially. Other reasons behind this choice are to reduce occupancies and radiation damage suffered by the detectors, particularly the silicon vertex locator. It may also be noted that LHCb has run above the design luminosity for most of the 2011 data taking at a value around 3×10^{32} cm^{-2}s^{-1}, as shown by Fig 2.4.

The design of the detector was led by the requirement to study B physics. Excellent vertex resolution combined with excellent momentum resolution allows for good proper time resolution, vital for the study of neutral B_s meson oscillations. Particle identification of protons, pions and kaons is particularly crucial to study some of the key physics processes, such as $B \to DK^{(*)}$ decays. Finally the triggers, data acquisition and readout systems must be able to cope with the high data rate.

The LHCb detector consists of several subsystems that are, starting from the interaction point; the VErtex LOcator (VELO); two Ring Imaging CHerenkov detectors, RICH1 and RICH2; the tracking system, consisting of a Tracker Turicensis (TT), Inner Tracker (IT) and the Outer Tracker (OT); the magnet; the calorimeter

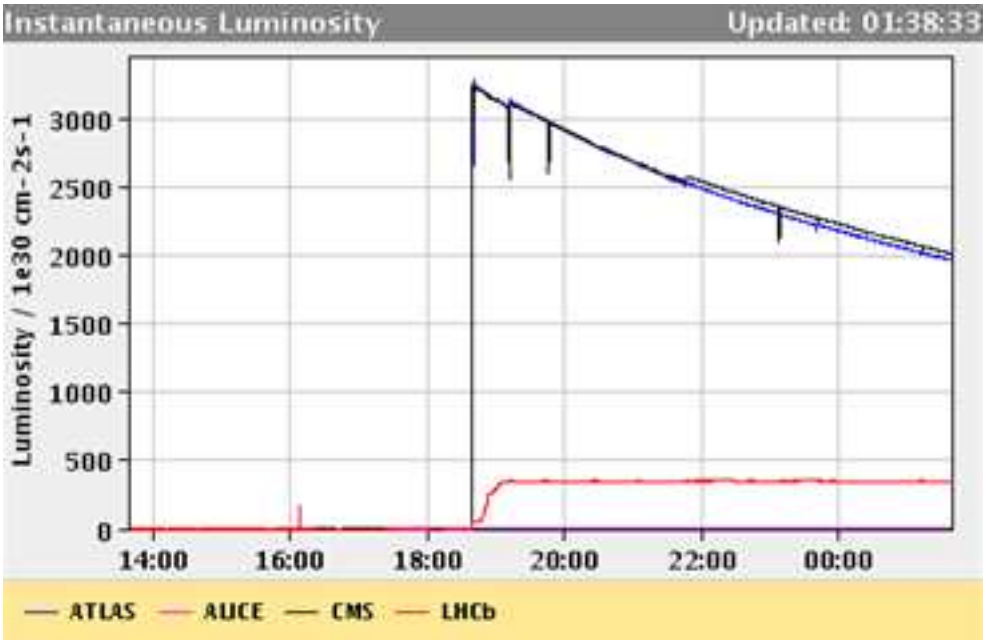

Figure 2.4: The constant instantaneous luminosity at LHCb (red) during a fill to illustrate luminosity levelling. For comparison the luminosity at ATLAS (blue) and CMS (black) are shown. Note that the horizonatal axis shows time in hours. Adapted from a figure in Ref. [71].

system, consisting of a Scintillator Pad Detector (SPD), PreShower detector (PS), Electromagnetic CALorimeter (ECAL) and Hadron CALorimeter (HCAL); and the muon system, consisting of stations M1 to M5. These elements are described in the following sections in more detail. Other elements of the LHCb experiment such as the Trigger system, Online system and a review of the offline software are discussed in Secs. 2.2.7, 2.2.8, 2.2.9 respectively.

2.2.1 Vertex detector

The VELO is designed to provide precise measurements of tracks close to the interaction point. This allows for excellent primary and secondary vertex resolutions that are required for the study of B hadron decays. The VELO consists of forty two modules, each with two silicon micro-strip sensors, one for R measurements and one for ϕ. The R sensors measure the radial distance away from the beam line and the ϕ sensors measure the azimuthal coordinate around the beam. The layout of these modules is shown by the top part of Fig. 2.5.

The VELO must cover the same range of angular acceptance as the down-

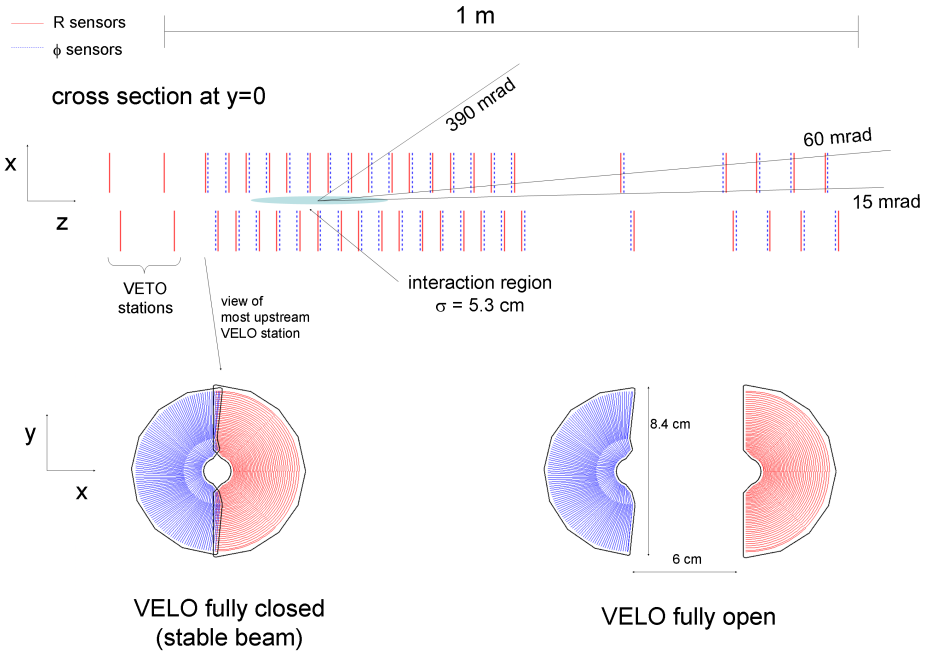

Figure 2.5: (Top) The layout of the forty two VELO modules and four pile-up, or VETO, modules. (Bottom) A view of two VELO sensors, on opposite sides of the beam, in the open (right) and closed (left) position. The overlap between the sensors is clearly visible, with the R sensor on the right and ϕ sensor on the left of each diagram. Reproduced from Ref. [58].

stream detectors, corresponding to a pseudorapidity range of $2 < \eta < 5$. Pseudorapidity is defined, for a generic particle, as

$$\eta = \frac{1}{2}\ln\left(\frac{|p| + p_z}{|p| - p_z}\right), \tag{2.2}$$

where p is the momentum of a given particle and p_z is the component of momentum parallel to the beam direction. Further considerations to the design included requiring that tracks inside the angular acceptance must cross three or more VELO stations. For sensors with an outer active radius of 42 mm, the central modules should be spaced by less than 5 cm. Increasing this constraint to crossing four stations, to allow for missing hits in one of them, reduces the spacing of stations around the interaction point to 3.5 cm. To ensure that the full azimuthal acceptance was covered, the VELO halves had to overlap in the x-y plane. To achieve this, one half was shifted by 1.5 cm in the z direction with respect to the other side. This overlap can be seen in the bottom left of Fig. 2.5.

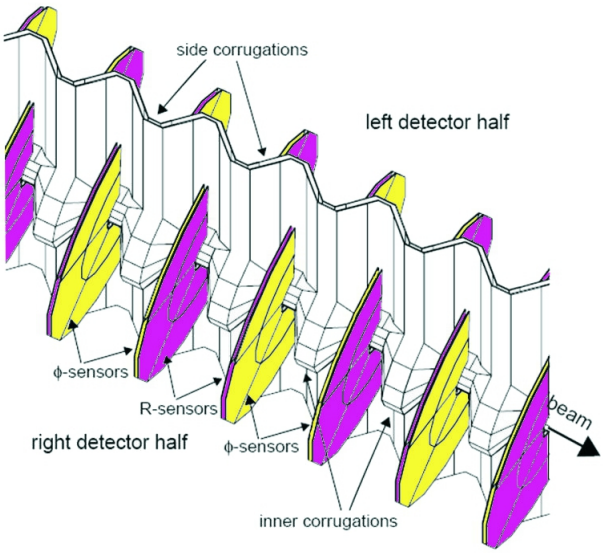

Figure 2.6: A close up to show the position of the VELO sensors with respect to the RF foil. The VELO is shown in the fully closed position. Reproduced from Ref. [58].

The sensors are positioned so close to the beam that they are inside the beam aperture of the LHC during injection. This means that the VELO modules must be able to move out of the way during injection and then close around the beam once it is declared stable. This is illustrated by the bottom of Fig. 2.5 where the sensors are shown in the open and closed positions. The closed position of the sensors is shown by Fig. 2.6 along with the RF foil, an aluminium foil designed to protect the VELO electronics from RF pickup induced by the beam. The modules are able to move up to 30 mm away from the interaction region during injection. They are then closed once the beams have been declared stable, with the first active strip 8.2 mm from the beam. The motion is performed by a stepping motor with an accuracy of 10 μm.

Sensors

The R and ϕ sensors are silicon micro-strip detectors, with a minimum pitch of 40 μm at the inner radius. Figure 2.7 shows the strip layout of the sensors and the properties are summarised in Tab. 2.1. The R sensors have a pitch running linearly from 40 μm at the inner radius to 102 μm at the outer radius. The strips are divided into 45° segments to reduce occupancy and capacitance.

The ϕ sensors have strips in two segments, again to reduce occupancy and also to decrease the pitch at the outer radius. To improve the pattern recognition,

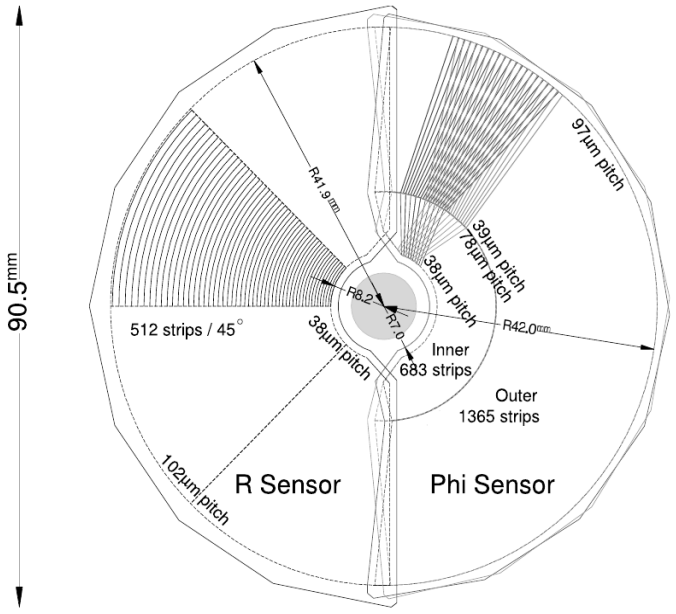

Figure 2.7: A sketch of the R (left) and ϕ (right) VELO sensors. There are two ϕ sensors overlaid to show opposite skew. Some strips are shown for each sensor, with the pitch labelled at the inner and outer radii. The sensitive areas of the sensors are identical; the larger size of the R sensor is due to a different arrangement of bonding pads. Reproduced from Ref. [58].

the strips are skewed away from the radial direction. This skew, or *stereo angle*, is shown in Fig. 2.7 and ϕ sensors of opposite skew are placed adjacently in the modules. The inner region has pitch 38 μm to 78 μm and the outer region 39 μm to 97 μm.

2.2.2 Ring imaging Cherenkov detectors

Particle identification is essential to LHCb because pions and kaons from B hadron decays must be separated. This will be a vital task to ensure the key physics channels such as $B \to DK^{(*)}$ can be reliably reconstructed. The LHCb detector includes two Ring Imaging Cherenkov detectors, RICH1 and RICH2, both of which are shown in Fig. 2.3. The use of two RICH detectors allows the full range of momenta to be covered. The upstream RICH1 detector covers the low momentum range of 1 to 60 GeV/c and the downstream detector, RICH2, covers the range from $\sim$15 GeV/c to over 100 GeV/c. Both RICH detectors focus Cherenkov radiation using flat and spherical mirrors on to Hybrid Photon Detectors (HPDs) that are positioned outside of the detector acceptance.

	R sensor	**ϕ sensor**
Number of sensors	42 + 4 (pile-up)	42
Readout channels	2048	2048
Sensor thickness	300 μm	300 μm
Smallest pitch	40 μm	38 μm
Largest pitch	102 μm	97 μm
Length of the shortest strip	3.8 mm	5.9 mm
Length of the longest strip	33.8 mm	24.9 mm
Inner radius of active area	8.2 mm	8.2 mm
Outer radius of active area	42 mm	42 mm
Angular coverage	182°	≈182°
Stereo angle (skew)	-	(10-20)°
Average occupancy	1.1%	1.1/0.7% inner/outer

Table 2.1: Characteristics of the two types of VELO sensors. Numbers taken from Ref. [58].

RICH1

RICH1 is located upstream of the magnet and consists of two radiators, one being aerogel and the other fluorobutane (C_4F_{10}). Figure 2.8 shows the layout of RICH1, along with an example Cherenkov light cone being focused. The design of RICH1 was influenced by several restrictions: minimising the material budget inside the LHCb acceptance required lightweight spherical mirrors and for all other optical components to be outside of the acceptance. The beryllium beam pipe limits the low angle acceptance to 25 mrad. Finally, the HPDs must be shielded from the magnet by a combination of iron and high permeability alloy shields.

RICH2

The downstream, RICH2, detector consists of a single CF_4 gas radiator and has a reduced acceptance of $\pm$120 mrad and $\pm$100 mrad in the horizontal and vertical planes respectively. The design, shown in Fig. 2.8, was guided by several restrictions: reducing the material budget forced all supports and HPDs outside the acceptance in addition to using secondary flat mirrors to reduce the total z length. The beampipe, and clearance around it, limits the lower angular acceptance to 15 mrad. HPDs are placed inside iron boxes to shield them from the LHCb dipole.

The HPDs used in both RICH detectors are vacuum photon detectors. Pho-

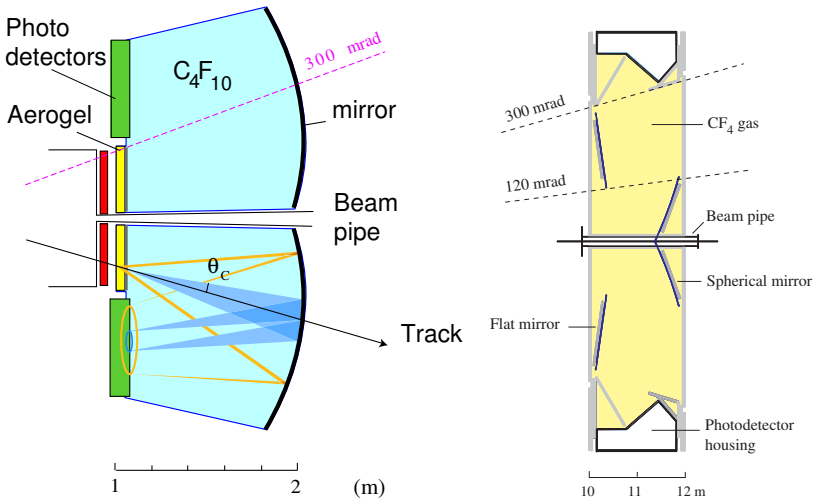

Figure 2.8: (Left) A side view schematic diagram of the RICH1 detector, with example photons to illustrate the focusing optics. The orange, larger, circle comes from the aerogel radiator and the smaller blue cone from the gas radiator. (Right) A top-down view schematic diagram of the RICH2 detector. Reproduced from Ref. [72].

toelectrons, released from a photocathode after it is struck by an incident photon, are accelerated by a high voltage of order 20 kV onto a silicon detector. LHCb uses, in total, 484 HPDs, with 196 and 288 in RICH1 and RICH2 respectively.

2.2.3 Tracking

Tracking in LHCb is split into three main sections, the VELO (section 2.2.1), the Silicon Tracker (ST) and the Outer Tracker (OT). The ST consists of two independent detectors, the Tracker Turicensis (TT) and the Inner Tracker (IT). The ST and OT will be discussed further in this section. Figure 2.9 shows the relative locations of the Tracker Turicensis, Inner Tracker and Outer Tracker.

Silicon Tracker

The ST includes two detectors, the Tracker Turicensis (TT) and the Inner Tracker (IT), both of which use silicon micro-strip sensors with an average pitch of approximately 200 μm. The TT is located upstream of the LHCb magnet, covering the full LHCb acceptance. It consists of four detection planes arranged in pairs separated by approximately 30 cm in the z direction. The second and third planes have a rotation of -5° and +5° respectively. Figure 2.10 shows the third detector plane of

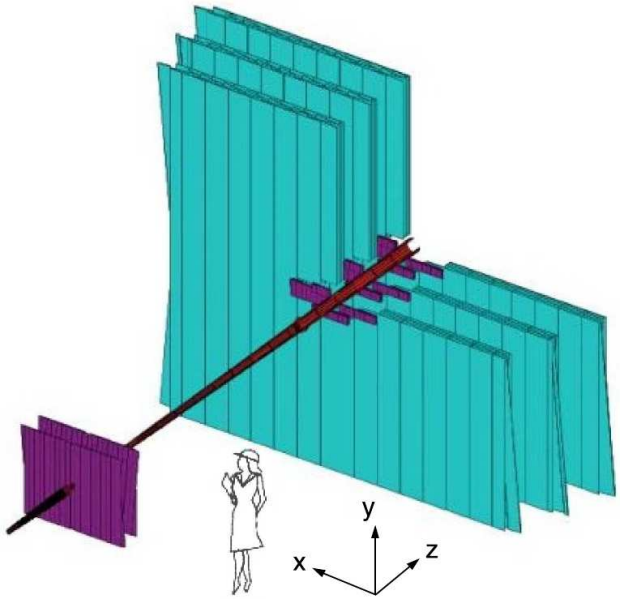

Figure 2.9: Layout of the tracking stations, the Tracker Turicensis is on the left in purple, the Inner Tracker on the right in purple and the Outer Tracker surrounding the Inner Tracker in blue. Reproduced from Ref. [58].

the TT that has the +5° rotation. Layers one and two have only seven half modules either side of the beam line whereas layers three and four have eight for projectivity reasons. There are two types of half modules; most of them have two readout sectors (L and M) but the six half modules closest to the beam have three readout sectors (K, L and M).

The IT consists of three stations downstream of the magnet, each with four detector layers. Like the TT, the second and third layers have a rotation by -5° and +5° respectively. Figure 2.11 shows two layers of an IT station. The IT does not cover the whole of the LHCb acceptance but an area close to the beampipe. Full angular coverage for the tracking stations T1 to T3, as labelled on Fig. 2.3, is provided by the OT.

Outer Tracker

The OT forms the outer part of the tracking stations with the IT as the inner part and so consists of three stations. It is a drift time detector to track charged particles over a wide range of angles. The OT uses arrays of straw-tube modules, as shown in Fig. 2.12. The straw-tubes are filled with Ar (70%) and CO_2 (30%) to provide a fast drift time and good position resolution of 200 μm. As with the ST stations,

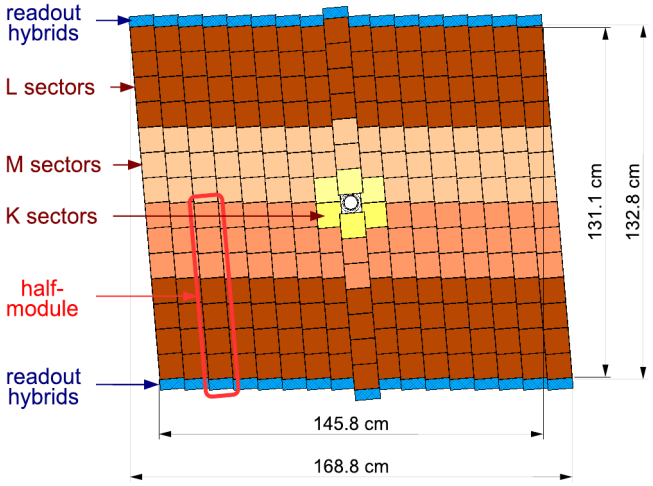

Figure 2.10: A diagram of the third layer of the TT detector layer. The shading represents different readout sectors. Reproduced from Ref. [58].

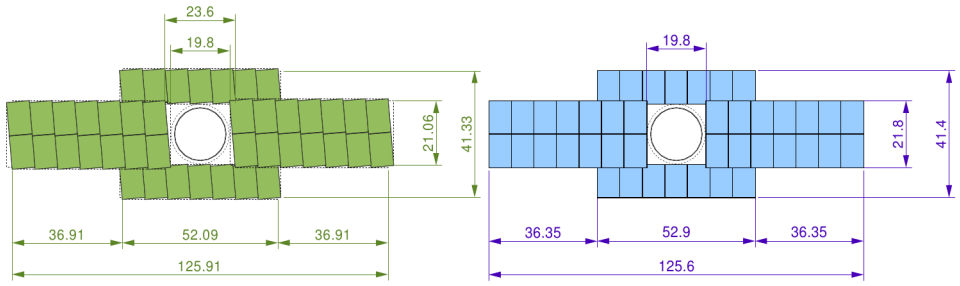

Figure 2.11: Layers of the IT detector with no rotation (right) and a +5° rotation (left). Reproduced from Ref. [73] and all measurements are shown in units of cm.

the OT stations each consist of four layers, with the second and third layers rotated by -5° and +5° to the vertical respectively.

2.2.4 Magnet

The LHCb experiment uses a warm dipole magnet to measure the momentum of charged particles. The warm magnet design was chosen over a super-conductor for financial reasons as well as a shorter construction period. The magnet consists of a vast rectangular iron yoke with two saddle shaped coils placed symmetrically inside the yoke, as shown by Fig. 2.13. The poles of the yoke are sloped to match the detector acceptance.

The magnet was designed to provide an integrated magnetic field of approx-

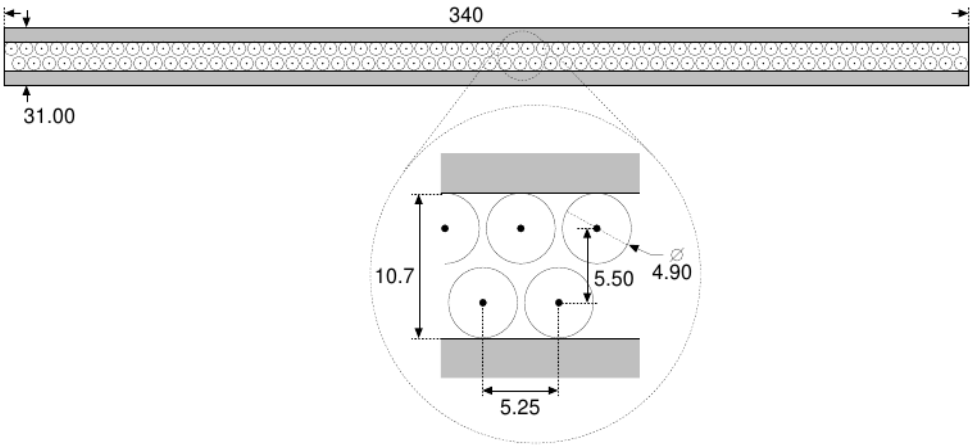

Figure 2.12: The layout of straw-tubes in an OT module, with a zoomed view to show the scale in mm. Reproduced from Ref. [58].

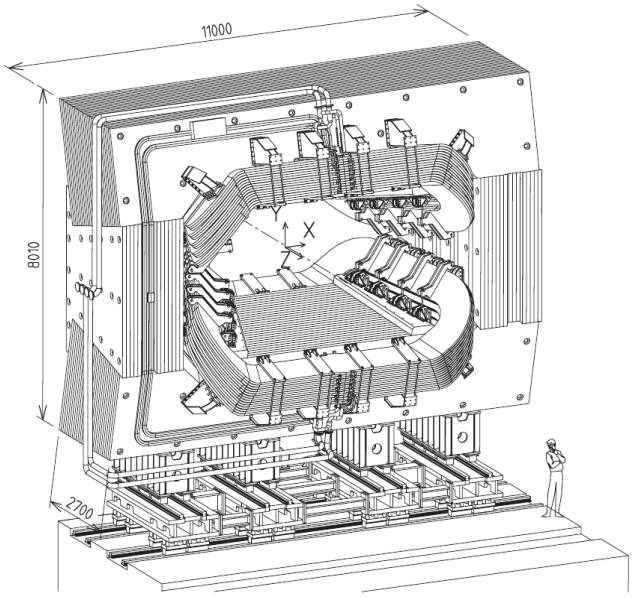

Figure 2.13: An illustration of the LHCb dipole magnet with the two saddle shaped coils inside the yoke. Measurements are in mm and the interaction point is behind the magnet. Reproduced from Ref. [58].

imately 4 Tm for 10 m long tracks. In addition the RICH detectors require very low field environments for the HPDs. HPDs accelerate electrons in a vacuum, so the presence of a magnetic field would cause the electrons to drift and degrade performance. The polarity of the magnet is reversible, allowing LHCb to run with

magnetic field up and down in polarity to study asymmetries.

2.2.5 Calorimeters

The calorimeter system at LHCb consists of four main elements, the Scintillator Pad Detector (SPD), PreShower detector (PS), Electromagnetic CALorimeter (ECAL) and Hadron CALorimeter (HCAL). These four parts are all labelled on Fig. 2.3. The SPD, PS and ECAL are designed to measure the energy of electrons and photons whereas the HCAL measures the energy of hadrons. The hardware electron trigger is designed to reject 99% of inelastic pp collisions in addition to providing a factor 15 enrichment in B hadron events. This makes electron identification very important, and as a consequence electrons of high transverse energy, E_T are selected. The quantity E_T is the energy of a particle perpendicular to the beam direction

$$E_T = \sqrt{E_x^2 + E_y^2}, \tag{2.3}$$

where x and y are the two directions perpendicular to the beam direction. Additionally, information from the calorimeters is used by the hardware level photon and hadron triggers. The latter is very important for studying hadronic decays of B hadrons.

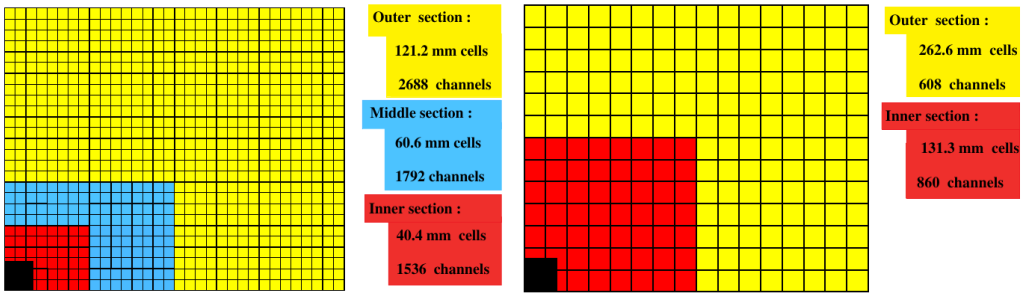

Figure 2.14: Segments in the ECAL, PS and SPD (left) and HCAL (right). One quarter of the detector front face is shown. The black regions are the gap for the beampipe. The dimensions on the left plot are from the ECAL. The SPD and PS are slightly smaller for projection reasons. Reproduced from Ref. [58].

Each part of the calorimeter system has a variable segmentation, with smaller cells closer to the beam line. This is due to hit densities varying by a factor 100 over the face of the modules. Figure 2.14 shows the segmentation chosen for the ECAL (left) and HCAL (right). Three sizes were chosen for the ECAL and, therefore, projectively for the PS and SPD. The HCAL has two sizes, each of those larger than

any ECAL cell, due to the dimensions of hadronic showers. The whole calorimeter system is built in halves that can be opened to get access to the detector.

Each calorimeter uses a Photo-Multiplier Tube (PMT) to detect scintillation light from a particle interaction in the material, collected by wave-length shifting (WLS) fibres. The PS and SPD cells have single fibres connected to a multianode PMT for read out, whereas the ECAL and HCAL modules require a PMT for their fibre bunches. The gain of the PMTs for the ECAL and HCAL are set in accordance to the distance from the beampipe to keep the E_T scale constant.

PS and SPD

The PS and SPD are used in conjunction with the ECAL to separate electrons and photons from pions, a critical task to provide information for the hardware electron and photon triggers. The SPD is also used to measure the number of charged tracks per interaction, which is used to veto events with too many tracks during offline analysis. The PS allows for a separation of electromagnetic showers in the z direction, providing a method to reject the background of charged pions based on the shower shapes in the PS and ECAL. Only charged particles interact in the SPD, which provides a method to separate photons and electrons by matching deposits in the PS and ECAL with the SPD. Given these rejection methods, the SPD is upstream of the PS which is also upstream of the ECAL. The detectors are both high granularity scintillator pads with a 15 mm lead converter between them. To achieve a one to one correspondence with the ECAL, both the PS and SPD are segmented in the same way. The projectivity requirement also forced the SPD detector to be smaller than the PS in all dimensions by about 0.45 %.

ECAL

The ECAL is split into three sections; inner, middle and outer, due to the hit density varying strongly with distance from the beampipe. Table 2.2 shows the parameters of the cells and modules located in each of the three sections. Each module is built from layers of lead alternated with scintillator tiles acting as absorber and active medium respectively. The lead layers are 2 mm in thickness and the polystyrene scintillator tiles are 4 mm thick, with 66 of each in a single module. The stacks are wrapped in black paper to ensure that they are light tight. The acceptance of the ECAL almost matches that of LHCb; 25 mrad to 250 mrad in the vertical plane. The inner acceptance is limited by the high radiation environment close to the beam.

	Section		
	Inner	**Middle**	**Outer**
Inner dimension (cm^2)	65 × 65	194 × 145	388 × 242
Outer dimension (cm^2)	194 × 145	388 × 242	776 × 630
Cell size (cm^2)	4.04 × 4.04	6.06 × 6.06	12.12 × 12.12
# of modules	176	448	2688
# of channels	1536	1792	2688
# of cells per module	9	4	1
# of fibres per module	144	144	64
Fibre density (cm^{-2})	0.98	0.98	0.44

Table 2.2: Parameters of the ECAL to compare the different sub-sections. The areas are all $x \times y$. Numbers taken from Ref. [58].

HCAL

The HCAL is similar to the ECAL, with tiles of polystyrene scintillator and iron as the absorber. Like the ECAL, it has a modular design with alternating layers of scintillator and absorber. Each layer is 10 mm thick and has a spine of 6 mm iron and alternating tiles of scintillator and 4 mm lead plates. To prevent dead areas adjacent layers alternate the pattern of lead and scintillator tiles. Figure 2.15 shows the layer structure used to build the HCAL modules, each consisting of 432 individual layers. A special feature of the HCAL is that the scintillator tiles are oriented parallel to the beam axis. The HCAL also extends much further in the z direction than the ECAL, reflecting the size of the showers it must contain.

2.2.6 Muon system

Muon identification is a vital function of LHCb in order to study some of the key CP sensitive decay channels, such as $B^0 \to J/\psi(\mu^+\mu^-)K^0_S$. The muon system must provide fast information on the muon transverse momentum, p_T, for the hardware high-p_T muon trigger and muon identification for the software trigger and offline software. Similarly to E_T, p_T is defined as the momentum of the particle perpendicular to the beam direction.

The muon system is composed of five rectangular stations, M1-M5, positioned perpendicular to the beampipe. The first station, M1, is positioned before the calorimeters to improve the transverse momentum measurement for the muon trigger. The remaining four stations are downstream of the HCAL and are sepa-

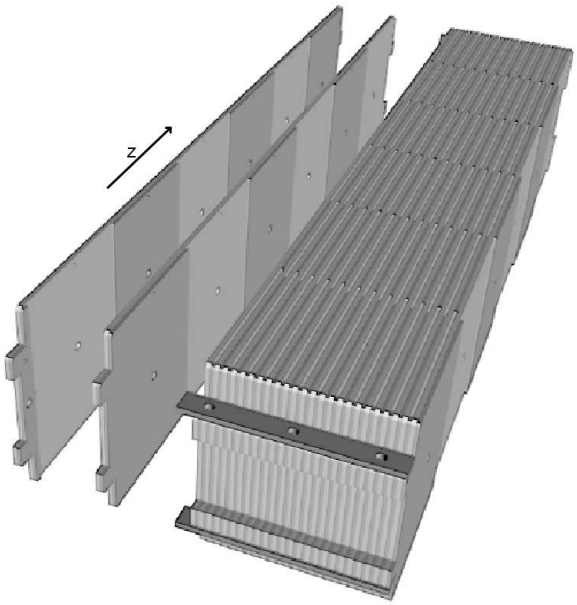

Figure 2.15: An illustration of the layer structure of the HCAL. The lighter regions are spaces for the scintillator tiles. Reproduced from Ref. [74].

rated by 80 cm thick iron absorbers to select penetrating muons of high momentum. Muons with momentum greater than roughly 6 GeV/c will reach the 5th muon station, M5. The detailed layout of the muon system is shown by Fig. 2.16, and a more general view of the muon system can be seen in Fig. 2.3. The muon stations increase in size from M1-M5 to keep the acceptance of each muon station from 20 (16) mrad to 306 (258) mrad in the bending (non-bending) frame.

M1 to M3 have good spatial resolution in the x direction, the bending plane, to measure the track direction and determine the transverse momentum of the candidate. Stations M4 and M5 have a much simpler task, to identify particles that manage to penetrate the iron absorbers between stations.

The muon stations are divided into four regions of varying chamber and logical pad size, with smaller chambers close to the beamline and larger ones as the distance increases, with three different sizes in total. The readout of all chambers except the inner region of M1 uses Multi-Wire Proportional Chambers (MWPC). The particle rate at the centre of M1 is too high so triple Gas Electron Multiplier (GEM) detectors are used instead.

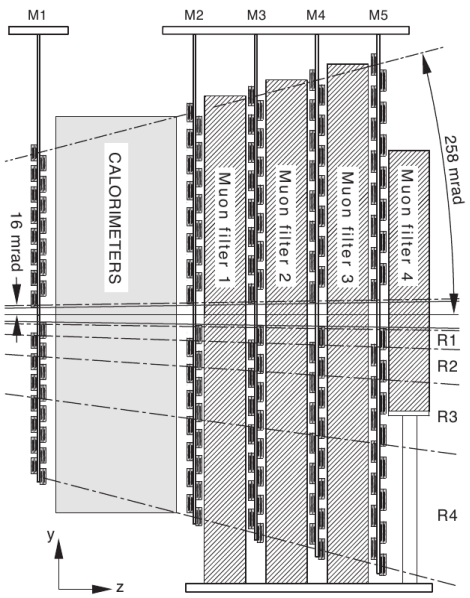

Figure 2.16: A side view of the muon system where the iron absorbers are labelled as muon filters, reproduced from Ref. [58].

2.2.7 Trigger

Designed to operate at an average luminosity of 2×10^{32} cm^{-2}s^{-1}, the LHCb experiment must reduce the data rate to something suitable to write the data to tape. In fact during 2011 the luminosity reached was around 4×10^{32} cm^{-2}s^{-1}. The data used in this thesis was taken at an average luminosity of approximately 3×10^{32} cm^{-2}s^{-1}. At the design luminosity single interactions dominate the bunch crossings, which helps the triggering and reconstruction by reducing the number of particles to reconstruct. Despite this, the rate of visible interactions to LHCb is approximately 10 MHz, which must be reduced to about 3 kHz by the trigger system.

The LHCb trigger is broken down into two trigger levels, Level-0 (L0) and the High Level Trigger (HLT). The L0 trigger is a hardware trigger and the HLT trigger is a software trigger. The software trigger consists of two stages, HLT1 and HLT2. A simple flow diagram of the trigger stages, including some examples of the trigger channels, can be seen in Fig. 2.17. The hardware trigger is designed to reduce the LHC beam crossing rate of 40 MHz down to 1 MHz at which the whole detector can be read out and passed to the software trigger. Given the nature of B meson decays the hardware trigger focuses on high E_T particles and high p_T muons. The software must then reduce the 1 MHz rate to approximately 3 kHz using additional

information from the VELO and tracking stations.

There are two methods by which an event can fire one of the trigger selections. Firstly, the signal B meson candidate decay can cause a trigger to fire. Secondly, the other B meson in the event can cause a trigger to fire, independently of the signal candidate. These methods are not exclusive, since both the signal candidate and the other B meson in the event can cause the trigger to fire.

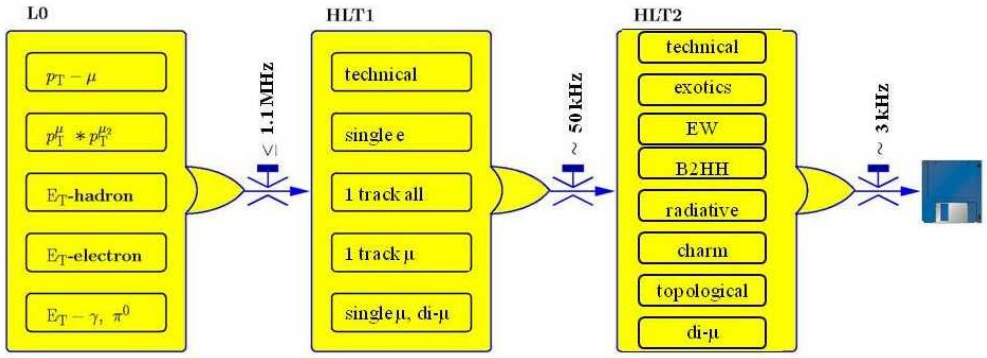

Figure 2.17: A flow diagram to show the trigger sequences and the data rates associated with each step. Reproduced from Ref. [75].

Hardware trigger

The hardware trigger consists of three components; the pile-up system, the hardware calorimeter trigger and the hardware muon trigger. Each of the components takes data from a single subdetector and the L0 decision unit collects the information and makes the final L0 decision per bunch crossing.

The hardware calorimeter trigger looks for electrons, photons and hadrons with high E_T, where particle identification is performed by combining information from the SPD, PS, ECAL and HCAL. The E_T of all HCAL cells is summed to veto crossings with no visible interactions and the total number of SPD cells with a hit is summed to measure charged track multiplicity.

The hardware muon trigger selects the two muons of highest p_T in each quadrant of the muon stations. Tracks are found in the muon stations by combining the clusters in each muon station and pointing back towards the interaction point.

Software trigger level 1

During early data taking, HLT1 operated in *alleys*, where each alley corresponds to an L0 trigger type. Some candidates will have passed several hardware triggers and hence must pass through several alleys. The VELO and tracking stations were used to confirm or reject the hardware trigger decision. L0 objects were confirmed in position and momentum by reconstructing seeds from the tracking stations along the trajectory defined by the L0 object. The VELO seeds were done in two stages, first R sensors and then ϕ sensors were only used if the 2D R tracks matched well with the L0 object. A final stage was to match both the VELO and tracking station information by matching VELO seeds to tracking station seeds and vice-versa.

With high luminosity runs and higher pile-up events with more than one interaction per bunch crossing, in 2011 a different approach was required. A single track trigger [76] was introduced to efficiently select hadronic decays of B and D mesons, and replaced many of the old HLT1 trigger alleys. This was an important change in order to remain inside the 12 ms per event timing budget. B mesons typically fly, of order, 10 mm from the interaction point and are strongly boosted in the z direction with momenta of order 100 GeV/c. Therefore, the software trigger looks for a single decay product track with high momentum, high transverse momentum and large impact parameter with respect to the interaction point. This is an important trigger in the scope of the measurement of the $B^0 \to \bar{D}^0 K^+ K^-$ branching fraction presented in this thesis. It should be noted that the single track trigger no longer makes reference to L0 objects to confirm or reject them.

The other HLT1 trigger selections, such as single muon and di-muon, can be seen in Fig 2.17.

Software trigger level 2

The total output rate of HLT1 must be low enough to allow for an offline track reconstruction to be performed. The software trigger track fits do not use a Kalman filter [77] to give a full covariance matrix since it is too CPU intensive for this stage. The tracks are subjected to very loose selection requirements on momentum and impact parameter before using them to create particles, such as ϕ from K^+ and K^-. These particles are then used to create the final states, where invariant mass and B momentum direction requirements are applied to the final selections. At the end of this stage the rate must be around 3 kHz for data to be written to disk for analysis.

With regards to this thesis, the most important trigger selections in the

HLT2 are the topological lines. They are designed to trigger efficiently on B decays including two or more charged tracks. For more details on the implementation of the topological triggers see Ref. [78].

2.2.8 Online system

The online system is responsible for the transfer of data from the front-end electronics to the storage disks. An important task is to ensure that all detector channels are synchronised with the LHC clock. The three parts of the online system are; the Data AcQuisition (DAQ) system, the Timing and Fast Control (TFC) system and the Experiment Control System (ECS). Figure 2.18 shows how these components interact with the experiment and each other.

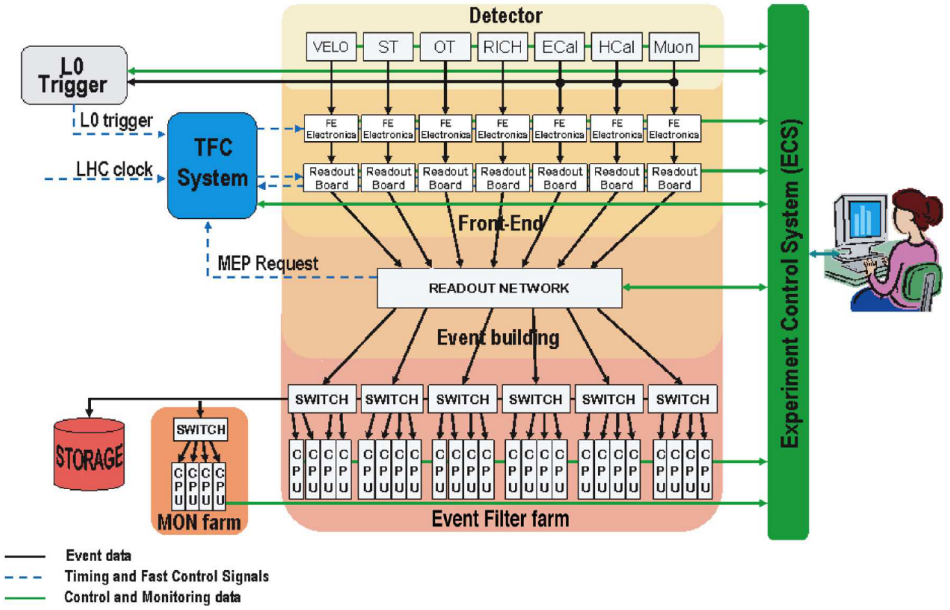

Figure 2.18: An overview of the online system showing how the different components interact with each other. Reproduced from Ref. [58]

DAQ system

The DAQ system must transport the data from a given bunch crossing, that has been identified by the trigger, from the front-end electronics to the storage disks. Data is read out from all the subdetectors, except RICH1 and RICH2, using TELL1 boards [79]. RICH1 and RICH2 use a specialised board [80] that is, from a read out point of view, identical to the TELL1. This is then processed by the trigger system

and written to permanent storage only if it is accepted by the trigger.

TFC system

The TFC is responsible for driving each stage of the data readout of the LHCb detector from the front-end electronics all the way down to the online processing farm. This is achieved by broadcasting the beam-synchronous clock, synchronous resets, fast control commands and the L0 trigger.

ECS

The ECS is responsible for the running, control and monitoring of the whole LHCb detector. The trigger, TFC system and DAQ systems are monitored and controlled by the ECS. In addition, settings and monitoring of more general parameters such as voltages, pressures and temperatures are the responsibility of the ECS.

2.2.9 Software

Event generation and detector simulation

The Gauss package is the simulation software used to create simulated data at LHCb. It consists of two phases, the generation phase and the simulation phase. The generation phase is responsible for generating particles and decaying them. PYTHIA [81] is used to create the initial proton - proton collision and then EvtGen [82, 83] is used to decay the particles in B hadron events. To generate signal samples, users provide a decay file that informs EvtGen which particles are required and how to decay them. More generally, EvtGen uses a generic decay file to store information about the decays of all particles that it can decay. This file contains thousands of branching fractions and must be kept up to date.

The simulation phase of Gauss uses `GEANT4` [84] and the detector description database (DDDB) to simulate the passage of particles through the LHCb detector. The DDDB stores the geometry of the detector which is used in the simulation and also in the reconstruction of real data. For example, information on size, materials and location of each detector component is stored. One of my responsibilities on LHCb was to improve the description for the VELO subdetector, and this work is summarised in Appendix A

Digitisation of simulated data

Boole is responsible for digitising the output from the simulation phase of Gauss and it forms the second stage in the simulation of LHCb. The output of Boole is in the same format as real data read directly from the experiment, with LHC background and detector response included.

Event reconstruction

Brunel is the event reconstruction application used at LHCb, it can process real data from the LHCb DAQ system or the output of Boole for simulated data. Brunel acts as the final stage of the simulation and gets both real data and simulated data ready for analysis. Brunel takes the digital data from Boole or LHCb and turns it into useful information by fitting tracks to calculate particle properties.

Physics analysis

DaVinci is an analysis software package that is used to study both real and simulated data. Selections are used to find the decay chains that are of interest to the user and then a ROOT [85] ntuple is created containing the events. Many tools are available to calculate quantities such as kinematic, event and particle identification variables from the track objects created by Brunel. Selection requirements may also be applied to the candidates before the output is written.

Bender is an analysis environment that allows the user to utilise other parts of the software, such as DaVinci. It is the primary tool used to create the datasets used in this thesis. It allows for simple use of other tools, such as performing a new vertex fit whilst constraining the mass of a particle.

Particle identification calibration

PIDCalib is a software tool used to calculate the efficiency of a particle identification requirement on Delta Log Likelihood (DLL) variables at LHCb. These variables are computed by combining information from the RICH, calorimeters and muon systems. The quantity of interest for this thesis is $\mathrm{DLL}_{K\pi}$, which is used to separate kaons from pions. This quantity, $\mathrm{DLL}_{K\pi}$, is defined as

$$\mathrm{DLL}_{K\pi} = \ln L(K) - \ln L(\pi)\,, \tag{2.4}$$

where $L(K)$ ($L(\pi)$) is the likelihood that the particle is a kaon (pion). Therefore, $\mathrm{DLL}_{K\pi}$ can be used to discriminate between kaon-like and pion-like particles. The

efficiency of kaon identification at LHCb as a function of particle momentum is shown by Fig. 2.19. The figure also shows the efficiency of misidentifying a pion as a kaon. Note that the solid points show the efficiency after a requirement of $\mathrm{DLL}_{K\pi} > 5$, which is the nominal value used in this anaylsis. See Sec. 3.5.3 for details.

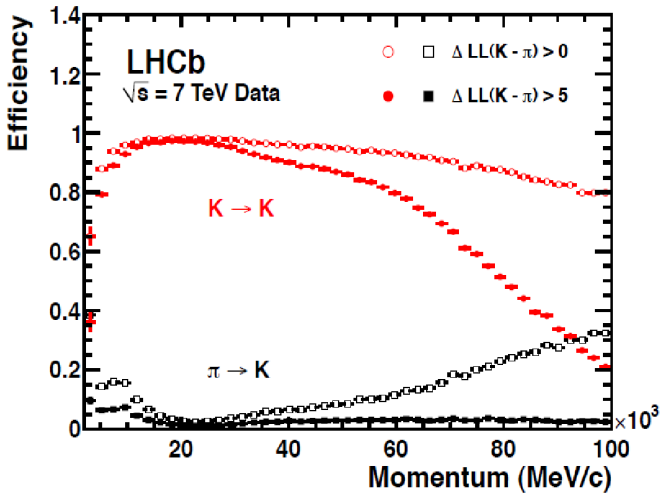

Figure 2.19: Efficiency of kaon identification (red) and pion misidentification (black) as a function of particle momentum. The hollow (solid) points show the result of a requirement of $\mathrm{DLL}_{K\pi} > 0$ (5). Taken from Ref. [86].

Calibration datasets are formed using decays that can be tagged without using particle identification information on the track of interest. The calibration sample used in this analysis was $D^{*+} \to D^0\pi_s^+$ with $D^0 \to K^-\pi^+$. Using the calibration data, PIDCalib can be used to calculate the efficiency of a given particle identification requirement in terms of p and p_T for a given track. This builds up an efficiency map for a given particle type. The efficiency is calculated using the pure calibration sample by comparing the number of events before and after the $\mathrm{DLL}_{K\pi}$ requirement is applied. This efficiency map can then be used to calculated the particle identification efficiency for each event in a (simulated) data set.

Chapter 3

Data samples and selections

This chapter will describe the data samples used in this analysis and explain how the raw data from the experiment were reduced and selected into the final data samples for analysis. Some of these steps have been described generally in Sec. 2.2.7 and Sec. 2.2.9 for the trigger and software respectively. The data used in this thesis were taken in 2011 by the LHCb experiment at the LHC. The sample used corresponds to an integrated luminosity of 0.62 fb^{-1}.

3.1 Analysis outline

The analysis presented here and in the coming chapters is a measurement of the ratio of branching fractions

$$\frac{\mathcal{B}(B^0 \to \bar{D}^0 K^+ K^-)}{\mathcal{B}(B^0 \to \bar{D}^0 \pi^+ \pi^-)}, \tag{3.1}$$

where $B^0 \to \bar{D}^0 K^+ K^-$ is the mode to be observed and $B^0 \to \bar{D}^0 \pi^+ \pi^-$ is used as a reference mode whose branching fraction is known experimentally. Additionally, the $B_s^0 \to \bar{D}^0 K^+ K^-$ decay mode is considered by measuring the ratio of branching fractions

$$\frac{\mathcal{B}(B_s^0 \to \bar{D}^0 K^+ K^-)}{\mathcal{B}(B^0 \to \bar{D}^0 K^+ K^-)}. \tag{3.2}$$

The decay mode of the D meson used in this analysis is $D \to K\pi$. LHCb is well suited to study these decay modes because both final states involve only charged kaons and pions. Here and throughout this thesis the h tracks in the Dh^+h^- final states are referred to as bachelors.

In the following chapters the two final states will be abbreviated as DKK and $D\pi\pi$. The measurement of ratios of branching fractions means that many sources

of systematic uncertainty will be common between the two decay modes and hence cancel. The world average (Tab. 1.7) of $\mathcal{B}(B^0 \to \bar{D}^0\pi^+\pi^-)$ may then be input to extract a value for $\mathcal{B}(B^0 \to \bar{D}^0 K^+ K^-)$.

The signal peak was seen during an initial investigation into all of the Dhh modes at LHCb to determine which measurements may have been possible and to estimate yields. An introduction to Dhh modes is provided in Sec. 1.7. Once the peak was observed in $B^0 \to \bar{D}^0 K^+ K^-$ it was clear that this was the most interesting study to perform on the early LHCb data. A peak in the DKK mode was not expected, because decays where $s\bar{s}$ quarks are produced in the final states should be suppressed. One final point is that the final state in this analysis does not distinguish between B flavour, so that both $B^0 \to \bar{D}^0 K^+ K^-$ and $\bar{B}^0 \to \bar{D}^0 K^+ K^-$ could contribute. However, the $\bar{B}^0$ decay would require a $b \to u$ transition rather than $b \to c$, to create the same flavour of D meson, and is therefore expected to be suppressed to a negligible level.

3.2 Trigger requirements

This analysis has trigger requirements from both the hardware trigger and the software trigger level 2. To pass the software trigger requirements, events must have fired on at least one of the multibody topological trigger selections. These topological trigger selections consider the kinematics of events using a boosted decision tree. The names of the selections are:

- `Hlt2Topo2BodyBBDT_TOS`;
- `Hlt2Topo3BodyBBDT_TOS`;
- `Hlt2Topo4BodyBBDT_TOS`.

The software trigger requirements are applied during the initial selection phase. These requirements mean that the signal decay must have been responsible for firing the trigger. For more information on the topological trigger selections please see Sec. 2.2.7.

After the full selection has been applied, a hardware requirement is applied such that events must satisfy at least one of two trigger selections. These are a hadronic trigger on the signal decay or a more general global trigger on the rest of the event, known as `L0Hadron_TOS` and `L0Global_TIS` respectively.

3.3 Stripping selection

The concept of *stripping* at LHCb is to break down the vast dataset from the LHCb detector into streams that are ready to be used in data analyses. The stripping is run over the reconstructed data, using `DaVinci`, and splits the recorded events into streams, such as b hadron events or electro-weak events. Each stream is fed by many stripping selections, which are algorithms designed to search for specific decay channels in the data sample. In this analysis it is the `Bhadron` stream that is important.

Each stripping selection has a set of requirements that are applied, in order to select which events are stored to the stream. The important stripping selection for this thesis is called `B2DXWithD2hhLine`. This accepts decays of the form $B \to Dh$ and $B \to Dhh$ with $D \to hh$, where h stands for a kaon or pion. No invariant mass requirements are applied to combinations of the selected daughter particles. Therefore, the `B2DXWithD2hhLine` stripping line provides unbiased data samples for $B \to \bar{D}^0 K^+ K^-$ and $B \to \bar{D}^0 \pi^+ \pi^-$ with regards to phase space.

The data samples used cover two separate stripping versions, `Stripping13b` and `Stripping15`. The requirements applied by the `B2DXWithD2hhLine` stripping selection in the two different versions are shown in Tab. 3.1. The following quantities are used to select a B candidate: reconstructed mass, $m^{\text{reco}}_{B^0}$; reconstructed lifetime, $\tau_{\text{reconstructed}}$; minimum χ^2 of the impact parameter with respect to any primary vertex, $\min_{\text{PVs}} \chi^2_{\text{IP}}$; quality of the B vertex fit, $(\chi^2/\text{ndf})_{\text{vertex}}$; and the cosine of the angle between the B momentum and the line between the primary vertex and the B vertex, $\cos$ (Dir. angle w.r.t own PV). While D candidates are selected using many of the same quantities described for the B candidates, the additional quantities are: transverse momentum, p_T; the maximum distance of closest approach between the D daughters, $\max_{\text{daughters}}$ (D.O.C.A.); the maximum χ^2 of the impact parameter with respect to the primary vertex of the two D daughter tracks, $\max_{\text{daughters}} \chi^2_{\text{IP w.r.t. PV}}$; and the χ^2 of the decay distance from the primary vertex, $\chi^2_{\text{flight w.r.t. best PV}}$. The bachelor tracks and the D daughters are selected during the stripping using the quantities already described above.

The stripping versions are consistent except for the Global Event Cut (GEC) on the maximum number of long tracks in the event. Long tracks are the best quality tracks for physics analysis because they utilise information from all of the tracking detectors; the VELO, TT and tracking stations.

Particle	Parameter	Requirement
B^0	$m^{\text{reco}}_{B^0}$	$< m^{\text{PDG}}_{B^0_s} + 500$ MeV/c^2
	$m^{\text{reco}}_{B^0}$	$> m^{\text{PDG}}_{B_0} - 500$ MeV/c^2
	$\tau_{\text{reconstructed}}$	> 0.2 ps
	$\min_{\text{PVs}} \chi^2_{\text{IP}}$	< 16
	$(\chi^2/\text{ndf})_{\text{vertex}}$	< 9
	cos (Dir. angle w.r.t own PV)	> 0.9999
D^0	p_T	> 1000 MeV/c
	$\lvert m^{\text{reco}}_{D^0} - m^{\text{PDG}}_{D^0} \rvert$	< 100 MeV/c^2
	$(\chi^2/\text{ndf})_{\text{vertex}}$	< 6
	$\chi^2_{\text{flight w.r.t. best PV}}$	> 100
	cos (Dir. angle w.r.t own PV)	> 0.9
	$\max_{\text{daughters}}$ (D.O.C.A.)	< 0.6 mm
	$\max_{\text{daughters}} \chi^2_{\text{IP w.r.t. PV}}$	> 40
D daughters	p_T	> 250 MeV/c
	p	> 2000 MeV/c
	$\min_{\text{PVs}} \chi^2_{\text{IP}}$	> 4
	χ^2_{track}	< 4
Bachelor track	p_T	> 250 MeV/c
	p	> 2000 MeV/c
	$\min_{\text{PVs}} \chi^2_{\text{IP}}$	> 4
	χ^2_{track}	< 4
Global Event Cut	$N_{\text{long tracks}}$	< 150 (500)

Table 3.1: Requirements imposed on the data sample in the `B2DXWithD2hhLine` stripping selection. Only the GEC differs between `Stripping13b` and `Stripping15`: the first (second) number given is for the former (latter).

3.4 Constraining masses in the vertex fit

Dalitz plots are defined by the invariant masses of the particles in the decay chain. Equation 1.40 in Sec. 1.5.1 shows the relationship between the Dalitz plot axis variables and the invariant masses of each particle. It is important to note that the masses of B and D mesons appear in the equation. Experimentally, the masses of the B and D mesons will be reconstructed from the decay daughters that are detected at LHCb. However, due to detector resolutions these masses will obey a Gaussian distribution and not a perfect delta function. As a result of this, each event has a slightly different Dalitz plot definition, which causes the boundary of

the plot to become smeared and unphysical.

A method to eliminate this problem is to constrain both the B and D meson masses to their world average values when the kinematic fit is performed. In fact it is the daughters of the B and D mesons that are constrained to have an invariant mass consistent with the true meson mass. It is not just a matter of changing the mass of the particles as an afterthought. This procedure only works for events that really do include a B and D meson. In some cases it is impossible to constrain the daughters, and these events are discarded since they are by definition background events. Events failing the fully constrained fit from the DKK and $D\pi\pi$ final data samples are shown in Fig. 3.1. Events with $m(Dhh)$ far from the value of $m(B)$ used to constrain the fit are more likely to fail.

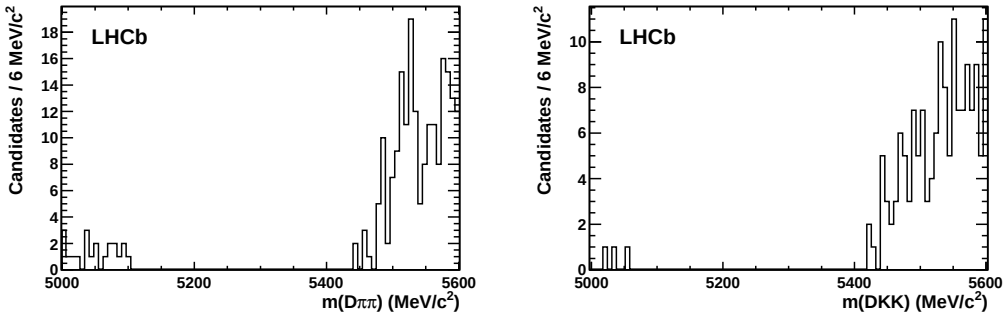

Figure 3.1: B candidate mass distribution for $D\pi\pi$ (left) and DKK (right) candidates that fail the B and D mass constrained vertex fit.

Figure 3.2 shows the effect of constraining the masses of the B and D mesons in the vertex fit. Both plots in the figure show exactly the same events before (left) and after (right) the refit. The data shown are from the $B^0 \to \bar{D}^0\pi^+\pi^-$ data sample before the full selection was applied. It is clear to see that the plot on the right is much sharper and that the edges are well defined. The unconstrained plot on the left has fuzzy edges where many events appear in the kinematically forbidden region. A full set of quantities were saved following the constrained fit, using the `Bender` software package, to be used in the selection described in Sec. 3.5.

A second set of quantities were produced using just a D mass constraint. This improves the resolution of the B mass and is used in the measurements presented in this thesis. These quantities are used when it is required to perform a fit to the B mass distribution.

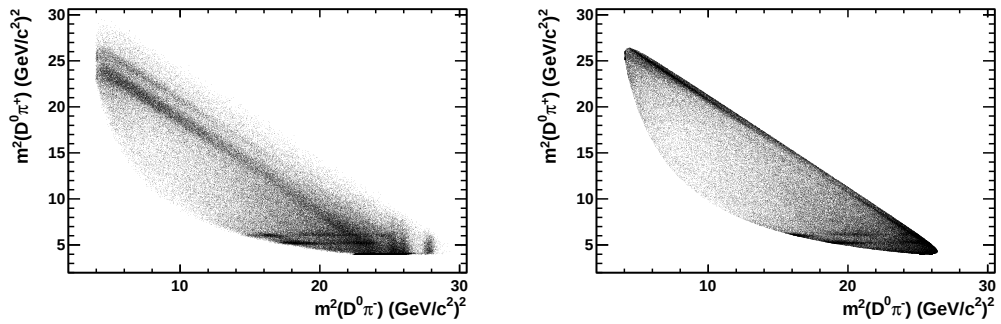

Figure 3.2: Dalitz plots from the $B^0 \to \bar{D}^0\pi^+\pi^-$ data sample to show the effect of constraining the B and D meson masses in the vertex fit, without constraints (left) and with constraints (right). Note that events failing the constrained vertex fit are not shown in either plot.

3.5 Selection

The selection of events for both $D\pi\pi$ and DKK is done in several stages. The aim of the selection is to reduce backgrounds as much as possible while keeping the number of signal events as high as possible. The starting point is an initial selection that is applied to data that is taken directly from the stripping selection. This selection reduces the backgrounds in the $D\pi\pi$ data sample enough so that signal and background samples are distinguishable, which allows a neural network to be trained to separate signal candidates from background candidates. Some further requirements such as vetoes and particle identification are also described.

3.5.1 Initial selection

The initial selection is based on the selection documented in Ref. [56], except that the requirements on the final state vector particle were removed to preserve the full kinematic region of the decay modes. Note that Ref. [56] corresponds to the final state $DK\pi$ but the topology is similar to both DKK and $D\pi\pi$. The aim of this selection is to reduce background in both $D\pi\pi$ and DKK modes such that a neural network can be used. Since the neural network is trained on $D\pi\pi$ data it is vital that signal candidates can be separated from background candidates in order to train it. Where possible, quantities from the D mass constrained fit are used, as described in Sec. 3.4. A summary of the requirements applied in the initial selection is shown in Tab. 3.2. The selection requirements for B and D candidates are to

tighten the requirements on some of the quantities used in the stripping. The two D daughters and the two bachelor particles have two additional selection criteria. Firstly, a particle identification requirement is applied using a delta log-likelihood quantity, $\mathrm{DLL}_{K\pi}$, that represents the difference in log-likelihood for a particle to be a kaon compared to a pion hypothesis. Secondly, there is a requirement to eliminate tracks that are likely to be clones using the Clone flag quantity. Two tracks are considered to be clones if they provide the same information as each other.

Particle	**Parameter**	**Cut Value**
B^0	†M	> 5000 and < 5600 MeV/c^2
	$(\chi^2/\mathrm{ndf})_{\mathrm{vertex}}$	< 4
	$^\dagger \cos$(Dir. angle w.r.t own PV)	> 0.99995 (angle < 10 mrad)
	$^\dagger \mathrm{min}_{\mathrm{PVs}}\, \chi^2_{\mathrm{IP}}$	< 9
D^0	M	> 1844 and < 1884 MeV/c^2
	$^\dagger (\chi^2/\mathrm{ndf})_{\mathrm{vertex}}$	< 5
	$^\dagger \mathrm{min}_{\mathrm{PVs}}\, \chi^2_{\mathrm{IP}}$	> 4
D^0_K	$\mathrm{DLL}_{K\pi}$	> 0
	Clone flag	> 10000
D^0_π	$\mathrm{DLL}_{K\pi}$	< 4
	Clone flag	> 10000
$^*K$	$\mathrm{DLL}_{K\pi}$	> 5
	Clone flag	> 10000
$^{**}\pi$	$\mathrm{DLL}_{K\pi}$	< 3
	Clone flag	> 10000

Table 3.2: Requirements used at the initial selection stage. Requirements labelled * are only used for the DKK data sample, while requirements labelled ** are from the $D\pi\pi$ selection. Parameters labelled † are calculated after a D mass constrained fit.

3.5.2 Using a neural network

`NeuroBayes` [87, 88], a neural network package, is used in this study to remove as much of the combinatorial background as possible. Due to the relatively small $B^0 \to \bar{D}^0 K^+ K^-$ data sample, the neural network was trained using $B^0 \to \bar{D}^0 \pi^+ \pi^-$ data, which has an almost identical topology. The neural network was only trained using events in the B mass region of 5200 to 5600 MeV/c^2. The lower limit is set rather high at 5200 MeV/c^2 because this prevented the neural network being trained

on signal-like partially reconstructed backgrounds, which contribute to the low mass region.

In order to train the neural network, `NeuroBayes` must be provided with a list of variables that can be used to distinguish signal and background events. These include some of the variables used in the initial selection as well as some extra variables. Those quantities that have not been used until the neural network training include the transerve momentum of the B candidate. The "cone" variables are created by summing the momentum and number of tracks inside a cone drawn around the B candidate momentum vector, for $p_{T\,\mathrm{asym}}$ and $\mathrm{track}_{\mathrm{mult}}$ respectively. The cone is defined in ϕ and η with an opening angle of 1.5 rad. Tracks from particles in the decay chain of interest are not counted in the cone variables. To avoid introducing a bias to one charge combination over another, the variables concerning the bachelor pions are combined. The variable smaller $\mathrm{min}_{\mathrm{PVs}}\ \chi^2_{\mathrm{IP}}$ takes the value from the pion with the smallest value for this parameter and larger $\mathrm{min}_{\mathrm{PVs}}\ \chi^2_{\mathrm{IP}}$ the larger of the two.

A full list of the inputs used to train the neural network is shown in Tab. 3.3. Similar to the initial selection, variables calculated after a D mass constraint are used when possible.

Particle	**Variables**
B^0	$^\dagger p_T$
	χ^2_{vertex}
	$^\dagger\chi^2_{\mathrm{flight\ w.r.t.\ best\ PV}}$
	$^\dagger \cos$ (Dir. angle w.r.t own PV)
	$^\dagger\mathrm{min}_{\mathrm{PVs}}\ \chi^2_{\mathrm{IP}}$
	$p_{T\,\mathrm{asym}}$ in 1.5 rad cone
	$\mathrm{track}_{\mathrm{mult}}$ in 1.5 rad cone
D^0	$^\dagger\chi^2_{\mathrm{vertex}}$
	$^\dagger\chi^2_{\mathrm{flight\ w.r.t.\ best\ PV}}$
	$^\dagger \cos$ (Dir. angle w.r.t own PV)
	$^\dagger\mathrm{min}_{\mathrm{PVs}}\ \chi^2_{\mathrm{IP}}$
D^0_K	$^\dagger\mathrm{min}_{\mathrm{PVs}}\ \chi^2_{\mathrm{IP}}$
D^0_π	$^\dagger\mathrm{min}_{\mathrm{PVs}}\ \chi^2_{\mathrm{IP}}$
π	†smaller $\mathrm{min}_{\mathrm{PVs}}\ \chi^2_{\mathrm{IP}}$
	†larger $\mathrm{min}_{\mathrm{PVs}}\ \chi^2_{\mathrm{IP}}$

Table 3.3: Variables used as inputs to the neural network selection. Parameters labelled † are calculated after a D mass constraint.

To separate signal candidates from background candidates in the training of the neural network, the `sWeights` technique was used. The formalism of `sWeights` and, more generally, `sPlots` is described in Ref [89]. The `sWeights` were calculated by the `Laura++` [90] package by fitting the $D\pi\pi$ mass distribution with a double Gaussian signal and a flat background distribution in the range 5200 to 5600 MeV/c^2. Please note that this is in no way a final fit to extract the signal yield, but it is just a simple fit to extract `sWeights` to train the neural network. The resulting `sWeights` take values from 1.3 (signal-like events) to -0.4 (background-like events) depending on the probability that the event was a signal or background event in the fit. The fit used to extract the `sWeights` and the mean `sWeight` as a function of B candidate mass is shown in Fig. 3.3.

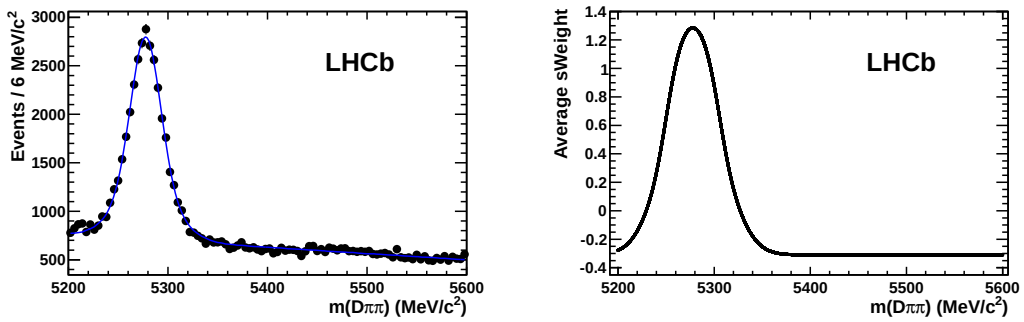

Figure 3.3: Result of the fit to the $D\pi\pi$ data sample, used to obtain `sWeights` as input to the neural network. (Left) result of the fit; (right) `sWeight` as a function of $m_{D\pi\pi}$.

Once trained successfully, the neural network returns a ranking of the input variables based upon their discriminating power, as shown in Tab. 3.3. The neural network output variable is shown in Fig. 3.4, with values ranging from -1 (background-like events) to about 0.6 (signal-like events). The signal and background yields as a function of the neural network output variable are also shown in Fig. 3.4.

The neural network output variable was then used to make a selection to purify the sample. Figure 3.5 shows how the requirement was optimised. The neural network was trained on $D\pi\pi$ data but was required to be optimised for the DKK mode. Comparison of the world average [5] $B^0 \to \bar{D}^0\pi^+\pi^-$ and $B^+ \to \bar{D}^0K^+\bar{K}^0$ branching fractions suggests the signal yield of the $B^0 \to \bar{D}^0K^+K^-$ mode is suppressed by a factor 2 with respect to $B^0 \to \bar{D}^0\pi^+\pi^-$:

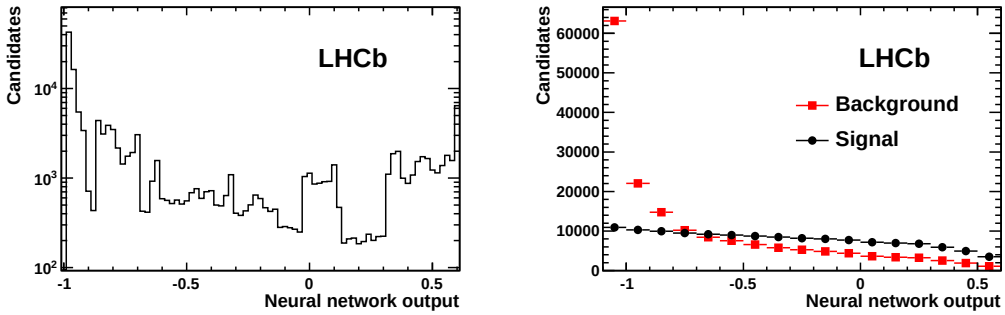

Figure 3.4: Result of the neural network training. (Left) output variable plotted for all events; (right) yields of signal and background obtained by a fit to $m_{D\pi\pi}$ with different requirements on the neural network output.

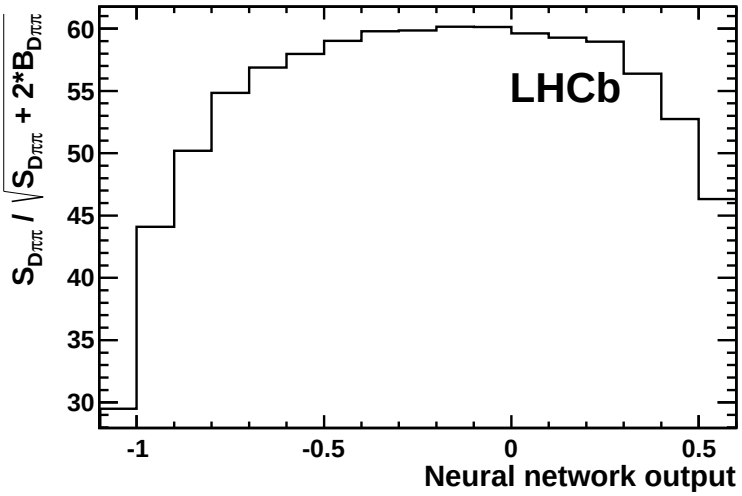

Figure 3.5: Optimisation of the requirement on the neural network output variable. S_{Dhh} and B_{Dhh} are the number of $D\pi\pi$ signal and background candidates respectively. Note that the y-axis scale is not absolutely normalised.

$$\mathcal{B}(B^0 \to \bar{D}^0\pi^+\pi^-) = (8.4 \pm 0.9) \times 10^{-4}, \tag{3.3}$$
$$\mathcal{B}(B^+ \to \bar{D}^0 K^+ \bar{K}^0) = (5.5 \pm 1.6) \times 10^{-4}.$$

In addition to this factor 2, the $B^0 \to \bar{D}^0 K^+ K^-$ decay mode is colour suppressed with respect to the B^+ mode above giving a further suppression by a factor of roughly 10. Combining these factors, the signal yield in the DKK final state is expected to be suppressed by a factor 20 when compared with the $D\pi\pi$ mode.

Secondly, the kaon identification requirements are effective to reduce combi-

natorial backgrounds, giving an estimated factor 10 less combinatorial background in $B^0 \to \bar{D}^0 K^+ K^-$. Therefore, $S_{DKK}/\sqrt{S_{DKK} + B_{DKK}} \propto S_{D\pi\pi}/\sqrt{S_{D\pi\pi} + 2B_{D\pi\pi}}$ is plotted as a function of the requirement on the neural network output variable. The constant of proportionality is neglected since only the peak position is required, not its value. S_{Dhh} and B_{Dhh} are the numbers of signal and background candidates of the decay mode respectively. Figure 3.5 shows that the curve peaks near -0.3, so that value was used.

3.5.3 Particle identification

The bachelor kaon identification requirement is very effective at reducing the combinatorial background in the DKK data sample. Tighter and looser requirements were investigated to check that the $\mathrm{DLL}_{K\pi} > 5$ requirement was reasonable. Three plots in Fig. 3.6 show the results of using $\mathrm{DLL}_{K\pi} > 3$, $\mathrm{DLL}_{K\pi} > 5$ and $\mathrm{DLL}_{K\pi} > 7$. The signal to background ratio appears similar in each of the three plots. Therefore the nominal requirement remained at $\mathrm{DLL}_{K\pi} > 5$. Given that this is not a blinded analysis, no further optimisation of the particle identification requirements are performed in order to reduce the chance of biasing the measurement.

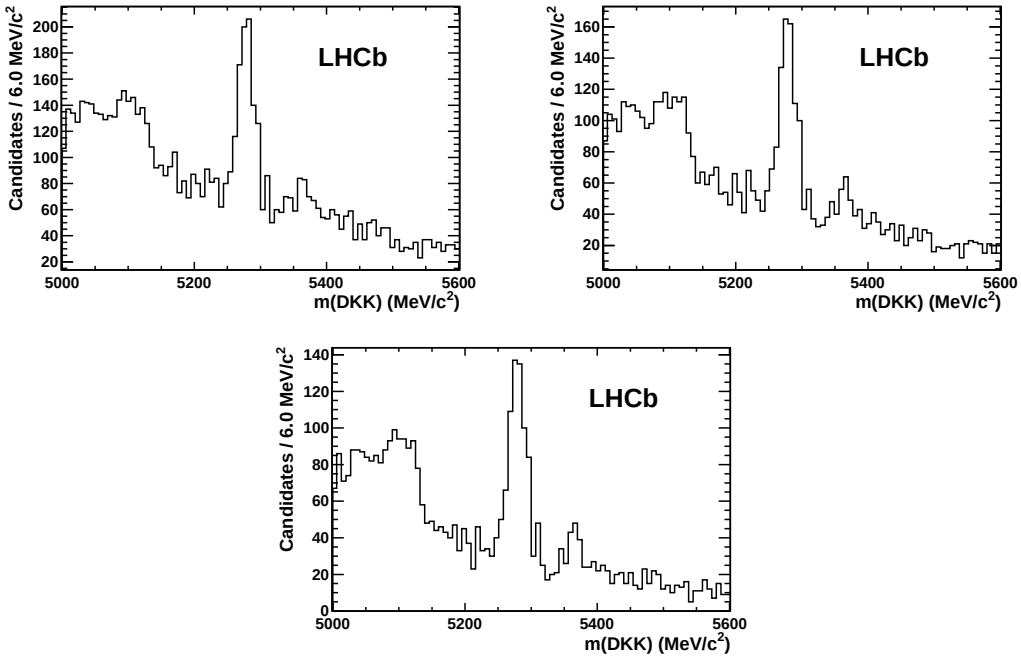

Figure 3.6: Effect of bachelor particle identification requirement on the B candidate mass distribution in the DKK data sample, for (left) $\mathrm{DLL}_{K\pi} > 3$; (right) $\mathrm{DLL}_{K\pi} > 5$ (default); (bottom) $\mathrm{DLL}_{K\pi} > 7$.

Further particle identification requirements on both muons and protons have been considered, however neither is used in the analysis. The effect of a muon veto is shown in Fig. 3.7 for both $D\pi\pi$ and DKK. The veto is applied if at least one of the bachelor tracks has hits in the muon stations associated to it. A peak is visible in the $D\pi\pi$ plot but this is most probably due to $\pi \to \mu$ misidentification or decays in flight. A muon veto is not applied because the number of events containing a real muon appears to be small.

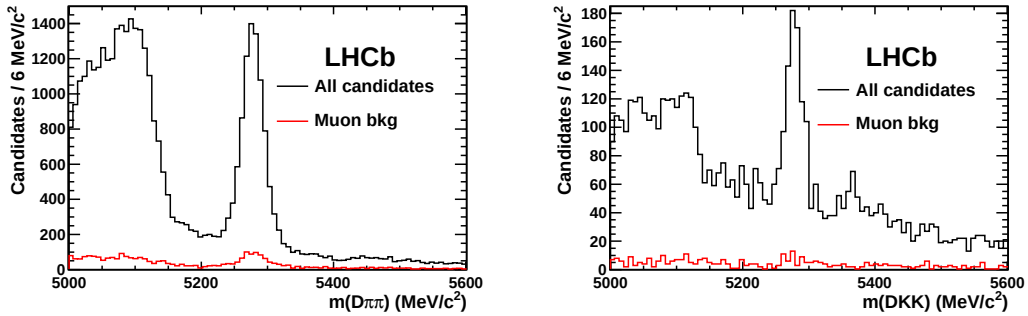

Figure 3.7: Events passing the full selection (black) and those failing a muon veto (red) for (left) $D\pi\pi$ and (right) DKK.

Two possible proton vetoes were investigated and are shown in Fig. 3.8. The tight (loose) requirement is defined by $\mathrm{DLL}_{p\pi} > 0(5)$ for the $D\pi\pi$ mode and $(\mathrm{DLL}_{p\pi} - \mathrm{DLL}_{K\pi}) > 0(5)$ for DKK. The vetoes are defined differently between modes because PID at LHCb is measured relative to the pion hypothesis. A signal peak is observed in all of the distributions but no other structures are seen. A small excess in the high mass region of the $D\pi\pi$ plot suggests a small background from a source such as $\Lambda_b^0 \to Dp\pi^-$, that could be included in a fit model. Therefore, no proton veto is applied.

3.5.4 $D^{*-}(2010)$ veto

The decay $B^0 \to D^{*-}(2010)\pi^+$ where $D^{*-}(2010) \to \bar{D}^0\pi^-$ produces a large contribution to the final state $B^0 \to \bar{D}^0\pi^+\pi^-$. The corresponding branching fractions are

$$\begin{aligned} \mathcal{B}\left(B^0 \to D^{*-}(2010)\pi^+\right) &= (2.76 \pm 0.13) \times 10^{-3}\,, \\ \mathcal{B}\left(D^{*-}(2010) \to \bar{D}^0\pi^-\right) &= (67.7 \pm 0.5) \times 10^{-2}\,. \end{aligned} \tag{3.4}$$

Importantly, this contribution is not included in the measurement of $B^0 \to$

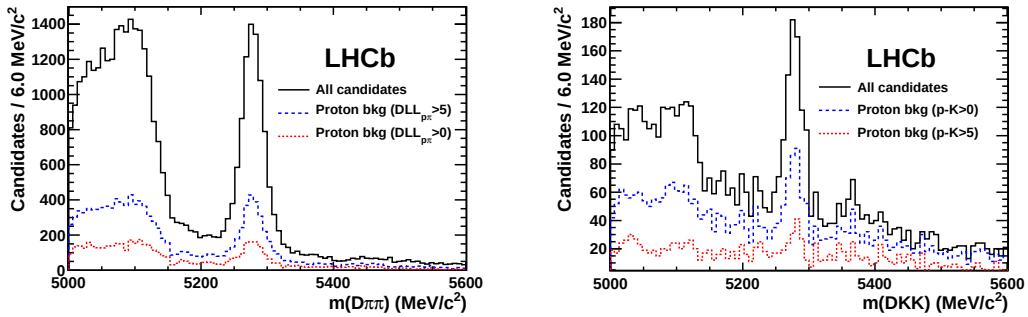

Figure 3.8: Events passing the full selection (black) and those failing a proton veto for (left) $D\pi\pi$ and (right) DKK. A (blue) tight veto and a (red) looser veto are shown.

$\bar{D}^0\pi^+\pi^-$ [5] since it is larger than the rest of the Dalitz plot contributions added together. In a previous analysis by Belle [51] of the same final state the $D^{*-}(2010)$ was vetoed by removing events with $m_{D\pi} - m_D$ within 2.5 MeV/c^2 of the nominal D^{*-}–$\bar{D}^0$ mass difference.

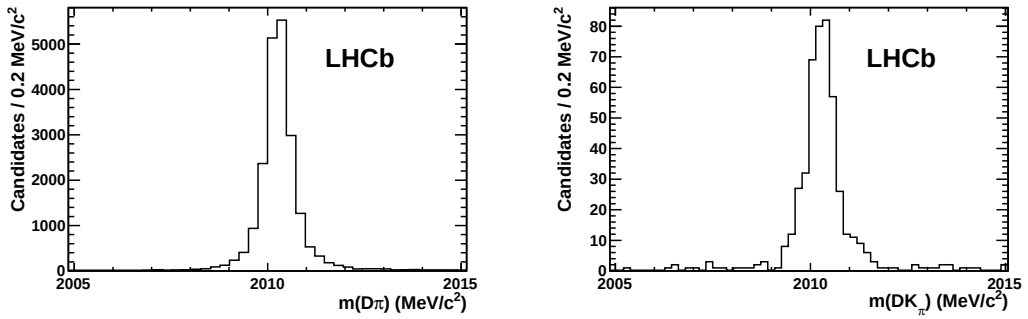

Figure 3.9: (Left) Invariant mass of $D\pi$ pair for $D\pi\pi$ sample candidates in the B^0 signal mass window . (Right) Invariant mass of $D\pi$ pair for DKK sample candidates in the B^0 signal mass window (recalculated with the pion mass hypothesis). Note that only one Dh combination appears in the plots per event.

A zoomed view of the $m(D\pi)$ distribution for events in the Dhh signal region is shown in Fig. 3.9. A sharp D^* peak is observed with narrow resolution, comfortably inside the proposed requirement of ± 2.5 MeV/c^2 of the nominal D^{*-}–$\bar{D}^0$ mass difference. Therefore, the same requirement will be used in this analysis.

Given the high rate of D^* production, both from B decays and prompt production, there may be a potentially serious background contribution to $B^0 \to \bar{D}^0 K^+ K^-$ from this source, together with $\pi \to K$ misidentification. To check this the invariant mass, $m(DK_\pi)$, was calculated, where K_π is the appropriate kaon

under a pion mass hypothesis. $m(DK_\pi)$ is shown for DKK in Fig. 3.9 (right) where a clear peak corresponding to the D^{*-} can be seen with similar resolution to the $D\pi\pi$ mode. Therefore, the veto is also applied to the $B^0 \to \bar{D}^0 K^+ K^-$ data sample.

3.5.5 D_s^+ veto

One of the many possible peaking backgrounds found in Sec. 4.3 for the DKK final state is from B^0 and B_s^0 decays to $D_s^\pm K^\mp$ with $D_s^\pm \to K^+K^-\pi^\pm$. To effectively eliminate this small background, all candidates where the invariant mass of the pair of bachelor kaon tracks together with the pion from the $\bar{D}^0$ decay, $m(KK\pi)$, is consistent with that of the D_s^+ are vetoed.

The distribution of events passing the initial DKK selection from the $B_s^0 \to D_s^\mp K^\pm$ MC sample is shown in Fig. 3.10. From there the D_s^+ veto is chosen to be 1950–1975 MeV/c^2. This veto removes 0.9% of total candidates, of which only 3 events are in the signal region. Note that this veto is not applied to the $D\pi\pi$ sample.

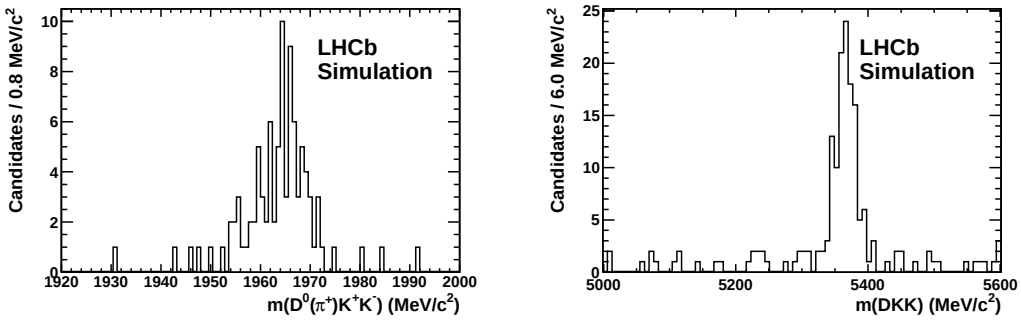

Figure 3.10: (Left) invariant mass of the pair of bachelor kaon tracks and the pion from the $\bar{D}^0$ decay for $B^0 \to \bar{D}^0 K^+ K^-$ events following the application of the initial selection to a $B_s^0 \to D_s^\mp K^\pm$ simulated sample; (right) B candidate invariant mass for the same events, note that this is identical to Fig. 4.10(right)).

3.6 Efficiency

In order to study the efficiency of the two decay modes the total efficiency is split into four contributions for each mode: geometrical, selection, particle identification and trigger effects. The total efficiency for each mode is then calculated as

$$\epsilon^{\text{tot}} = \epsilon^{\text{geom}}\, \epsilon^{\text{sel|geom}}\, \epsilon^{\text{PID|sel\&geom}}\, \epsilon^{\text{trig|PID\&sel\&geom}}, \tag{3.5}$$

where the terms are, from left to right, geometrical, selection, particle identification and trigger efficiencies. In this context, geometrical efficiency is the efficiency of the decay occurring inside the LHCb detector acceptance. The order of the superscript labels X|Y means that X is the efficiency relative to the effect from Y. Since the aim of the analysis is to measure the ratio of branching fractions, it is the ratio of efficiencies that is important, rather than absolute values. The majority of the systematic effects cancel in the ratio between $\bar{D}^0 K^+ K^-$ and $\bar{D}^0 \pi^+ \pi^-$, providing a significant reduction of systematic uncertainties. The greatest exception from this cancellation is the PID efficiency, which is completely different for the bachelor tracks in each decay. A summary of the various efficiencies for both $D\pi\pi$ and DKK decay modes is shown in Tab. 3.4. The different contributions to the total efficiency shown in Eq. 3.5 are described below.

Efficiency	$D\pi\pi$	DKK
ϵ^{geom}	45.1 %	48.5 %
$\epsilon^{\text{sel\|geom}}$	2.28 %	2.09 %
$\epsilon^{\text{PID\|sel\&geom}}$	79.5 %	71.0 %
$\epsilon^{\text{trig\|PID\&sel\&geom}}$	94.1 %	93.4 %
ϵ^{tot}	0.78 %	0.68 %

Table 3.4: Summary of the efficiencies found for $D\pi\pi$ and DKK in phase space simulation samples. Fractional uncertainties are of order 1 %.

3.6.1 Geometrical efficiency

The geometrical efficiency, ϵ^{geom}, was determined using simulated data samples without any detector acceptance requirements applied to the daughter particles. The simulated data was generated using a phase space model, such that candidates are uniformally distributed over the Dalitz plot. The samples do, however, require that the B meson is inside the detector acceptance. The variation of ϵ^{geom} is shown as a function of Dalitz plot position in Fig 3.11 for both DKK and $D\pi\pi$ decay modes. For both DKK and $D\pi\pi$ the distribution of ϵ^{geom} appears fairly flat across the Dalitz plot, with some local variations of order 10 %. Note that the Dalitz plot is defined using quantities from the B and D mass constrained kinematic fit. The integrated geometrical efficiency across the Dalitz plot is 45.1 % for $D\pi\pi$ and 48.5 % for DKK. The difference between these numbers is due to the pion mass being lower than the kaon mass. In the $D\pi\pi$ sample, the bachelors have slightly higher momenta than in the DKK sample, this makes them more likely to escape the

detector acceptance.

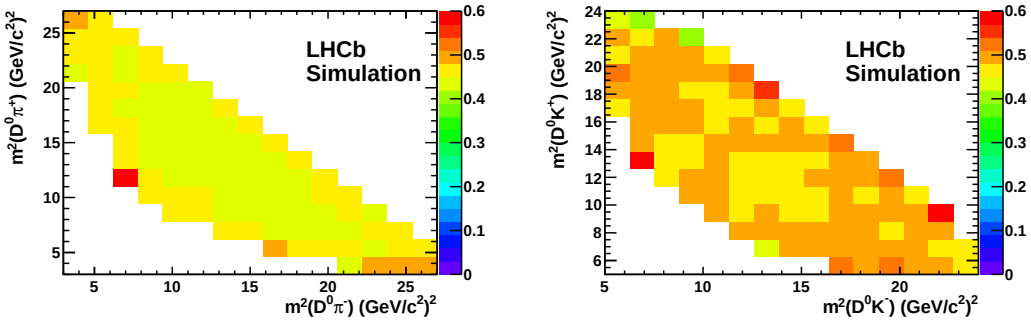

Figure 3.11: Geometrical efficiency, ϵ^{geom}, across the $B \to Dhh$ Dalitz plots, obtained from simulations. (Left) $\bar{D}^0\pi^+\pi^-$, (right) $\bar{D}^0K^+K^-$. Note that the z-axis scales are set to be the same in both plots.

3.6.2 Selection efficiency

The selection efficiency, $\epsilon^{\text{sel|geom}}$, was calculated using simulated data samples with detector acceptance requirements applied to each particle. The variations of $\epsilon^{\text{sel|geom}}$ across $D\pi\pi$ and DKK Dalitz plots are shown in Fig 3.12. A slight drop in the selection efficiency is seen in the corners of the $D\pi\pi$ Dalitz plot and also, less clearly, for DKK. Note that the Dalitz plot is defined using quantities from the B and D mass constrained kinematic fit. The integrated selection efficiency across the Dalitz plot is 2.28 % for $D\pi\pi$ and 2.09 % for DKK.

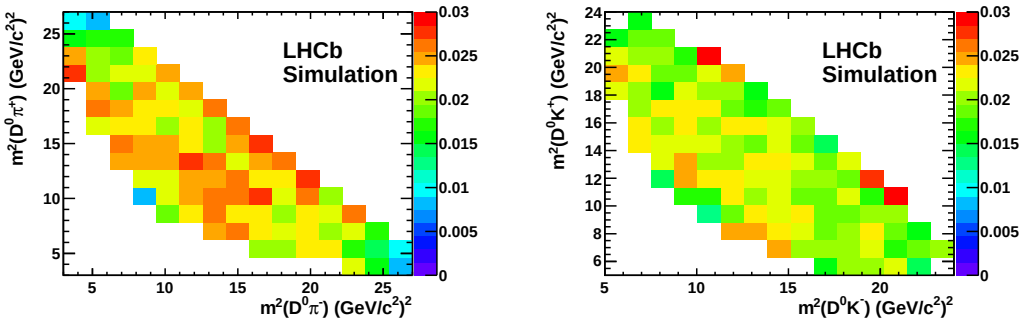

Figure 3.12: Selection efficiency, $\epsilon^{\text{sel|geom}}$, across the $B \to Dhh$ Dalitz plots, obtained from simulations. (Left) $\bar{D}^0\pi^+\pi^-$, (right) $\bar{D}^0K^+K^-$. Note that the z-axis scales are set to be the same in both plots.

3.6.3 Particle identification efficiency

The particle identification efficiency, $\epsilon^{\text{PID|sel\&geom}}$, was determined using a calibration data sample of kaons and pions. These kaons and pions are identified without using direct particle identification, but inferring it from the rest of the decay chain. The calibration sample is used by the `PIDCalib` tool to create a map of $\epsilon^{\text{PID|sel\&geom}}$ in bins of p and p_T for kaons and pions at a given particle identification cut. Then simulated data samples were used to calculate $\epsilon^{\text{PID|sel\&geom}}$ as a function of the Dalitz plot variables by multiplying the efficiencies of the two bachelor tracks together. The efficiency of each track was obtained using the p and p_T efficiency map calculated from the calibration sample. The variation of $\epsilon^{\text{PID|sel\&geom}}$ across the Dalitz plot is shown for both $D\pi\pi$ and DKK in Fig. 3.13. A small drop in particle identification efficiency is observed in the corners of the $D\pi\pi$ Dalitz plot and also in DKK, although it is not as clear. Note that the Dalitz plot is defined using quantities from the B and D mass constrained kinematic fit. The integrated particle identification efficiency across the Dalitz plot is 79.5 % for $D\pi\pi$ and 71.0 % for DKK.

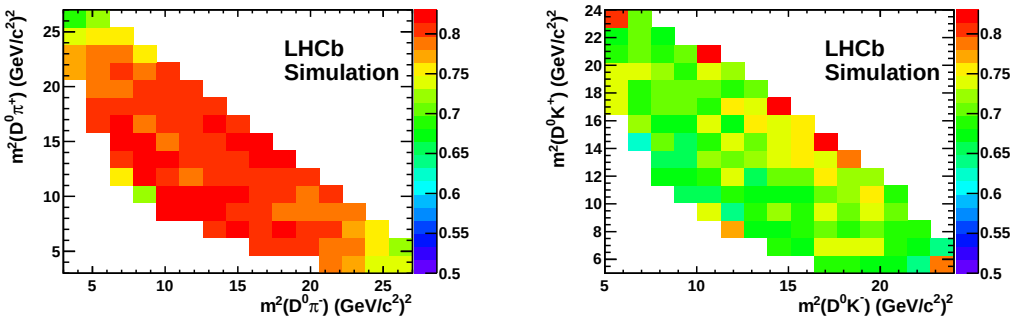

Figure 3.13: Particle identification efficiency, $\epsilon^{\text{PID|sel\&geom}}$, across the $B \to Dhh$ Dalitz plots, obtained from calibration data and simulation. (Left) $\bar{D}^0\pi^+\pi^-$, (right) $\bar{D}^0K^+K^-$. Note that the z-axis scales are set to be the same in both plots.

3.6.4 Trigger efficiency

The trigger efficiency, $\epsilon^{\text{trig|PID\&sel\&geom}}$, was calculated using simulated data samples with the full selection criteria applied with the exception of the trigger requirements. The variation of $\epsilon^{\text{trig|PID\&sel\&geom}}$ as a function of the Dalitz plot variables is shown in Fig. 3.14 for both $D\pi\pi$ and DKK. The distributions of $\epsilon^{\text{trig|PID\&sel\&geom}}$ are fairly flat across the Dalitz plot for both $D\pi\pi$ and DKK decay modes. Note that the Dalitz plot is defined using quantities from the B and D mass constrained kinematic

fit. The integrated trigger efficiency across the Dalitz plot is 94.1 % for $D\pi\pi$ and 93.4 % for DKK.

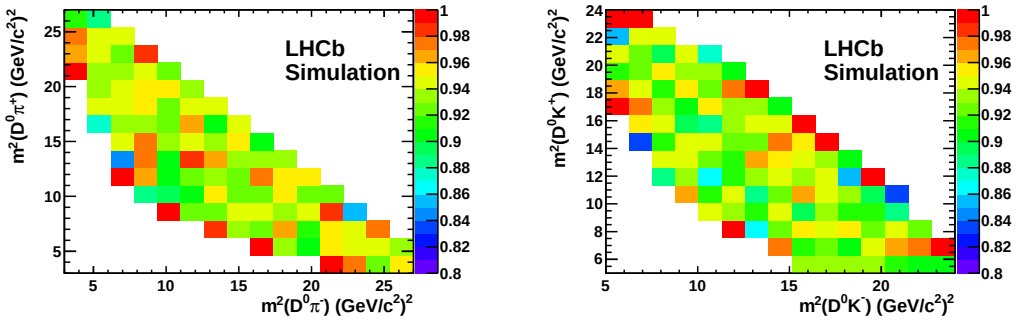

Figure 3.14: Trigger efficiency, $\epsilon^{\text{trig|PID\&sel\&geom}}$, across the $B \to Dhh$ Dalitz plots, obtained from simulations. (Left) $\bar{D}^0\pi^+\pi^-$, (right) $\bar{D}^0K^+K^-$. Note that the z-axis scales are set to be the same in both plots.

3.7 Events failing mass constrained fit

As discussed in Sec. 3.4, a B and D mass constraint is applied during the vertex fit. Some background events fail such a procedure because there is no way to fit the tracks with such constraints applied. These events are shown for $D\pi\pi$ and DKK in Fig. 3.1 and it is clear that none of the vetoed events is in the signal region. This veto removes 0.6 % of $D\pi\pi$ events and 2.8 % of DKK events.

3.8 Yields

38503 $D\pi\pi$ candidates are seen after all of the selection requirements described have been applied. Of these, 7323 are in the B^0 mass window of 5250 MeV/c^2 $< m_{D\pi\pi} <$ 5300 MeV/c^2. The numbers for the DKK mode are 5449 and 896 respectively. The B candidate mass distributions are shown for each decay mode in Fig. 3.15.

Multiple candidates are found in the selected events, where two B candidates have the same event number and run number. They occur in 1.1 % of $D\pi\pi$ events and in 0.7 % of events in the signal window. The corresponding numbers for the DKK mode are 0.6 % and 0.6 %. These candidates are kept and are treated no differently to the other candidates.

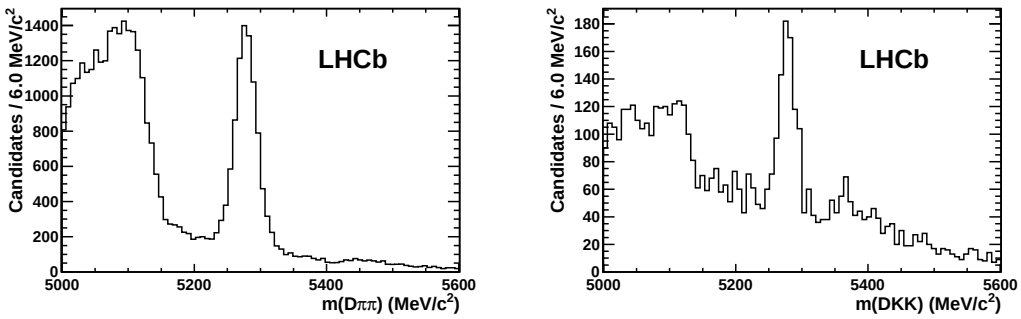

Figure 3.15: Invariant mass distribution of events after all selection requirements for (left) $D\pi\pi$ and (right) DKK.

Chapter 4

Background studies

This chapter presents the range of background studies undertaken as part of this analysis. Firstly the types of backgrounds involved are introduced in Sec. 4.1, and then these are discussed in greater detail for the DKK mode in Secs. 4.2, 4.3 and 4.4. Some of the studies are repeated for the $D\pi\pi$ mode in Sec. 4.5.

4.1 Background categories

To characterise backgrounds, the D mass requirement, see Tab. 3.2, was removed in order to show how many of the background events originate from candidates containing a real D meson. The plots from this study are shown in Fig. 4.1, and when compared to those in Fig. 3.15 it is clear that the background level is lower in the D mass plot. This implies that the majority of background events include a real D meson coupled with two random tracks. A second observation is that the D sidebands appear flat, and they have no structure which allows them to be used to study charmless backgrounds. There are no obvious structures from misidentification of $D \to KK$ or $D \to \pi\pi$ modes or from missing the soft π^0 from $D \to K\pi\pi^0$.

In this analysis three different types of background are considered and are studied in detail.

- *Partially reconstructed B decays*, where events include a D^0 meson and two tracks originating from a single B candidate, but additional particles in the decay were missed, as described in Sec. 4.2. Note that the D^0 may be a random combination of two tracks passing the selection criteria, known as a fake D^0.
- *Peaking background*, where all four final state particles come from a B candidate, but either the decay is not via a D^0 meson or the particles are in-

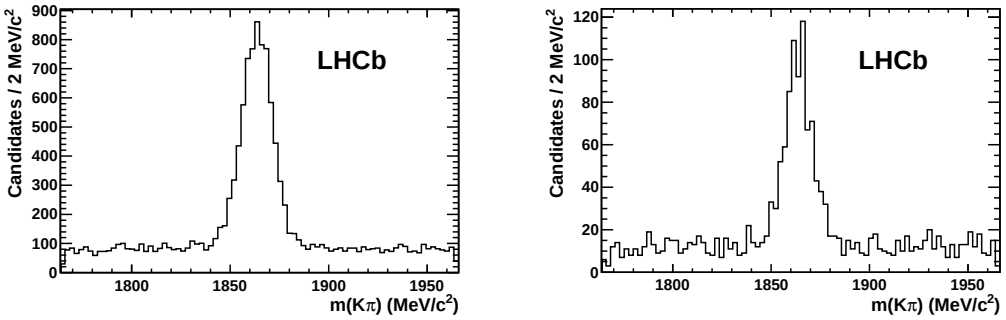

Figure 4.1: D candidate invariant mass distributions for events in the B mass signal region for (left) $D\pi\pi$ and (right) DKK.

correctly identified. These are referred to as *charmless* and *charmed* peaking background respectively and are described in Sec. 4.3.1 and Sec. 4.3.2.

- *Combinatorial background*, which consists of events with a real or fake D^0 meson and some random tracks. More information is availiable in Sec. 4.4.

Additionally, a contribution from $B_s^0 \to \bar{D}^0 K^+ K^-$ is expected and can be accounted for as a separate contribution in the fit to the DKK mass distribution.

4.2 Partially reconstructed B decays

The partially reconstructed B decays occupy the low mass region of the B candidate mass distribution, approximately below 5200 MeV/c^2. Due to the signal-like nature of the partially reconstructed B decays, they are not rejected by the neural network. In fact, the neural network was not trained on any partially reconstructed B decays, as discussed in Sec. 3.5.2. Examples of such backgrounds for the $B^0 \to \bar{D}^0 K^+ K^-$ mode are $B^0 \to \bar{D}^{*0} K^+ K^-$ with $\bar{D}^{*0} \to \bar{D}^0 \pi^0$ or $\bar{D}^0 \gamma$ where the soft neutral $\bar{D}^{*0}$ daughter is not reconstructed.

Careful choice of the lower limit of the mass window used in the fit to the B candidate mass distribution allows partially reconstructed B decays to be considered without detailed knowledge of the shapes. This approach has been used in previous LHCb analyses, for example see Ref. [56]. For example, see Fig. 3.15 (left) where the complex shape of the partially reconstructed background can been seen in the region from below 5200 MeV/c^2. The full shape of this background is not important, only the tail of the distribution affects the B^0 signal region. By choosing a mass

range to include only this tail, details of the full partially reconstructed background shape are not required. Therefore, the lower boundary of the B mass fit is set to 5150 MeV/c^2, allowing a simple shape such as an exponential to be used.

$B_s^0 \to \bar{D}^{*0} K^+ K^-$ could present a dangerous background underneath the B^0 mass peak if the neutral daughter from the D^{*0} decay is missed. These decay modes are discussed further as peaking backgrounds in Sec. 4.3.2. Since there is no evidence for a large $B_s^0 \to \bar{D}^0 K^+ K^-$ signal in the DKK data sample, it is assumed the rate of $B_s^0 \to \bar{D}^{*0} K^+ K^-$ is similarly small. Therefore, it is not considered in the fit to the $B^0 \to \bar{D}^0 K^+ K^-$ data sample but is instead treated as a source of systematic uncertainty.

4.3 Peaking background

Peaking backgrounds can be considered in two groups, charmed and charmless. The large signal in $B^0 \to \bar{D}^0 K^+ K^-$ was a surprise initially, so many searches for peaking backgrounds were performed to understand if the observed peak really was a signal decay. All of the studies discussed here use simulated data with trigger, stripping and initial selection applied. The requirement on the neural network output variable was not applied to preserve statistics and the two charm vetoes were not required either.

4.3.1 Charmless peaking background

As mentioned previously, the lack of structure in the D sidebands allows them to be used to study charmless background contributions. The D sidebands are defined as follows: lower mass sideband as $1764 \leq m_D \leq 1828$ MeV/c^2 and the upper mass sideband as $1900 \leq m_D \leq 1964$ MeV/c^2. The method used to estimate the charmless backgrounds was to take events from the D sidebands and scale the yield of this contribution to the region underneath the D mass peak. The scaling was done by fitting the D sidebands with a straight line and extrapolating the background yield into the D signal peak region. The result of this study is shown for both sidebands combined in Fig. 4.2 and independently for upper and lower mass sidebands in Fig. 4.3. Note that Fig. 4.3 shows the data from each sideband scaled to be twice as large to represent the full charmless background originating from a single sideband. Since a peak is visible at the B^0 mass in the charmless background, the number of events in the peak must be extracted. The number of peaking charmless events was found by fitting the invariant B mass distribution of events from the D sidebands, as shown in Fig. 4.4. The fit used was a double Gaussian for the peaking events

and a linear function for the background events. The total number of charmless background events forming a peaking background was 403 ± 57 events, which scales to an expected 126 ± 18 events underneath the D mass peak. Note that there is no evidence of charmless peaking background under the B_s^0 peak.

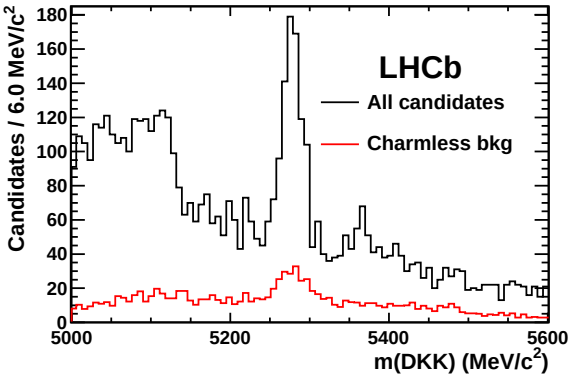

Figure 4.2: Expected pollution from charmless background events underneath the D^0 mass peak (red line), estimated from events failing the D^0 mass cut. For comparison it is overlaid on the DKK B candidate mass distribution from events passing the D^0 mass cut.

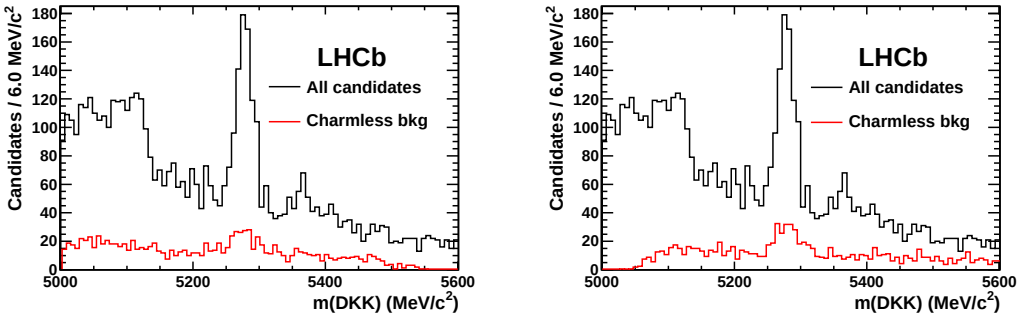

Figure 4.3: As Fig. 4.2 but for (left) lower and (right) upper D candidate mass sidebands separately. All charmless background events are assumed to come from a single sideband in this figure and so are shown twice as large w.r.t. Fig.4.2.

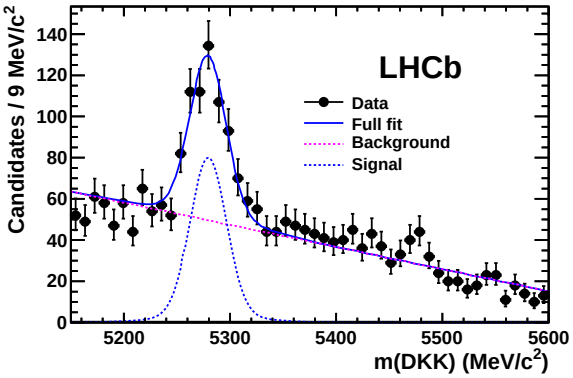

Figure 4.4: Fit to the B candidate invariant mass distribution of events from the D^0 sidebands in the DKK data sample. Shown are the data points (black), full fit function (solid blue), double Gaussian signal (dashed blue) and background (dashed pink).

4.3.2 Charmed peaking background

The first check for charmed peaking backgrounds was to use generic simulated samples to understand which types of decays may contribute. The generic samples generated B^0, B^+, B_s^0 and Λ_b hadrons and decayed them to all possible final states including a charm meson. The B invariant mass distributions of events surviving the DKK initial selection from these studies are shown in Fig. 4.5.

The generic simulated studies suggest that no significant sources of peaking backgrounds exist in any of the samples. Of order 100 events pass the selection for all modes, with Λ_b being the largest contribution. Further studies of Λ_b simulated samples were performed based on the fact that the Λ_b generic sample had the most candidates passing the selection. The modes used were $\Lambda_b \to D^0 p K^-$ and $\Lambda_b \to D^0 p \pi^-$. Events passing the selection from these modes are shown in Fig. 4.6. The plots show that of order 10000 and 100 $\Lambda_b \to D^0 p K^-$ and $\Lambda_b \to D^0 p \pi^-$ events passed the selection from half a million events respectively. However, neither shows a significant peaking background contribution in the B^0 signal region. Due to the high number of $\Lambda_b \to D^0 p K^-$ events surviving the selection at B mass values this component will be included in the fit to the DKK data.

$B \to D^* X$ decays are also considered, as mentioned in Sec.4.2. The simulated samples studied are:

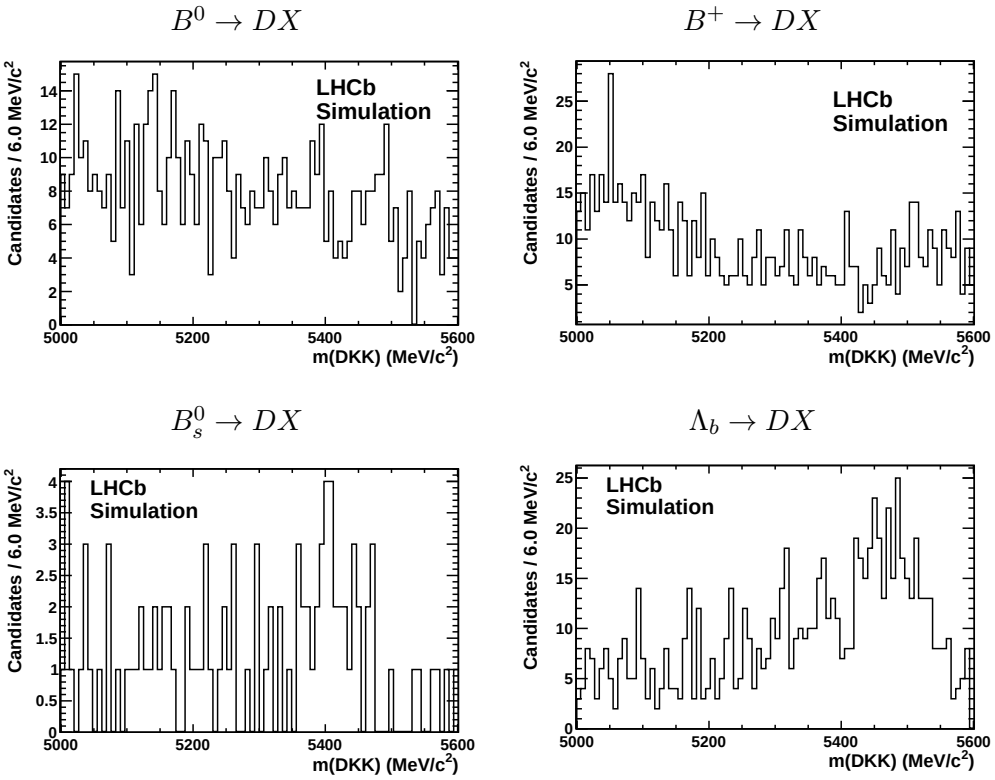

Figure 4.5: Events passing the $B^0 \to \bar{D}^0 K^+ K^-$ initial selection from generic simulated samples. From the top left, going clockwise, they are: $B^0 \to DX$, $B^+ \to DX$, $\Lambda_b \to DX$ and $B^0_s \to DX$.

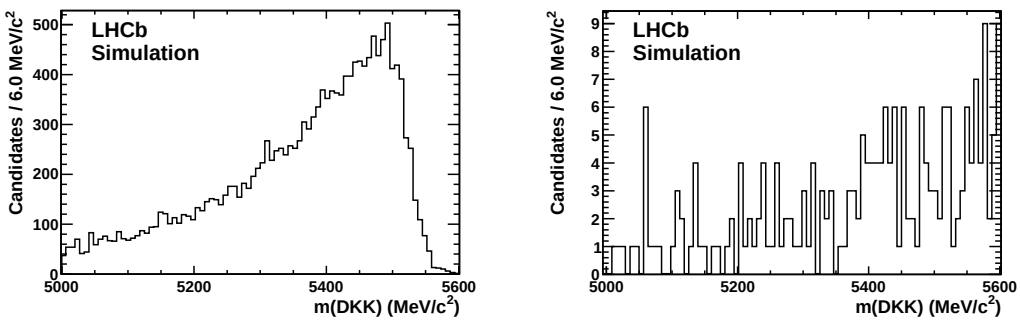

Figure 4.6: Events passing the $B^0 \to \bar{D}^0 K^+ K^-$ initial selection from two Λ_b signal decay modes, (left) $\Lambda_b \to D^0 p K^-$ and (right) $\Lambda_b \to D^0 p \pi^-$.

- $B^0 \to \bar{D}^{*0} K^{*0}$ with $\bar{D}^0 \to \bar{D}^0 \gamma$;
- $B^0 \to \bar{D}^{*0} K^{*0}$ with $\bar{D}^0 \to \bar{D}^0 \pi^0$;
- $B^0_s \to \bar{D}^{*0} \bar{K}^{*0}$ with $\bar{D}^0 \to \bar{D}^0 \gamma$;
- $B^0_s \to \bar{D}^{*0} \bar{K}^{*0}$ with $\bar{D}^0 \to \bar{D}^0 \pi^0$.

In particular the partial reconstruction of the B^0_s modes could be a peaking background in the signal region. The B invariant mass distributions of candidates from these four samples are shown in Fig. 4.7. The distributions are relatively flat, or at least linear, over the range of B masses between 5150 and 5600 MeV/c^2, with the exception of the $B^0_s \to \bar{D}^{*0} \bar{K}^{*0}$ with $\bar{D}^0 \to \bar{D}^0 \pi^0$ decay mode, which is considered separately as a source of systematic uncertainty in Sec. 7. The remaining three decay modes are not treated separately as peaking backgrounds and are absorbed into the combinatorial background shape.

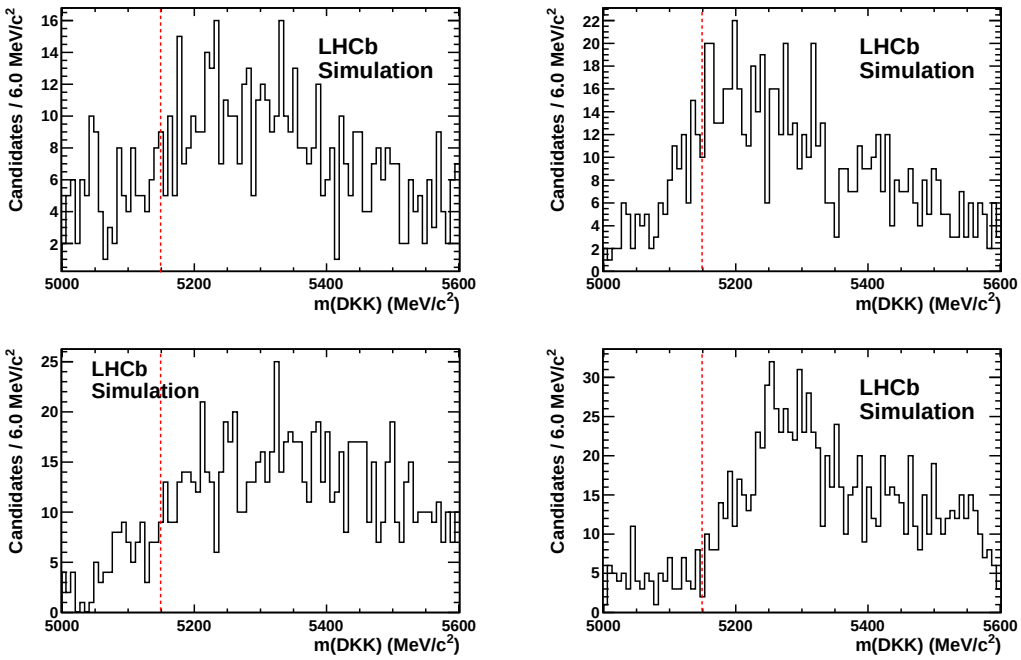

Figure 4.7: Invariant mass distributions of simulated events passing the $B^0 \to \bar{D}^0 K^+ K^-$ initial selection from $B \to \bar{D}^{*0} K^{*0}$ modes: (top left) B^0 with $\bar{D}^{*0} \to \bar{D}^0 \gamma$, (top right) B^0 with $\bar{D}^{*0} \to \bar{D}^0 \pi^0$, (bottom left) B^0_s with $\bar{D}^{*0} \to \bar{D}^0 \gamma$, (bottom right) B^0_s with $\bar{D}^{*0} \to \bar{D}^0 \pi^0$. The dashed red lines show the lower boundary of the fit range, 5150 MeV/c^2.

Cross-feeds from other $B \to Dhh$ modes could also create peaking backgrounds either under or close to the signal mass peak. To investigate this, the DKK selection was applied to $B^0 \to \bar{D}^0\pi^+\pi^-$, $B^0 \to \bar{D}^0K^+\pi^-$ and $B_s^0 \to \bar{D}^0K^+\pi^-$ simulated samples. The results are shown in Fig. 4.8 where $\mathcal{O}(10)$ candidates survive the selection for the $D\pi\pi$ mode from a sample of 500000 and $\mathcal{O}(100)$ from a sample of 400000 for the $DK\pi$ modes. There are no peaks in the signal region from any of these decay modes, and $D\pi\pi$ can be neglected completely. The $DK\pi$ modes, however, have to be included in the fit for $B^0 \to \bar{D}^0K^+K^-$ due to the number of events passing at higher B mass values.

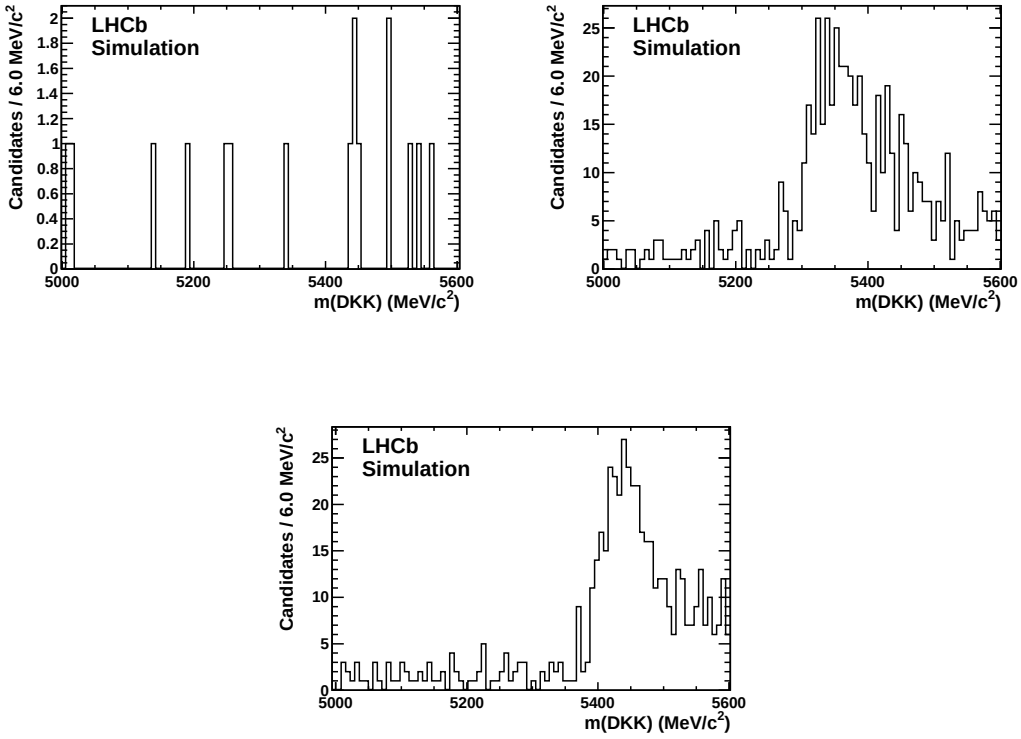

Figure 4.8: Invariant mass distribution of simulated events passing the $B^0 \to \bar{D}^0K^+K^-$ initial selection from (left) $B^0 \to \bar{D}^0\pi^+\pi^-$, (right) $B^0 \to \bar{D}^0K^+\pi^-$ and (bottom) $B_s^0 \to \bar{D}^0K^+\pi^-$.

To search for further peaking backgrounds from B hadron decays with charm mesons, particle combinations from the $B^0 \to (\bar{D}^0 \to K^+\pi^-)K^+K^-$ final state were examined. The particle combinations considered in the data sample were:

- Bachelor K^+ and K from D meson;

- Bachelor K^- and π from D meson;
- Both bachelors and K from D meson;
- Both bachelors and π from D meson.

The invariant mass distributions of the above particle combinations from the final DKK data sample are shown in Fig.4.9. From there it is clear that the only structure that needs to be considered further is a small peak in $m(KK\pi)$, corresponding to the D_s^+ meson.

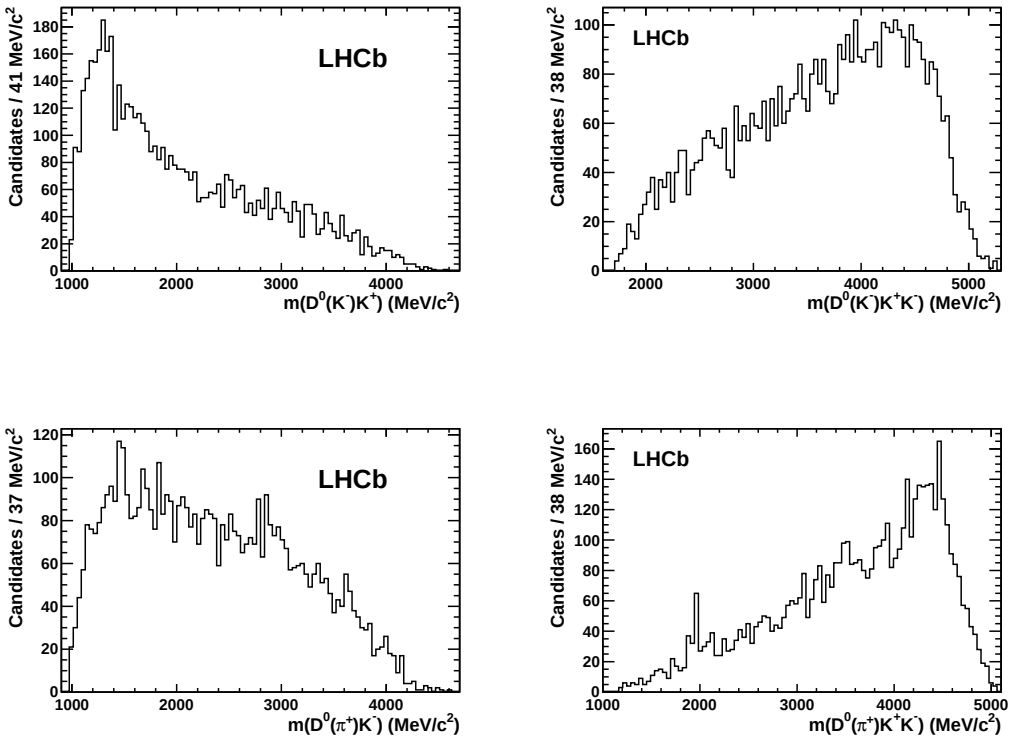

Figure 4.9: Invariant mass distributions of combinations of particles in the $B^0 \to \bar{D}^0 K^+ K^-$ data sample: (top left) K from D meson with bachelor K^+, (top right) K from D meson with both bachelors, (bottom left) π from D meson with bachelor K^- and (bottom right) π from D meson with both bachelors. $D^0(h)$ means the daughter h from the D^0 decay.

Following the observation of the D_s^+ peak in the $m(KK\pi)$ mass distribution, Fig. 4.9, additional potential sources of peaking background are B^0 and $B_s^0 \to D_s^\mp K^\pm$ with $D_s^\mp \to K^+K^-\pi^\mp$. Simulated events for these decays were passed

through the DKK selection algorithm, with the results shown in Fig. 4.10. An obvious peak is seen around the B_s^0 mass for the $B_s^0 \to D_s^{\mp} K^{\pm}$ sample. There are 170 events that survive the selection from a sample of 500000 events in the B_s^0 decay mode and 2 from 200000 for the B^0 decay mode. The large difference between the numbers of surviving events from the two decay modes is believed to be due to the different D decay models in the MC samples. The B_s^0 mode uses a phase space model, `PHSP`, while the B^0 mode uses a more realistic Dalitz plot model, `D_DALITZ`, in `EvtGen`. The phase space model used is not ideal for this decay mode, however given the small size of the D_s^+ peak in Fig. 4.9 further studies are not required. Although this background is not considered to be a serious concern, a D_s^+ veto is applied to the DKK data sample, as described in Sec. 3.5.5, to make sure that it is reduced to a negligible level.

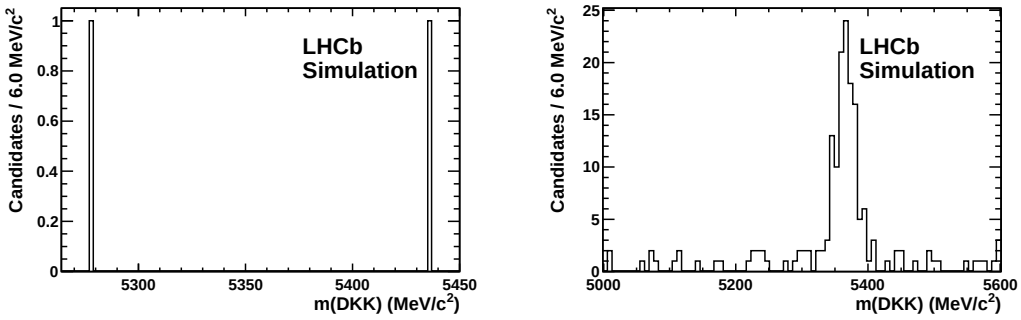

Figure 4.10: Invariant mass distribution of events passing the $B^0 \to \bar{D}^0 K^+ K^-$ selection from (left) $B^0 \to D_s^{\mp} K^{\pm}$, (right) $B_s^0 \to D_s^{\mp} K^{\pm}$, both with $D_s^{\mp} \to K^+ K^- \pi^{\mp}$ (Note that (right) is identical to Fig. 3.10(right)).

A similar mode, $B^0 \to D^- K^+$ with $D^{\mp} \to K^+ K^- \pi^{\mp}$ was also checked and the B candidate mass distribution is shown in Fig. 4.11. Due to the fact that only 17 events from a sample of 200000 survive the selection, and no peak that corresponds to the D^- mass is observed in Fig. 4.9, this background is not considered further.

4.4 Combinatorial background

The combinatorial background extends over the entire range of B masses considered in this analysis. It is parametrised in the fit to the B candidate mass by a straight line. Generally combinatorial backgrounds can be studied using same sign events of the form $Dh^{\pm}h^{\pm}$. Since these final states do not conserve charge they must

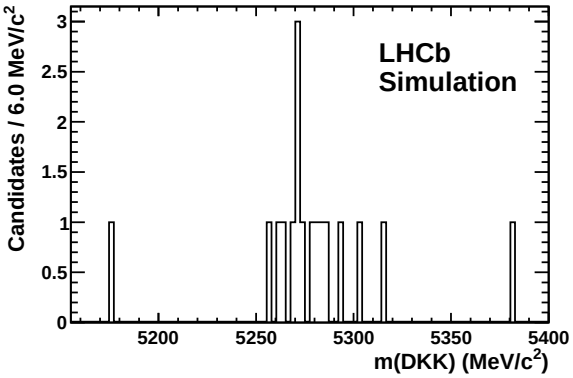

Figure 4.11: Events passing the $B^0 \to \bar{D}^0 K^+ K^-$ selection from $B^0 \to D^\mp K^\pm$ with $D^\mp \to K^+ K^- \pi^\mp$.

arise from a D meson combined with two random tracks, the same definition as combinatorial background. Unfortunately, this data sample was not available from the stripping selection for this analysis.

As an alternative, the combinatorial background shape can be studied using events from the D sidebands. The B invariant mass distribution of the sideband events can be fitted to extract the shape of the combinatorial background. It has been verified, using the $D\pi\pi$ data sample, that the slope of the linear function used to fit the combinatorial background in the D signal region is very similar to that in the D sidebands. Comparison of Fig. 4.16 in Sec. 4.5 and Fig. 5.6 in Sec. 5.4 illustrates this point. Hence for the DKK fit the slope is constrained to the value found in the D sidebands. The small discrepancy found in the $D\pi\pi$ case is considered as a source of systematic uncertainty in Sec. 7.

4.5 $D\pi\pi$ cross-checks

Since the $D\pi\pi$ signal has been previously observed, fewer background studies were required for peaking backgrounds. However, some cross checks were performed to make sure that nothing had been overlooked. Firstly, the generic simulated samples were checked again, using the $D\pi\pi$ initial selection. The four samples used were

- $B^0 \to DX$;
- $B_s^0 \to DX$;

- $B^+ \to DX$;
- $\Lambda_b \to DX$.

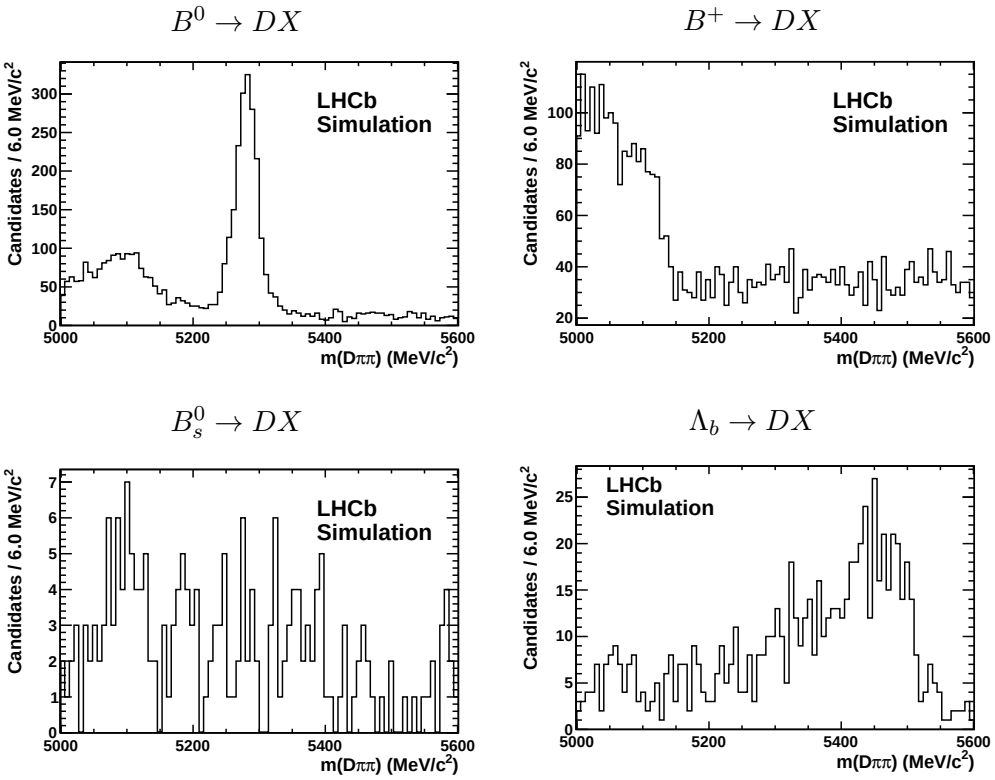

Figure 4.12: Invariant mass distributions of events passing the $B^0 \to \bar{D}^0\pi^+\pi^-$ initial selection from generic simulation samples. From the top left, going clockwise, they are: $B^0 \to DX$, $B^+ \to DX$, $\Lambda_b \to DX$ and $B_s^0 \to DX$.

The plots are shown in Fig. 4.12 and the most obvious feature is the signal peak seen in the $B^0 \to DX$ sample, since $D\pi\pi$ is an observed mode and it is included in the generic sample generation. By looking at the Dalitz plot projections, $m(D^0\pi^+)$ and $m(\pi^+\pi^-)$, the source of the signal can be discovered. In this case it is $D\rho^0(770)$ and $D^{*\pm}\pi^{\mp}$, as shown by Fig. 4.13. The low mass peak seen in the $B^+ \to DX$ sample can be neglected because the lower limit of the fit range is chosen to be 5150 MeV/c^2. The final feature of note is the high mass background present in the $\Lambda_b \to DX$ sample. This is probably from misidentification of $\Lambda_b \to Dp\pi^-$ and so this will be included in the $D\pi\pi$ fit.

The second check was to consider peaking charmless backgrounds in the same way as was described for the DKK decay mode in Sec. 4.3.1. The expected con-

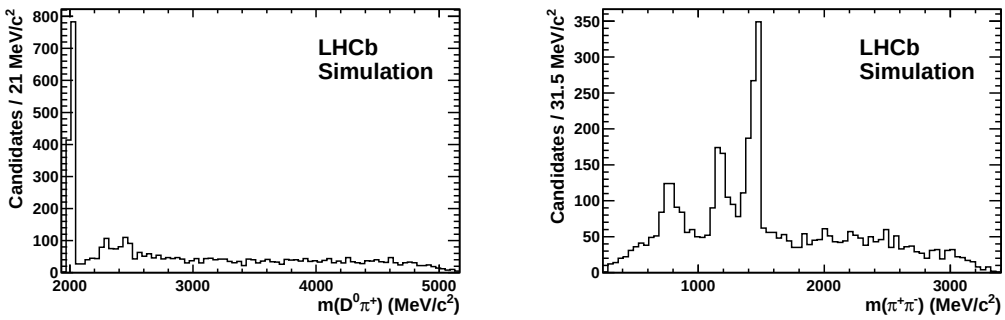

Figure 4.13: Two invariant mass projections for events shown in Fig. 4.12 (top left), (left) $m(D^0\pi^+)$ and (right) $m(\pi^+\pi^-)$. Note the reflection from the D^* appears as a double peak structure above 1000 MeV/c^2 in the $m(\pi^+\pi^-)$ distribution.

tribution of charmless background events from both upper and lower D sidebands to the final $D\pi\pi$ data sample is shown in Fig. 4.14. The individual sideband contributions are shown in Fig. 4.15. Note that they are shown twice as large to show the effect of all charmless events coming from a single sideband. Similarly to the DKK study, a peak is visible at the B^0 mass for the charmless background events. The B candidate invariant mass distribution of the charmless background events was fitted using a double Gaussian for the peaking signal and a linear function for the background, as shown in Fig. 4.16. The number of charmless background events forming a peaking background was 2345 ± 95 events, which scales to an expected 773 ± 30 events underneath the D mass peak.

A final check is to consider the final state particle combinations to look for sources of charmed backgrounds in the $D\pi\pi$ data sample. The combinations considered are as follows:

- Bachelor π^+ and K from D meson;
- Bachelor π^- and π from D meson;
- Both bachelors and K from D meson;
- Both bachelors and π from D meson.

The invariant mass distributions of the above combinations are shown in Fig. 4.17. The only feature of any note in these distributions is a very small peak at the D^0 mass in the $m(D^0(K^+)\pi^+)$ distribution. This is from either background

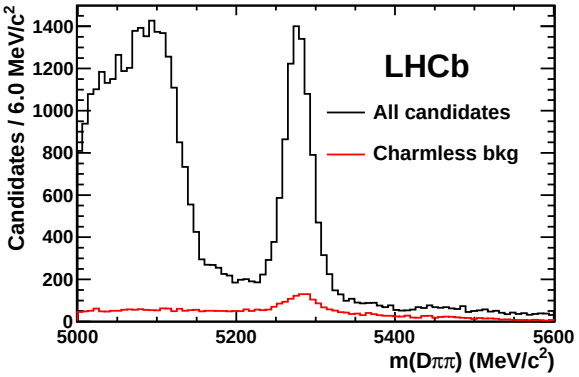

Figure 4.14: Expected pollution from charmless background events underneath the D mass peak (red line), estimated from events failing the D mass requirement. For comparison it is overlaid on the B candidate mass distribution from events passing the D mass requirement from the $D\pi\pi$ sample.

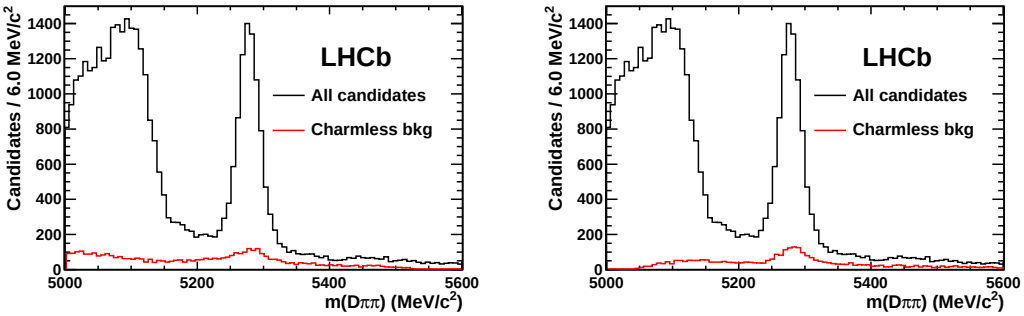

Figure 4.15: As Fig. 4.14 but for (left) lower and (right) upper D candidate mass sidebands separately. The contribution from each sideband is shown twice as large as in Fig. 4.14, to show the effect of all charmless events coming from a single sideband.

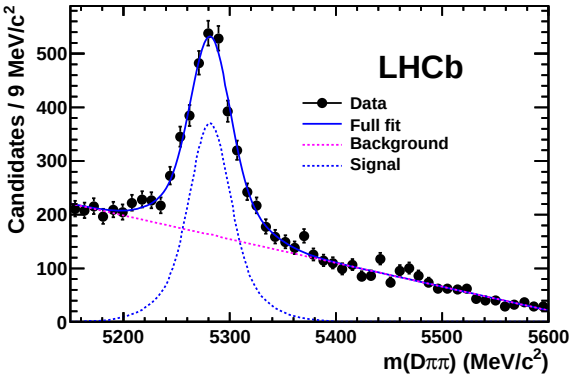

Figure 4.16: Fit to B candidate invariant mass distribution for events in the D sidebands for the $D\pi\pi$ decay mode. The data points are shown in black with the components of the fit overlayed; full fit (solid blue), double Gaussian signal (dashed blue) and linear background (dashed pink).

combinations or true signal events where the particles have been combined incorrectly. However, given the small size of the peak and the lack of peaking features this study is deemed to show nothing of concern to the analysis.

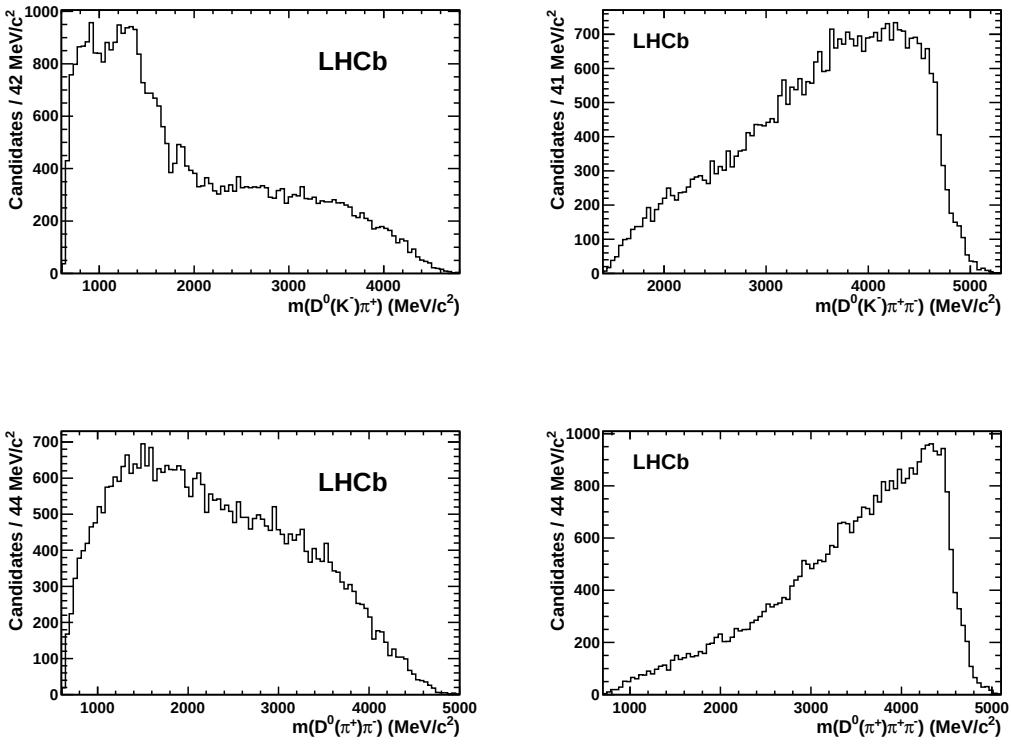

Figure 4.17: Combinations of particles in the $D\pi\pi$ data sample, (top left) K from D meson with bachelor π^+, (top right) K from D meson with both bachelors, (bottom left) π from D meson with bachelor π^- and (bottom right) π from D meson with both bachelors. $D^0(h)$ means the daughter h from the D^0 decay.

Chapter 5

Yield extraction

To extract the signal yield of each decay mode a fit to the B candidate invariant mass distribution is performed. The different parts of the fits are introduced in Sec. 5.1 and described in greater detail in Sec. 5.2. Validation of the fit procedure is given in Sec. 5.3 and the final fit to the data samples shown in Sec. 5.4.

5.1 Fitting strategy

Based on the background studies presented in Chap. 4 the following components of the two data samples are accounted for using a probability density function (PDF). For $D\pi\pi$ consider:

- B^0 signal;
- Partially reconstructed B decays;
- Combinatorial background;
- Peaking background from $\Lambda_b^0 \to DX$ decays.

For DKK consider:

- B^0 signal;
- B_s^0 signal;
- Partially reconstructed B decays;
- Combinatorial background;
- Peaking backgrounds from $B^0 \to \bar{D}^0 K^+\pi^-$, $B_s^0 \to \bar{D}^0 K^+\pi^-$ and $\Lambda_b \to D^0 pK^-$.

The final PDFs used to fit the DKK and $D\pi\pi$ mass distributions are a sum of all of the PDFs required to fit each mode. The fits are performed independently using the `RooFit` package [91]. The type of fit performed was an extended unbinned maximum log likelihood fit.

5.2 Fit components

5.2.1 Signal

The signal peaks are parametrised by a double Gaussian PDF with common means

$$\mathcal{P}_{\rm sig}(m) = (1-f)\,G(m;m_B,\sigma_1) + f\,G(m;m_B,\sigma_2)\ , \tag{5.1}$$

where f is the fraction between the area of each of the Gaussians. The results of fitting the DKK and $D\pi\pi$ simulated samples with the double Gaussian PDF are shown in Fig. 5.1. The parameters from the fits are listed in Tab. 5.1. The fits to simulated data samples demonstrate that the double Gaussian describes the signal shapes of both modes well.

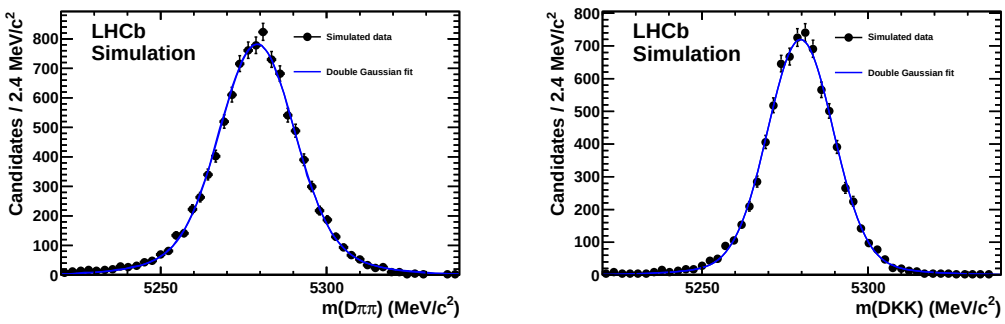

Figure 5.1: Fit to the B candidate invariant mass distribution for (left) $D\pi\pi$ and (right) DKK simulated samples.

A further consideration was to check that the signal shape was constant across the Dalitz plot. This is not an issue for yield extraction because the shape parameters are left free in the fit but it would cause a bias to the Dalitz plot distribution using `sWeights`. The variations of the mean and RMS of the B candidate mass distribution as a function of Dalitz plot position are shown in Fig. 5.2 and Fig. 5.3 respectively. No large effect is observed in either the width or the mean, allowing the Dalitz plot structure to be looked at reliably.

Parameter	$D\pi\pi$	DKK
m_B (MeV/c^2)	5279.1 ± 0.1	5279.7 ± 0.1
σ_1 (MeV/c^2)	10.9 ± 0.3	9.8 ± 0.2
σ_2 (MeV/c^2)	22 ± 1	24 ± 2
f	0.77 ± 0.04	0.90 ± 0.02

Table 5.1: Parameters of the signal double Gaussian shape (Eq. 5.1) obtained from fits to simulated samples.

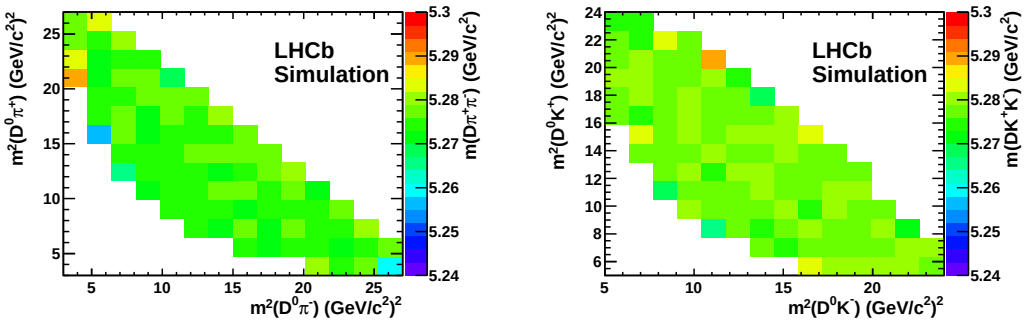

Figure 5.2: Mean of the B candidate mass distribution as a function of Dalitz plot position for reconstructed events in (left) $D\pi\pi$ and (right) DKK simulated samples. Note that the z axis scales are set to be the same in both plots.

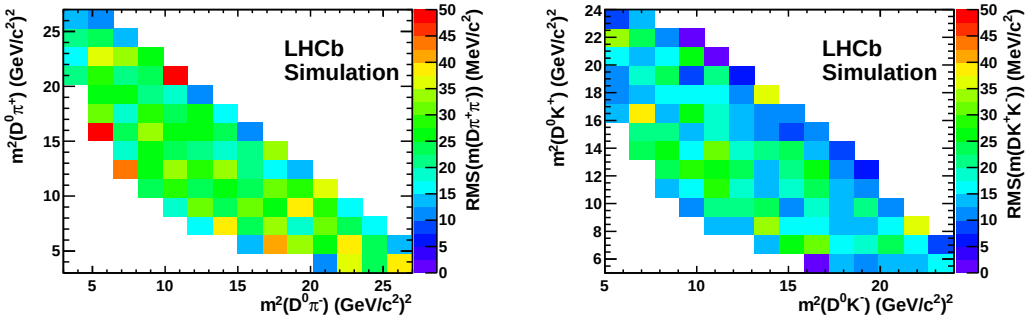

Figure 5.3: RMS of the B candidate mass distribution as a function of Dalitz plot position for reconstructed events in (left) $D\pi\pi$ and (right) DKK simulated samples. Note that the z axis scales are set to be the same in both plots.

In the fit to $D\pi\pi$ data, the ratio of the Gaussian widths is constrained to the value found in the fit to simulated data within Gaussian uncertainties. All other

parameters, mean, overall width and the fraction of events in each Gaussian are floated in the fit. The DKK signal fit follows the same method but the fraction of events in each Gaussian is constrained to the value found in the fit to simulated data, also within a Gaussian constraint. This is applied in addition to a constraint on the ratio of Gaussian widths. When a B_s^0 signal peak is also required it is fitted with exactly the same shape as the B^0 signal. The difference between the means of the two peaks is fixed to the world average value [5] of 86.8 ± 0.7 MeV/c^2.

5.2.2 Combinatorial background

The combinatorial background is fitted with a product of two PDFs, one to fit the combinatorial shape and one to correct this shape for events failing the fully constrained kinematic track fit. A linear PDF is used to fit the combinatorial shape. In the $D\pi\pi$ fit the slope and yield are free parameters. For the DKK fit the yield is floated but the slope of the PDF is constrained to the value extracted in a fit to data from the D mass sidebands. This method was cross-checked using $D\pi\pi$ data, where the combinatorial slope value was extracted from both a fit to the final data sample and data from the D sidebands. The slope from the sideband data agreed to within a few percent of the value from the fit to the final data sample and a systematic uncertainty was assigned to this procedure.

Figure 3.1 shows the distribution of events that fail the fully constrained kinematic fit. When these are subtracted from the final data sample, events are only lost at high values of the B invariant mass. The second PDF, used to correct for the events failing the fully constrained kinematic fit, is defined as:

$$f(x) = \begin{cases} 1 & \text{if } x \leq 5420 \text{ MeV}/c^2 \\ 1 - k(x - 5420 \text{ MeV}/c^2) & \text{if } x > 5420 \text{ MeV}/c^2, \end{cases} \tag{5.2}$$

where x is the invariant mass of the B candidates in MeV/c^2. The shape of this PDF reflects the fact that no events fail the kinematic fit below 5420 MeV/c^2. Therefore, the PDF must be flat until 5420 MeV/c^2, where a change of gradient occurs. The gradient, parameter k, was measured by fitting the B candidate invariant mass distribution of candidates that failed the fully constrained kinematic fit in the range $m_B > 5420$ MeV/c^2 and the results are summarised in Tab. 5.2. Note that this fit for k is completely independent of the final fit to the data samples.

Parameter	$D\pi\pi$	DKK
k	0.0249 ± 0.003	0.0273 ± 0.002

Table 5.2: Parameter of a fit to the B candidate invariant mass distribution of candidates failing the fully constrained kinematic fit. Parameter k is defined in Eq. 5.2.

5.2.3 Partially reconstructed B decays

For the $D\pi\pi$ fit an exponential function is used to fit the partially reconstructed background, with the slope and yield as free parameters. The DKK fit has only the yield as a free parameter, where the slope is constrained to that from the $D\pi\pi$ fit within Gaussian uncertainties. A systematic uncertainty is assigned to fixing this parameter, as discussed in Chap. 7.

5.2.4 Peaking background

One peaking background is included in the fit to $D\pi\pi$ data, $\Lambda_b \to DX$. In the fit to DKK data three components are included for $B^0 \to \bar{D}^0 K^+\pi^-$, $B_s^0 \to \bar{D}^0 K^+\pi^-$ and $\Lambda_b \to D^0 p K^-$ decay modes. All peaking backgrounds are included by generating a PDF from the B candidate invariant mass distribution of candidates from simulated data samples, as discussed in Sec. 4.3. The shape of each peaking background is, therefore, fixed. The normalisation and, therefore, the yield of each peaking background is a free parameter in the fits to data.

5.3 Simulation studies

The DKK data sample contains far fewer candidates than the $D\pi\pi$ data sample but requires three extra PDFs to be included in the fit. This could cause the fit to become unstable, so it was tested using simulation studies.

One thousand samples were generated from the nominal fit PDF with parameters set to their central values and then fitted using the `RooFit` package. The generated yield of each fit component was allowed to vary according to Poisson uncertainties, creating unique datasets. The central values that were used to generate the samples were taken from the fit to data, as described in Sec. 5.4.

The most important parameters extracted from the fit to the DKK data sample are the signal yields of $B^0 \to \bar{D}^0 K^+ K^-$ and $B_s^0 \to \bar{D}^0 K^+ K^-$. The variation of the $B^0 \to \bar{D}^0 K^+ K^-$ signal yield and the pull, $(N_{\text{fit}}(B^0) - N_{\text{gen}}(B^0))/\sigma(N(B^0)$, of the same parameter are shown in Fig. 5.4, and the Gaussian fit parameters are

summarised in Tab. 5.3. Here $N_{\rm fit}$ is the fitted signal yield and $N_{\rm gen}$ is the number of generated signal events. The study shows that $N(B^0 \to \bar{D}^0 K^+ K^-)$ is shifted by 8 events compared to the generated value. This is, however, much smaller than the uncertainty on $N(B^0 \to \bar{D}^0 K^+ K^-)$ from any one fit. Therefore no correction is applied and a systematic uncertainty is assigned.

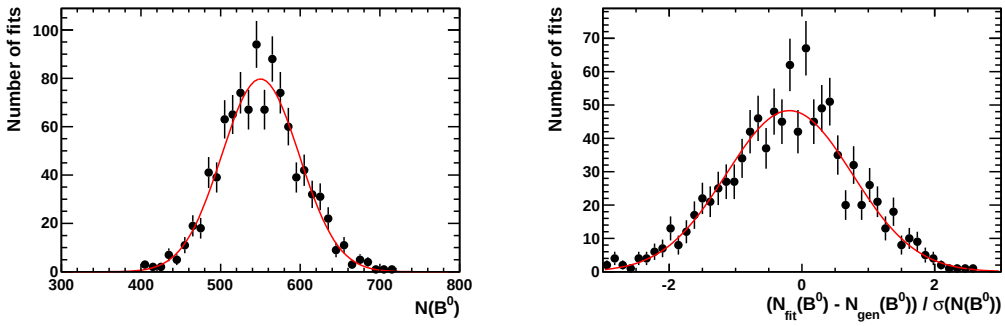

Figure 5.4: Variation of the $B^0 \to \bar{D}^0 K^+ K^-$ signal yield (left) and $(N_{\rm fit}(B^0) - N_{\rm gen}(B^0))/\sigma(N(B^0)$ (right) for fits to 1000 simulated samples. The red lines show Gaussian fits.

Fit parameter	**Yield (fit)**	**Yield (exp.)**	**Pull (fit)**	**Pull (exp.)**
$\mu_{B^0 \to \bar{D}^0 K^+ K^-}$	550 ± 2	558	-0.19 ± 0.03	0.0
$\sigma_{B^0 \to \bar{D}^0 K^+ K^-}$	48.5 ± 1.2	49	0.95 ± 0.02	1.0
$\mu_{B_s^0 \to \bar{D}^0 K^+ K^-}$	101 ± 1	104	-0.13 ± 0.03	0.0
$\sigma_{B_s^0 \to \bar{D}^0 K^+ K^-}$	29.6 ± 0.7	29	0.98 ± 0.02	1.0

Table 5.3: Fit parameters from the Gaussian fits shown in Figs. 5.4 and 5.5.

Equivalent information for the $B_s^0 \to \bar{D}^0 K^+ K^-$ yield is shown in Fig. 5.5 and the parameters from the Gaussian fits are shown in Tab. 5.3. The fits show that the signal yield for the B_s^0 mode is shifted by 3 candidates with respect to the generated value. This is a very small effect compared to the uncertainty on the yield in a single fit. Therefore, no correction is applied and a systematic uncertainty is assigned.

5.4 Fit to data

The fit to the $D\pi\pi$ data sample is shown in Fig. 5.6. The fit consists of four components: signal, combinatorial background, partially reconstructed B decays and a peaking background from $\Lambda_b \to DX$. The fit parameters are shown in Tab. 5.4

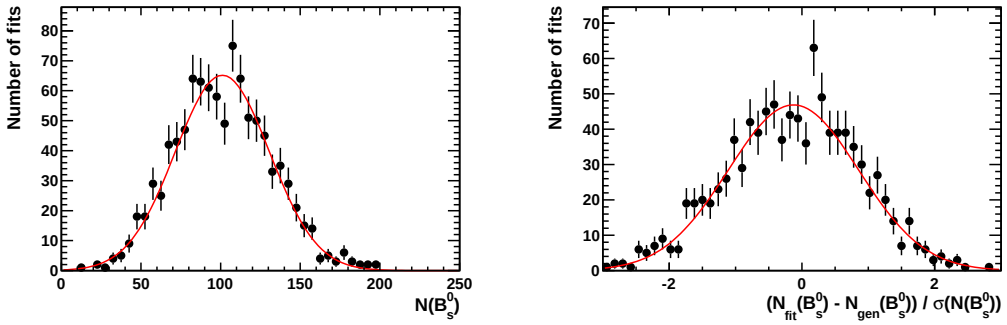

Figure 5.5: Variation of the $B_s^0 \to \bar{D}^0 K^+ K^-$ signal yield (left) and $(N_{\rm fit}(B_s^0) - N_{\rm gen}(B_s^0))/\sigma(N(B_s^0)$ (right) for fits to 1000 simulated samples. The red lines show Gaussian fits.

and the only parameter that is not completely free in the fit is the ratio of the Gaussian widths. The ratio of widths was constrained to the value shown in Tab. 5.1.

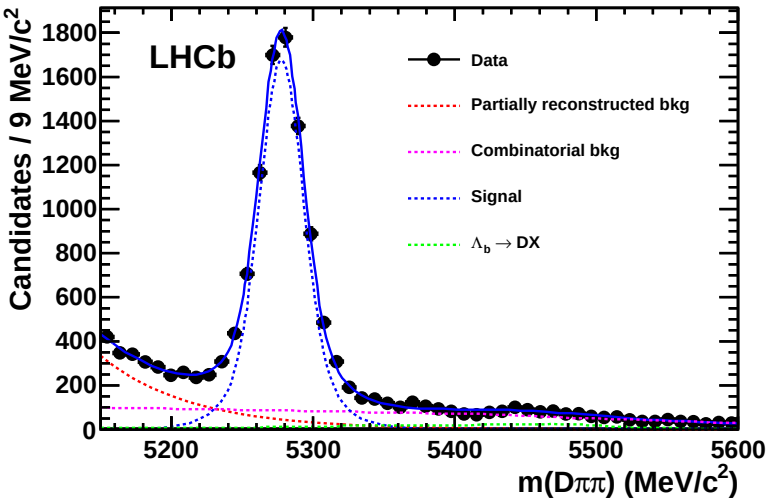

Figure 5.6: Fit to B candidate invariant mass distribution for $D\pi\pi$. Data points are shown in black, the combined fit as a solid blue line and the four fit components as dashed lines.

The fit to the DKK data sample is shown in Fig. 5.7. The fit includes seven components: signal, combinatorial background, partially reconstructed B candidates, $B_s^0 \to \bar{D}^0 K^+ K^-$ signal and three peaking backgrounds. Table 5.4 lists the parameters from the fit to the DKK data sample. The parameters in the fit that are not floated freely are the ratio of Gaussian widths, fraction of events in each Gaussian, and the slopes of the combinatorial and partially reconstructed B events. The ratio of widths and fraction parameters were constrained to the values shown

in Tab. 5.1, the partially reconstructed B decays slope was constrained to the value from the $D\pi\pi$ fit shown in Tab. 5.4 and the combinatorial slope was constrained to a value of $(-1.742 \pm 0.008) \times 10^{-4}$ from fitting events in the D mass sidebands.

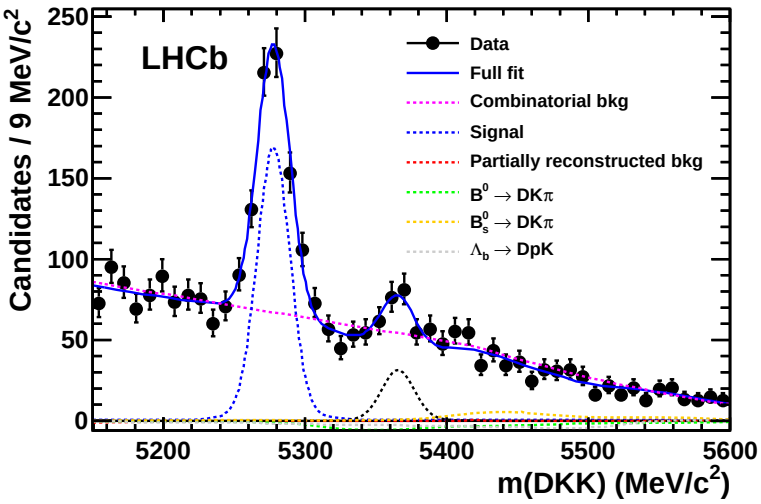

Figure 5.7: Fit to B candidate invariant mass distribution for DKK. Data points are shown in black, the combined fit as a solid blue line and the seven fit components as dashed lines.

The DKK fit returns negative yields for the partially reconstructed backgrounds and the peaking backgrounds from $B^0 \to \bar{D}^0 K^+ \pi^-$ and $\Lambda_b \to D^0 p K^-$. These are, however, consistent with zero within uncertainties.

Figure 5.8 shows the negative log likelihood, $-2\ln(L)$, plotted against the signal yield of $B^0 \to \bar{D}^0 K^+ K^-$ (left) and $B_s^0 \to \bar{D}^0 K^+ K^-$ (right). The other free parameters in the fit were kept at their global minimum values while the signal yields were scanned over the ranges shown. Both curves appear Gaussian in shape, which allows the charmless background contributions to be simply subtracted from the signal yield found in the fit to establish the significance of the observed signals.

Parameter	$D\pi\pi$	DKK
m_B	5278.1 ± 0.2 MeV/c^2	5278.1 ± 0.8 MeV/c^2
σ_1	14.7 ± 0.6 MeV/c^2	11.5 ± 0.9 MeV/c^2
σ_2/σ_1	2.03 ± 0.10	2.45 ± 0.10
Fraction (f)	0.73 ± 0.05	0.94 ± 0.09
Linear slope	$(-1.67 \pm 0.05) \times 10^{-4}$	$(-1.74 \pm 0.01) \times 10^{-4}$
Exponential slope	$(-1.6 \pm 0.3) \times 10^{-2}$	$(-1.6 \pm 0.8) \times 10^{-2}$
$n_{\mathrm{B}^0 \to \mathrm{Dhh}}$	8056 ± 149 events	558 ± 49 events
$n_{\mathrm{part.reco.bkg}}$	2358 ± 424 events	-8 ± 107 events
$n_{\mathrm{comb.bkg}}$	3258 ± 546 events	2485 ± 284 events
$n_{\Lambda_b \to DX}$	542 ± 177 events	-
$n_{B_s \to Dhh}$	-	104 ± 29 events
$n_{B_d \to DK\pi}$	-	-108 ± 142 events
$n_{B_s \to DK\pi}$	-	81 ± 90 events
$n_{\Lambda_b \to DpK}$	-	-121 ± 96 events

Table 5.4: Parameters from the fit to $D\pi\pi$ and DKK data samples.

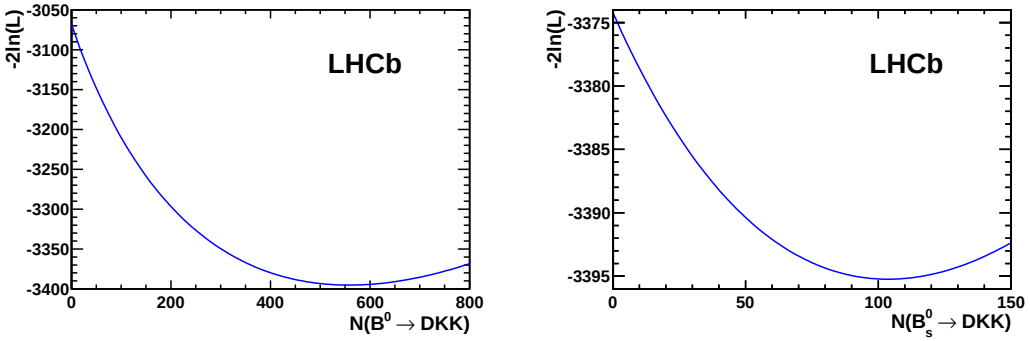

Figure 5.8: Negative log likelihood of the fit to DKK data, $-2\ln(L)$, plotted against the signal yield of $B^0 \to DKK$ (left) and $B_s^0 \to DKK$ (right).

Chapter 6

Results

The nominal result is obtained by using efficiency corrections on an event-by-event basis. This method accounts for variation of efficiencies across the Dalitz plot. `sWeights` are extracted from fits to both $D\pi\pi$ and DKK data samples, as described in Sec. 5.4. The corrected number of candidates is calculated using the following equation:

$$N^{\text{corr}}(Dhh) = \sum_i \frac{W_i}{\epsilon_i^{\text{tot}}} = \sum_i \frac{W_i}{\epsilon_i^{\text{geom}}\,\epsilon_i^{\text{sel|geom}}\,\epsilon_i^{\text{PID|sel\&geom}}\,\epsilon_i^{\text{trig|PID\&sel\&geom}}}\,, \qquad (6.1)$$

where i is an index that runs over all events in the fitted range and W_i is the signal `sWeight` for an event i. The various ϵ_i terms are efficiencies as defined in Sec. 3.6. The `sWeights` only depends on $m(Dhh)$ and the efficiencies on Dalitz plot position. The values obtained for $N^{\text{corr}}(Dhh)$ are presented in Tab. 6.1.

	DKK	$D\pi\pi$
N	558 ± 49	8056 ± 149
N^{corr}	$86\,169 \pm 7520$	$1\,308\,563 \pm 25\,067$
N^{peak}	126 ± 18	773 ± 30

Table 6.1: The corrected number of events, calculated from Eq. 6.1, the raw number of events and the number of peaking background events for DKK and $D\pi\pi$.

An added complication is to subtract the charmless peaking background under the B mass peak, as discussed in Secs. 4.3.1 and 4.5. The yields of these backgrounds were obtained from a fit to events without the D mass constraint in the kinematic fit, so the Dalitz plot boundaries are different to candidates in the nominal fit. Therefore, event-by-event efficiency corrections cannot be used. Instead the average efficiency is assumed to be the same as for the true signal candidates and

the corrected yield is scaled by a factor $(1-N^{\rm peak}/N)$. Parameters $N^{\rm peak}$ and N are the peaking background yield and the raw yield from the nominal fit, respectively, and both are shown in Tab. 6.1.

The ratio of branching fractions is then defined as

$$\frac{\mathcal{B}\left(B^0 \to \bar{D}^0 K^+ K^-\right)}{\mathcal{B}\left(B^0 \to \bar{D}^0 \pi^+ \pi^-\right)} = \frac{N^{\rm corr}(DKK)\left(1 - \frac{N^{\rm peak}(DKK)}{N(DKK)}\right)}{N^{\rm corr}(D\pi\pi)\left(1 - \frac{N^{\rm peak}(D\pi\pi)}{N(D\pi\pi)}\right)}\,. \tag{6.2}$$

Determination of the uncertainty on both the numerator and denominator of Eq. 6.2 is not trivial. The method used to calculated the uncertainty is described below.

- The uncertainty on $N^{\rm corr}$ is defined as [89]

$$\sigma(N^{\rm corr}) = \sqrt{\sum_i \left(\frac{W_i}{\epsilon_i^{\rm tot}}\right)^2}\,. \tag{6.3}$$

  However, the `sWeights` are calculated from a fit where only the PDF yields are free parameters, rather that floating shape parameters as in the nominal fit. This means that $\sigma(N^{\rm corr})$ must be corrected by finding the difference between the nominal fit and a yields-only fit.

- The uncertainty difference between the two fits is calculated by a subtraction in quadrature:

$$\sigma^{\rm shape}(N) = \sqrt{\sigma^{\rm fit}(N)^2 - \sigma^{\rm yields-only}(N)^2}, \tag{6.4}$$

  where $\sigma^{\rm yields-only}(N)$ and $\sigma^{\rm fit}(N)$ are the uncertainty on the yields-only fit and the nominal fit respectively.

- The correction, $\sigma^{\rm shape}(N)$, is applied to $\sigma(N^{\rm corr})$ after scaling it by a factor $N^{\rm corr}/N$:

$$\sigma^{\rm corr}(N^{\rm corr}) = \sqrt{\sigma(N^{\rm corr})^2 + \left(\frac{N^{\rm corr}}{N}\sigma^{\rm shape}(N)^2\right)}. \tag{6.5}$$

  These are the uncertainties on $N^{\rm corr}$ shown in Tab. 6.1

- The final step is to consider the uncertainty on the peaking background. The relative uncertainty is

$$\sigma^{\rm peak}_{\rm rel} = \frac{\frac{\sigma(N^{\rm peak})}{N^{\rm peak}}}{1 - \frac{N^{\rm peak}}{N}}, \tag{6.6}$$

  where the small uncertainty on N is neglected to avoid double counting.

- The total uncertainty for each of the numerator and denominator of Eq. 6.2 is

$$\sigma^{\text{tot}} = N^{\text{corr}} \left(1 - \frac{N^{\text{peak}}}{N}\right) \sqrt{\left(\frac{\sigma^{\text{corr}}}{N^{\text{corr}}}\right)^2 + (\sigma^{\text{peak}}_{\text{rel}})^2}. \tag{6.7}$$

Substituting the values from Tab. 6.1 into Eq. 6.2 gives the ratio of branching fractions to be:

$$\frac{\mathcal{B}\left(B^0 \to \bar{D}^0 K^+ K^-\right)}{\mathcal{B}\left(B^0 \to \bar{D}^0 \pi^+ \pi^-\right)} = 0.056 \pm 0.011 \pm 0.007, \tag{6.8}$$

where the first uncertainty is statistical and the second systematic. The systematic uncertainty is described in Chap. 7. Substituting in for the known value of $\mathcal{B}\left(B^0 \to \bar{D}^0 \pi^+ \pi^-\right) = (8.4 \pm 0.9) \times 10^{-4}$ from Ref. [5] gives:

$$\mathcal{B}\left(B^0 \to \bar{D}^0 K^+ K^-\right) = (4.7 \pm 0.9 \pm 0.6 \pm 0.5) \times 10^{-5}, \tag{6.9}$$

where the uncertainties are, from left to right, statistical, systematic and the uncertainty from the measurement of $\mathcal{B}\left(B^0 \to \bar{D}^0 \pi^+ \pi^-\right)$.

A measurement of the ratio of branching fractions for $B^0_s \to \bar{D}^0 K^+ K^-$ and $B^0 \to \bar{D}^0 K^+ K^-$ is also presented. Given the low statistics, event-by-event weighting is not used and instead the average efficiency across the Dalitz plot is assumed to be the same for the two decay modes. A systematic uncertainty is assigned to account for possible differences between the two Dalitz plots. No charmless background is subtracted from the B^0_s yield because no peak is seen in Fig. 4.2. The equation used is then

$$\frac{\mathcal{B}\left(B^0_s \to \bar{D}^0 K^+ K^-\right)}{\mathcal{B}\left(B^0 \to \bar{D}^0 K^+ K^-\right)} = \left(\frac{f_s}{f_d}\right)^{-1} \frac{N(B^0_s \to DKK)}{N(B^0 \to DKK) - N^{\text{peak}}(B^0 \to DKK)}, \tag{6.10}$$

where f_s/f_d is the ratio of fragmentation fractions and has a value of $0.267^{+0.021}_{-0.020}$ [92]. The ratio of fragmentation fractions describes how many B^0_s mesons are created in the pp collisons with respect to B^0 mesons. Inserting the measured values gives

$$\frac{\mathcal{B}\left(B^0_s \to \bar{D}^0 K^+ K^-\right)}{\mathcal{B}\left(B^0 \to \bar{D}^0 K^+ K^-\right)} = 0.90 \pm 0.27 \pm 0.20, \tag{6.11}$$

where the first uncertainty is statistical and the second is systematic. The uncertainty on f_s/f_d is included in the systematic uncertainty, which is described in more detail in Chap. 7.

Finally the significance of each signal was evaluated using the following equa-

tion:

$$\text{significance} = \frac{s_{\text{stat}}}{\sqrt{1 + \left(\frac{\sigma_{\text{syst}}}{\sigma_{\text{stat}}}\right)^2}}, \tag{6.12}$$

where s_{stat} is the statistical significance obtained from the change in $-2\ln\mathcal{L}$, calculated using Fig. 5.8. Substituting in the various terms for $B^0 \to \bar{D}^0 K^+ K^-$ gives a significance of 5.8 standard deviations and for $B_s^0 \to \bar{D}^0 K^+ K^-$ a significance of 3.8 standard deviations.

6.1 Dalitz plot structure

6.1.1 $D\pi\pi$

The Dalitz plot distributions for candidates in the B mass signal region is shown in Fig. 6.1 (left) and reconstructed from signal `sWeights`, calculated from the fit in Sec. 5.4, in Fig. 6.1 (right). Projections of the `sWeighted` Dalitz plot to show the invariant mass distributions are shown in Fig. 6.2. All of these plots were generated using quantities from the fully constrained kinematic fit.

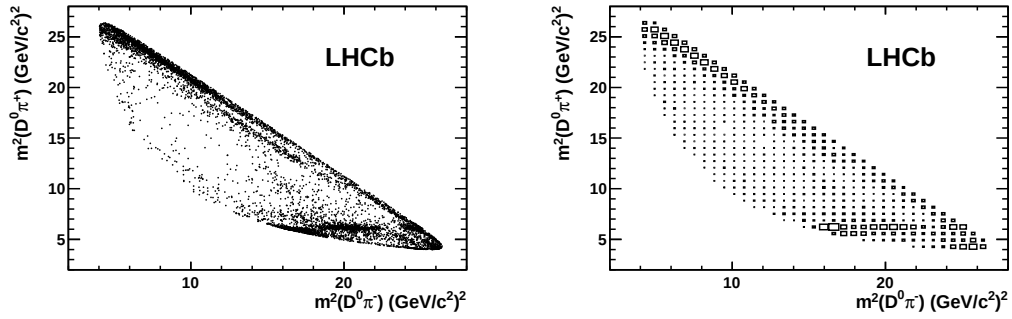

Figure 6.1: $B^0 \to \bar{D}^0 \pi^+ \pi^-$ Dalitz plots. (Left) all candidates in the B mass signal region; (Right) distribution reconstructed from `sWeights`.

Several resonances are visible on the Dalitz plots as horizontal and diagonal bands in Fig. 6.1. The clearest band is from the $\rho^0(770)$ and appears on the diagonal axis of the Dalitz plot. It is also clearly visible in the $m(\pi^+\pi^-)$ projection. A fainter diagonal band is also visible, most clearly on the scatter plot in Fig. 6.1. It has a three lobe structure (the diagonal band has two gaps in it) which is characteristic of a tensor resonance, suggesting the $f_2(1270)$ for example. A small peak in the $m(\pi^+\pi^-)$ invariant mass plot can be seen to correspond with this resonance. Finally, a horizontal band, again with a three lobe structure, is clearly visible on both Dalitz plots in Fig. 6.1. This is the $D_2^{*+}(2460)$ as can clearly be seen in the projection of

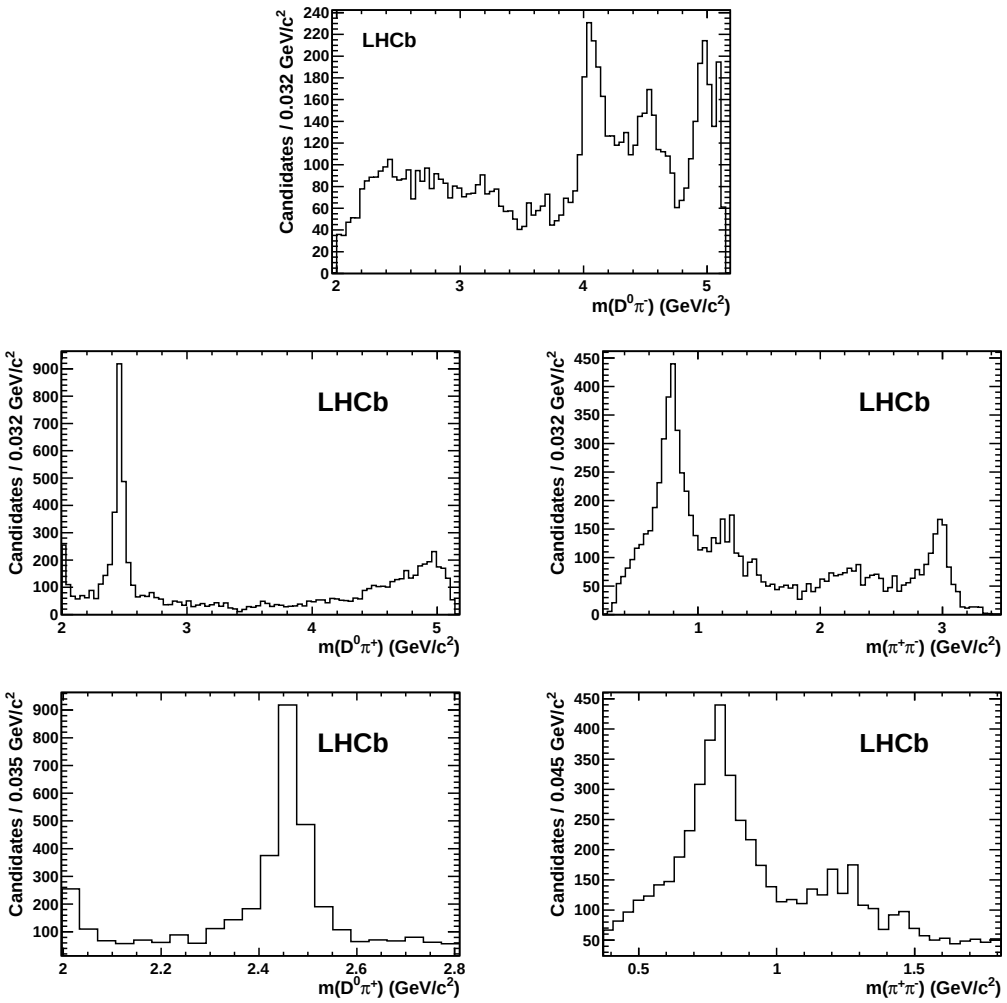

Figure 6.2: Invariant mass distributions of $B^0 \to \bar{D}^0\pi^+\pi^-$ decays, obtained from `sWeights`. The plots are: $m(D^0\pi^-)$ (top), $m(D^0\pi^+)$ (left middle), $m(\pi^+\pi^-)$ (right middle) with the corresponding zoomed view for $m(D^0\pi^+)$ and $m(\pi^+\pi^-)$ below the respective plots.

$m(D^0\pi^+)$. The observed $D\pi\pi$ Dalitz plot appears to be consistent with previous studies, see for example Refs. [93, 94]. This suggests that the method used to reconstruct the Dalitz plot from `sWeights` worked correctly.

6.1.2 DKK

The equivalent plots to those shown in Figs. 6.1 and 6.2 for the DKK final state are shown in Fig. 6.3 for the Dalitz plot distributions and Fig. 6.4 for the invariant mass projections. As with $D\pi\pi$, the Dalitz plot on the right of Fig. 6.3 and all invariant mass projections are reconstructed using signal `sWeights` from the fit described in Sec. 5.4.

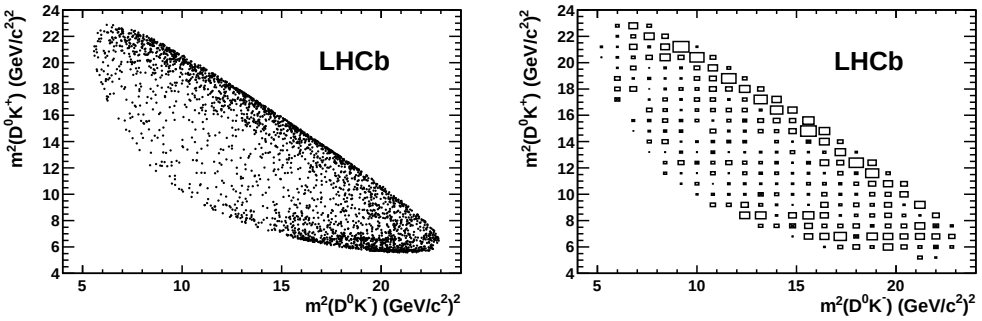

Figure 6.3: $B^0 \to \bar{D}^0 K^+ K^-$ Dalitz plots. (Left) all candidates in the B mass signal region; (Right) distribution reconstructed from `sWeights`.

The clearest structure on the Dalitz plot is the diagonal band, showing a zero lobe structure, characteristic of a spin zero resonance. With limited statistics it is certainly not conclusive but this appears consistent with the $a_0^0(980)$ state, as seen in the invariant mass projection of $m(K^+K^-)$. A second visible structure on the Dalitz plot is a horizontal band. Inspection of the $m(D^0K^+)$ invariant mass projection suggests it is the $D_{s2}^{*+}(2573)$ resonance.

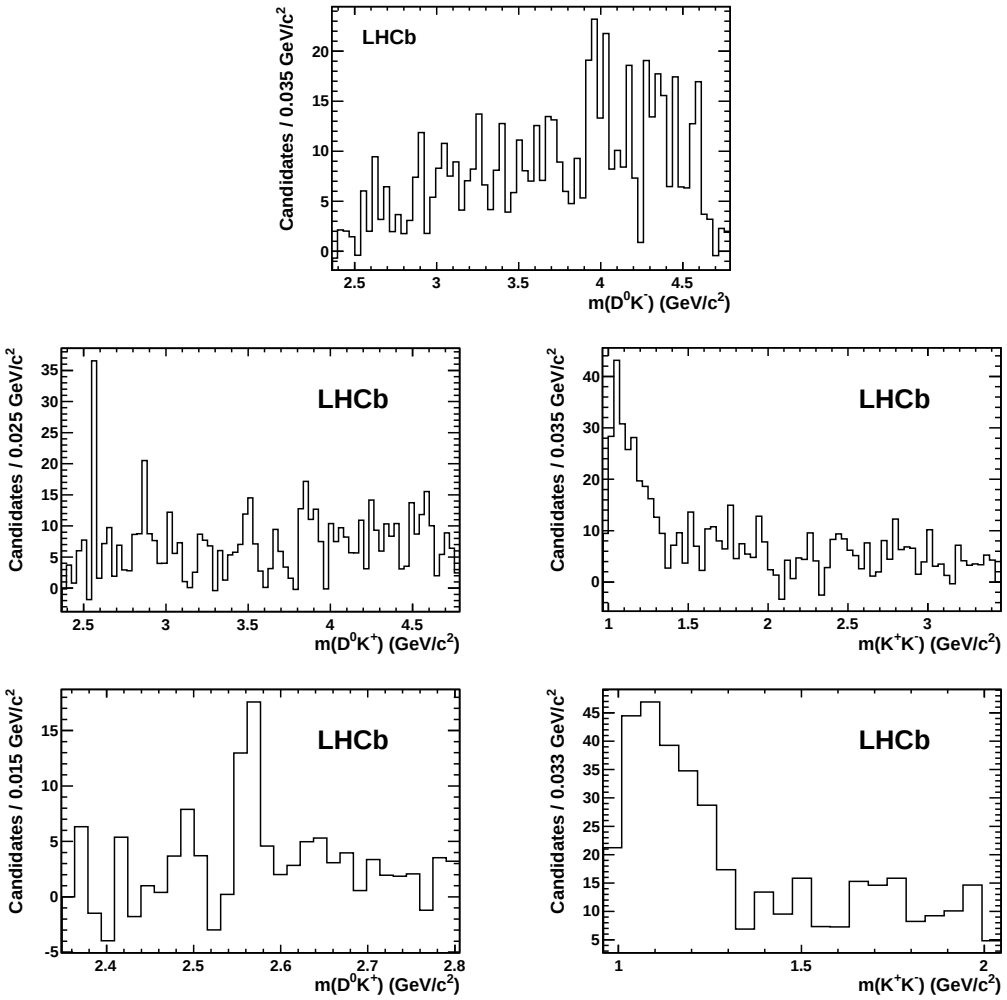

Figure 6.4: Invariant mass distributions of $B^0 \to \bar{D}^0 K^+ K^-$ decays, obtained from `sWeights`. The plots are: $m(D^0 K^-)$ (top), $m(D^0 K^+$ (left middle), $m(K^+ K^-$ (right middle) with the corresponding zoomed view for $m(D^0 K^+)$ and $m(K^+ K^-)$ below the respective plots.

Chapter 7

Systematic uncertainties

This chapter considers the various sources of systematic uncertainty that affect the measurements presented in this thesis. Some cross-checks are also performed to ensure that further systematic uncertainties are not present at a non-negligible level. The systematic uncertainties on the $\mathcal{B}\left(B^0 \to \bar{D}^0 K^+ K^-\right) / \mathcal{B}\left(B^0 \to \bar{D}^0 \pi^+ \pi^-\right)$ branching fraction ratio are summarised in Tab. 7.1 and described below. Secondly, the systematic uncertainties on the ratio of branching fractions to the DKK final state, $\mathcal{B}\left(B_s^0 \to \bar{D}^0 K^+ K^-\right) / \mathcal{B}\left(B^0 \to \bar{D}^0 K^+ K^-\right)$, are summarised in Tab. 7.2 and are also described below.

Source	**Uncertainty**
Trigger	2.0 %
D_s veto	1.7 %
MC modelling of efficiency	6.7 %
Particle identification	2.0 %
Fit model	10.1 %
Fit bias	1.5 %
Peaking background subtraction	1.5 %
Total	12.7 %

Table 7.1: Summary of systematic uncertainties on the $B^0 \to \bar{D}^0 K^+ K^-$ and $B^0 \to \bar{D}^0 \pi^+ \pi^-$ branching fraction ratio. The total is calculated as the sum in quadrature of all contributions.

Source	Uncertainty
MC modelling of efficiency	6.7 %
Fit model	19.5 %
Fit bias	3.4 %
Peaking background subtraction	1.5 %
f_s/f_d	7.9 %
Total	22.4 %

Table 7.2: Summary of systematic uncertainties on the ratio of B_s^0 and B^0 branching fractions to DKK. The total is calculated as the sum in quadrature of all contributions.

7.1 Trigger efficiency

There is a potential disagreement between data and simulation on the efficiency of the hardware hadron trigger that may not cancel in the ratio of $B^0 \to \bar{D}^0 K^+ K^-$ and $B^0 \to \bar{D}^0 \pi^+ \pi^-$ branching fractions. Previous studies [95] have found the difference in the relative efficiencies of kaons and pions to fire this trigger to be less than 2 % per track, yielding a 4 % uncertainty due to the presence of two bachelor tracks. Only approximately half of the data sample passes this trigger requirement so the final systematic uncertainty assigned is halved. Therefore, an uncertainty of 2 % is assigned. Note that this does not affect the ratio of B_s^0 and B^0 to DKK branching fractions.

7.2 Event selection efficiency

Most event selection effects cancel in the ratio of branching fractions. Exceptions to this are requirements that differ between the DKK and $D\pi\pi$ final states; particle identification and the D_s^+ veto. The systematic uncertainty due to the D_s^+ veto was evaluated by removing the veto completely and by widening the veto. The results of this study are shown in Tab. 7.3 and a systematic uncertainty of 1.7 % is assigned for the D_s^+ veto. Particle identification is discussed below in Sec. 7.4. Note that no systematic uncertainty is assigned for event selection in the B_s^0 and B^0 to DKK ratio measurement.

Requirement	$N(B^0 \to DKK)$ **(fit)**	$N(B^0 \to DKK)$ **(corr)**
No veto	548 ± 47	84789 ± 5777
1950–1975 MeV/c^2 (nominal)	558 ± 49	86168 ± 5669
1940–1985 MeV/c^2	553 ± 46	85533 ± 5767

Table 7.3: Stability of the results to variation in the D_s^+ veto requirement.

7.3 Efficiency variation across the Dalitz plot

An uncertainty arises related to how well the simulated data model the variation of the various efficiencies over the Dalitz plot. This is conservatively estimated by taking the difference between the nominal result using event-by-event efficiencies and one using the efficiencies averaged over the Dalitz plot. This is done for ϵ^{geom}, $\epsilon^{\text{sel|geom}}$ and $\epsilon^{\text{trig|PID\&sel\&geom}}$ simultaneously and contributes 6.7 % to the systematic uncertainty.

7.4 Particle identification

The systematic uncertainty assigned is 0.5 % for each pion track and 0.5 % for each kaon track. These are then added linearly to account for correlations giving a total systematic uncertainty of 2 % in the $DKK/D\pi\pi$ ratio. These are in line with previous studies at LHCb, such as [96, 97]. Once again, note that this systematic uncertainty does not also apply to the B_s^0 and B^0 to DKK ratio measurement.

7.5 Fit model

The systematic uncertainty from the fit models is evaluated from several sources as detailed below and summarised in Tabs. 7.4 and 7.5. For the $D\pi\pi$ final state:

- Remove $\Lambda_b \to DX$ component;
- Change the slope of the combinatorial background to zero and double the nominal value.

For the DKK final state:

- Remove PDF for each peaking background one at a time;
- Remove PDF for partially reconstructed B candidates;
- Include $B_s^0 \to D^* K^{*0}$ component;

- Vary the combinatorial slope by $\pm 10\,\%$.

The combinatorial slope for the DKK fit is constrained to the value found in the D candidate sidebands, given that the $D\pi\pi$ mode agrees to within $6\,\%$. Therefore, a variation of $\pm 10\,\%$ seems reasonable. Greater variation of the combinatorial slope was required for the $D\pi\pi$ mode because fewer checks were performed while developing the fit model, since it is a simple and stable fit. The $B_s^0 \to D^* K^{*0}$ component was considered for the DKK mode because it was the only other peaking background described in Sec. 4.3 that could have been dangerous.

Source	**Uncertainty**
No $\Lambda_b \to DX$	$1.3\,\%$
Combinatorial slope	$0.9\,\%$
Total	$1.6\,\%$

Table 7.4: Summary of systematic uncertainties due to the fit model for the $D\pi\pi$ final state. The total is obtained from the sum in quadrature of all contributions.

Source	**Uncertainty** (B^0)	**Uncertainty** (B_s^0)
Add $B_s^0 \to D^* K^{*0}$	$5.1\,\%$	$1.9\,\%$
No $B^0 \to DK\pi$	$2.3\,\%$	$7.7\,\%$
No $B_s^0 \to DK\pi$	$3.0\,\%$	$9.6\,\%$
No $\Lambda_b \to DpK$	$1.6\,\%$	$1.0\,\%$
No part. reco. bkgd.	$0.3\,\%$	$0.0\,\%$
Vary combinatorial slope	$7.6\,\%$	$11.1\,\%$
Total	$10.0\,\%$	$16.7\,\%$

Table 7.5: Summary of systematic uncertainties due to the fit model for the DKK final state. The total is obtained from the sum in quadrature of all contributions.

7.6 Fit bias

The simulation study presented in Sec. 5.3 showed a small bias of 8 ± 2 candidates in the $B^0 \to \bar{D}^0 K^+ K^-$ signal yield. Essentially, this is negligible but to be conservative a systematic uncertainty of $1.5\,\%$ is applied. Similarly, the $B_s^0 \to \bar{D}^0 K^+ K^-$ signal yield had a bias of 3 ± 1 candidates so an uncertainty of $3\,\%$ is assigned.

7.7 Peaking background subtraction

Two sources of uncertainty are associated with this procedure. Firstly the peaking backgrounds were estimated using quantities without the D mass constraint in the kinematic fit, so the distribution is slightly different to the nominal fit. However, this effect is assumed to be small and adequately covered by the systematic uncertainties from the fit model.

Secondly, the average efficiency of peaking background events may be different from that of the true signal events, due to different variations of efficiency over the Dalitz plot. This was evaluated in Sec. 7.3 with a value of 6.7 %. Scaling this by the peaking background fraction, $N^{\rm peak}/N = 126/558$ yields a systematic uncertainty of 1.5 %.

7.8 Ratio of fragmentation fractions

The uncertainty on $f_s/f_d = 0.267^{+0.021}_{-0.020}$ [92] is 7.9 %.

7.9 Cross-checks

7.9.1 L0 selection

To check for any effect from the hardware trigger the data samples are divided into three parts; events passing only the hadronic trigger requirement on the signal decay, events passing only the global trigger requirement on the rest of the event and events that pass both trigger selections, referred to as hadronic, global and both respectively in Tab. 7.6.

Requirement	$N(B^0 \to DKK)$	$N(B^0 \to D\pi\pi)$	$\epsilon^{\rm trig}_{B^0\to DKK}$	$\epsilon^{\rm trig}_{B^0\to D\pi\pi}$	**Double ratio**
Nominal	558 ± 49	8056 ± 149	96.5 %	97.2 %	0.07 ± 0.01
Hadronic	244 ± 29	3611 ± 103	97.3 %	98.5 %	0.07 ± 0.01
Global	217 ± 29	2169 ± 60	94.6 %	95.5 %	0.10 ± 0.01
Both	142 ± 48	1896 ± 67	97.3 %	96.5 %	0.07 ± 0.03

Table 7.6: Stability of the results to the hardware trigger requirement. Recall that the nominal requirement is that events must pass a global trigger on the rest of the event or a hadronic trigger on the signal decay mode. Note that $\epsilon^{\rm trig} = \epsilon^{\rm trig|PID\&sel\&geom}$ is expressed for the software trigger requirement only. The double ratio is defined as $(N(B^0 \to DKK)/\epsilon^{\rm trig}_{B^0\to DKK})/(N(B^0 \to D\pi\pi)/\epsilon^{\rm trig}_{B^0\to D\pi\pi})$.

There is a slight effect noted in the double ratio of events from the global trigger requirement on the rest of the event. However, this is not deemed to be a

serious problem because the total efficiency of the nominal hardware trigger requirement is approximately 97 % for both final states. No further systematic uncertainty is assigned as a result of this cross check.

7.9.2 Neural network selection

The effect of using a neural network is checked by varying the requirement on the neural network output variable. The ratio of signal yields for $B^0 \to \bar{D}^0 K^+ K^-$ and $B^0 \to \bar{D}^0 \pi^+ \pi^-$ is compared for different requirements. Changing the requirement varies the number of combinatorial background events that pass the selection and therefore tests the relevant parts of the fit. The results of this study are shown in Tab. 7.7.

Requirement	$N(B^0 \to DKK)$	$N(B^0 \to D\pi\pi)$	**Ratio**
-0.6	593 ± 49	8786 ± 149	0.067 ± 0.007
-0.3 (nominal)	558 ± 49	8056 ± 149	0.069 ± 0.006
0.0	507 ± 44	7331 ± 137	0.069 ± 0.006
0.3	446 ± 40	6439 ± 130	0.069 ± 0.006

Table 7.7: Stability of the results to variation in the requirement on the neural network output variable.

The ratio of yields is very stable with respect to the requirement on the neural network output so no additional systematic uncertainty is assigned.

7.9.3 Particle identification requirement

The stability of the fit results with different particle identification requirements on the DKK sample was checked. This was done by checking the ratio of the fitted signal yield and the particle identification efficiency. The requirement values and the results of the study are summarised in Tab. 7.8 and no systematic uncertainty is assigned.

Requirement	N_{DKK}	$\epsilon^{\text{PID}\|\text{sel\&geom}}$	**Ratio**
$\text{DLL}_{K\pi} > 3$	638 ± 57	78.0 %	0.12 ± 0.01
$\text{DLL}_{K\pi} > 5$ (nominal)	558 ± 49	71.0 %	0.13 ± 0.01
$\text{DLL}_{K\pi} > 7$	519 ± 38	64.2 %	0.12 ± 0.01

Table 7.8: Stability of the fit results to variation in the PID requirement in the DKK data sample.

The nominal particle identification efficiency is obtained using a calibration sample of data that is used to create an efficiency map of a given particle identification ID requirement in terms of bachelor p and p_T. This is then used to obtain the particle identification efficiency of simulated signal samples that do not have a particle identification requirement applied. The stability of the result was checked using kinematics from real data for $D\pi\pi$ candidates using the `sPlot` technique, rather than the simulated samples. Using real data the particle identification efficiencies are 70.6 % for DKK and 78.2 % for $D\pi\pi$, which compare well to the nominal values of 71.0 % and 79.5 % respectively.

A second check is to apply a very loose proton veto to the bachelor track with opposite charge to the kaon from the D^0 decay. For $D\pi\pi$ the veto applied is $\mathrm{DLL}_{p\pi} < 10$ and for DKK it is $\mathrm{DLL}_{pK} < 10$. Such requirements should be very efficient on signal but still remove candidates that are likely to be from B baryon decays with protons misidentified as pions or kaons. The results are shown in Tab. 7.9. No problems are observed so no systematic uncertainty is assigned.

Requirement	N_{DKK}	$N_{D\pi\pi}$
Without proton veto	558 ± 49	8056 ± 149
With proton veto	574 ± 42	7948 ± 144

Table 7.9: Stability of the results to a loose proton veto on the DKK data sample.

7.9.4 Stripping selection

The stability of the result against the stripping selection used for each candidate is checked. The two data samples are the sum of data from `Stripping13b` and `Stripping15`. The results of this cross-check are shown in Tab. 7.10 and show that no large effects are present so no systematic uncertainty is applied.

Stripping selection	$N(B^0 \to DKK)$	$N(B^0 \to D\pi\pi)$	**Ratio**
Both (nominal)	558 ± 49	8056 ± 149	0.069 ± 0.006
`Stripping13b`	289 ± 29	4786 ± 90	0.060 ± 0.008
`Stripping15`	260 ± 36	3310 ± 112	0.078 ± 0.009

Table 7.10: Stability of the results for different stripping selections.

7.9.5 Magnet polarity

A final check was to search for any hidden problems within the data samples by separating candidates by magnet polarity and checking the stability of the results. The results of this study are shown in Tab. 7.11 and show that no systematic uncertainty needs to be considered.

Magnet polarity	$N(B^0 \to DKK)$	$N(B^0 \to D\pi\pi)$	**Ratio**
Both (nominal)	558 ± 49	8056 ± 149	0.069 ± 0.006
Up	198 ± 29	2927 ± 90	0.068 ± 0.010
Down	341 ± 36	5100 ± 112	0.067 ± 0.007

Table 7.11: Stability of the results under different magnet polarities.

Chapter 8

Summary

In approximately 0.62 fb^{-1} of data collected by LHCb during 2011, approximately 550 $B^0 \to \bar{D}^0 K^+ K^-$ decays were observed. The branching fraction was measured relative to that of $B^0 \to \bar{D}^0 \pi^+ \pi^-$ to be

$$\frac{\mathcal{B}\left(B^0 \to \bar{D}^0 K^+ K^-\right)}{\mathcal{B}\left(B^0 \to \bar{D}^0 \pi^+ \pi^-\right)} = 0.056 \pm 0.011 \pm 0.007\,, \tag{8.1}$$

where the first uncertainty is statistical and the second is systematic. The significance of the signal is 5.8 standard deviations.

Using the world average value of $\mathcal{B}\left(B^0 \to \bar{D}^0 \pi^+ \pi^-\right) = (8.4 \pm 0.4 \pm 0.8) \times 10^{-4}$ [51] yields

$$\mathcal{B}\left(B^0 \to \bar{D}^0 K^+ K^-\right) = (4.7 \pm 0.9 \pm 0.6 \pm 0.5) \times 10^{-5}\,, \tag{8.2}$$

where the third uncertainty is from the measurement of $\mathcal{B}\left(B^0 \to \bar{D}^0 \pi^+ \pi^-\right)$. This value is in agreement with the estimate discussed in Sec. 3.5.2 that the $B^0 \to \bar{D}^0 K^+ K^-$ branching fraction should be approximately 20 times smaller than that of $B^0 \to \bar{D}^0 \pi^+ \pi^-$.

An excess of approximately 100 DKK events in the B_s^0 region is also observed. The branching fraction of $B_s^0 \to \bar{D}^0 K^+ K^-$ was measured relative to that for $B^0 \to \bar{D}^0 K^+ K^-$ to be

$$\frac{\mathcal{B}\left(B_s^0 \to \bar{D}^0 K^+ K^-\right)}{\mathcal{B}\left(B^0 \to \bar{D}^0 K^+ K^-\right)} = 0.90 \pm 0.27 \pm 0.20\,, \tag{8.3}$$

where the first uncertainty is statistical and the second is systematic. The significance of the signal is 3.8 standard deviations.

The measurements presented in this thesis represent a very important start-

ing point towards future analyses of the $B \to DKK$ final state. Evidence for the B_s^0 decay mode provides an exciting prospect that a measurement of γ using this decay mode could be possible using the full 2011 and 2012 data samples from LHCb. A more certain short term prospect would be a full Dalitz plot analysis of the B^0 decay mode, to identify which intermediate resonances are responsible for the signal peak observed in this analysis. This study could be done using the full 2011 data sample to approximately double the available statistics or after the addition of a 2012 data sample. Finally, the methods and techniques used in this analysis also provide an excellent starting point for other analyses of $B \to Dhh$ decay modes. One very interesting example is the $B^0 \to DK\pi$ final state, which is sensitive to γ. This is another exciting prospect that could come from the analysis presented here using the 2011 and 2012 LHCb data samples.

Appendix A

Simulated VELO geometry description

This appendix describes how the VELO is modelled in the LHCb simulation software. The details and methods are covered in Sec. A.1, the actual geometry description of the detector in Sec. A.2 and a study of the amount of simulated material in the VELO in Sec. A.3. Finally a conclusion, Sec. A.4, compares the simulated material to that of the real detector.

A.1 Introduction

The detector description database (DDDB) contains information on the structure, geometry and materials of the LHCb detector. The VELO detector forms one subdirectory of the DDDB. The detector description is used by `GEANT4` [84] to simulate particles moving through the detector. The LHCb tracking code also uses the DDDB information to account for multiple scattering from particle interactions in material.

The geometry part of the VELO description is of interest here. Components of the detector are created from seven primitive types of solids. These are: boxes, tubes, spheres, cones, polyconical tubes, trapezoids and general trapezoids. These are based on volumes which the `GEANT4` toolkit can effectively handle. The primitive shapes can be combined using intersection, subtraction and union Boolean operations. Intersection preserves the region of overlap between two volumes, subtraction removes the area of overlap and union combines the two volumes together. Every Boolean operation generates a new solid, so that it is possible to subtract one union from another.

I was responsible for a major update to the VELO geometry description in

November 2009 to improve the description of passive parts of the VELO. My work included completely rebuilding the vacuum tank, improving the RF foil, adding detector supports, Kapton cables, connectors and pile-up modules. A second important task was to fix material overlaps in the description. An overlap occurs when two different elements occupy the same space and causes problems when the DDDB is used to track particles. A full breakdown of the work that I performed is included in Sec. A.2 and a more complete write up of the work is available from Ref. [98].

The simulated masses reported in this appendix are all from Ref. [98], and were calculated from density and volume information provided by the `GAUSS` package. The available production mass of elements from the real VELO detector are also from Ref. [98].

A.2 VELO geometry description

A.2.1 VELO

All of the VELO components in the geometry description are contained within a large cylindrical volume. The contents of the VELO are shown by Fig. A.1. The vacuum tank is shown in wire-frame mode to show the other components inside it. The four large grey volumes form the two VELO halves, described in Sec. A.2.2 and the remaining visible pieces are described below.

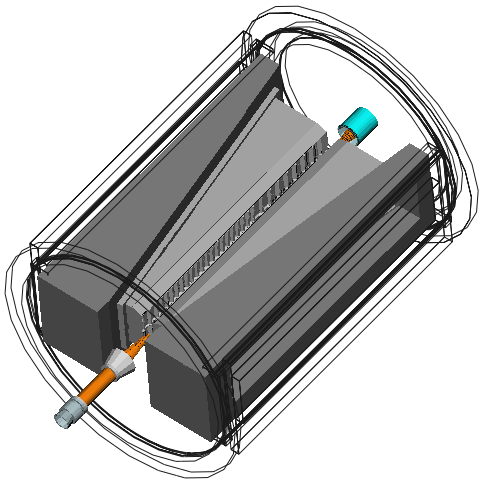

Figure A.1: The VELO shown with the vacuum tank in wire-frame to show the components inside it. Bottom left shows the upstream beam pipe and upstream wakefield cone and top right the downstream wakefield cone and beam pipe.

Wakefield cones

The wakefield cones are positioned at both ends of the VELO, attached to the end of the sections of beampipe. They are complex copper foils that are only partially modelled in the DDDB, since the wings that connect to the RF box are not yet included. The mass at production was 38.7 g compared to a mass in the DDDB of 13.219 g. The difference is due to the fact that they are not completely modelled. The more downstream of the two wakefield cones is shown in Fig. A.2.

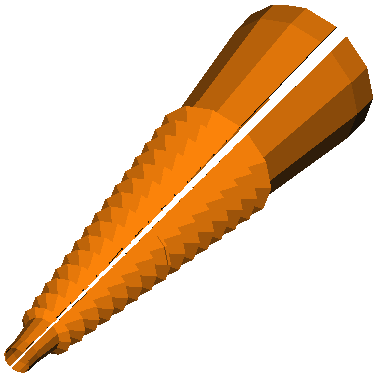

Figure A.2: The downstream wakefield cone.

Upstream beam pipe

The upstream beam pipe is a collection of tubes and cones made from copper, steel and aluminium. The elements forming the upstream beam pipe are shown in Fig. A.3 (left) and have a combined mass in the simulation of 1748.728 g. The mass at production is not currently known to the VELO group.

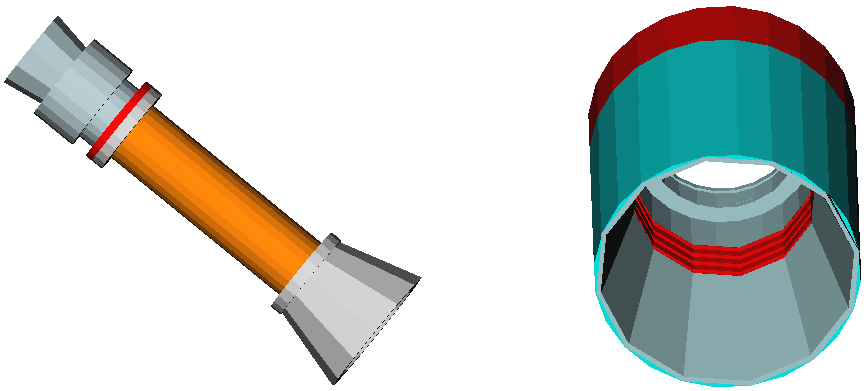

Figure A.3: The upstream beam pipe (left) and the downstream beam pipe (right).

Downstream beampipe

The downstream beam pipe is a collection of cylinders and cones, shown in Fig. A.3 (right). The beam pipe is also surrounded by gas volumes because it joins to the RICH1 detector description which is filled with gas. The mass of the downstream beam pipe section is 163.499 g and the true production mass is not known. Adding the gas volumes was one of my contributions as well as fixing some overlaps.

VELO Vacuum Tank

The VELO vacuum tank is a large, stainless steel vessel that encloses the whole VELO detector. It is shown in Fig. A.4 and the whole description was written by myself using engineering schematics. Some gas volumes are also included at the downstream end of the vacuum tank, where it joins with RICH1. The total mass of the simulated vacuum tank is 697053.099 g and the production value is not known.

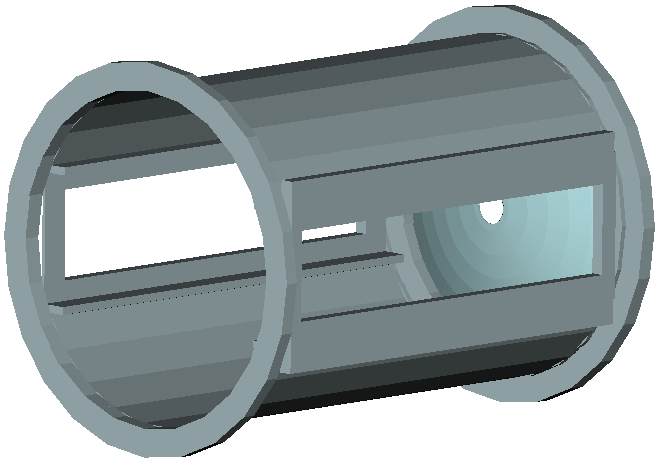

Figure A.4: The VELO vacuum tank.

A.2.2 VELO halves

The VELO halves each contain one half of the VELO detector. The left side is shown in Fig. A.5, containing 21 VELO modules, 2 pile-up modules and several supporting volumes described below. VELO modules are described in Sec. A.2.3 and pile-up modules in Sec. A.2.4.

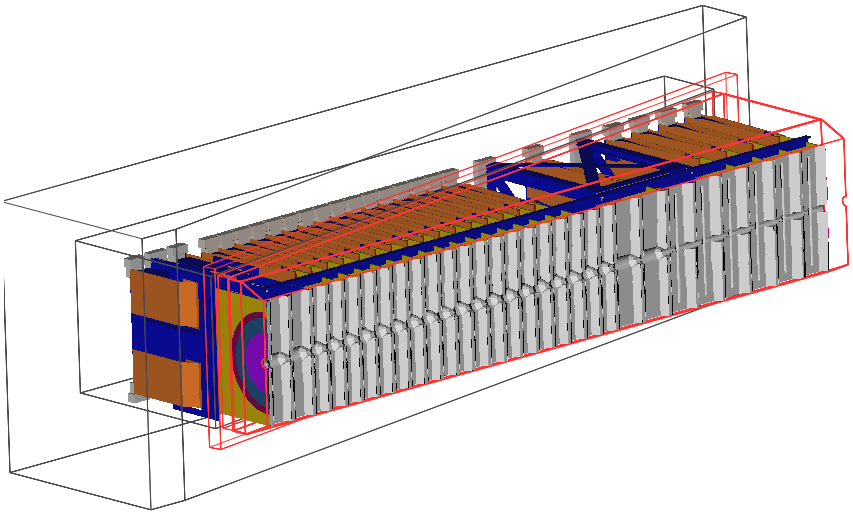

Figure A.5: The left side of the VELO. The RF box (red) and detector support (grey) are shown in wire-frame to show the internal elements.

RF box

The RF box is an aluminium box that houses the VELO modules and joins to the RF foil. The RF box from the left VELO half is shown in Fig. A.6, and the right side is identical. The mass of the RF box in the description, including the RF foil, is 4398.650 g. The production mass of the same components was 4073 g. Correcting overlaps in the RF box was one task I performed while improving the geometry description.

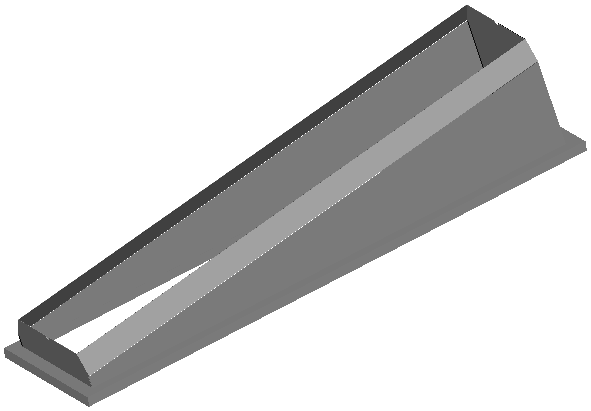

Figure A.6: The RF box on the left side of the VELO.

RF Foil

The RF foil is a corrugated aluminium foil that separates the VELO sensors from the beam. The RF foil has a general thickness of 300 microns which drops to 180 microns in the central region. The left side VELO RF foil is shown in Fig. A.7, and the right side foil is identical. The mass of the RF foil is 200.642 g in the simulation and approximately 174 g at production. The small corrugations shown in the top right of the figure and three full corrugations on the left of the figure were added by myself to improve the RF foil description. In addition I also fixed several overlaps.

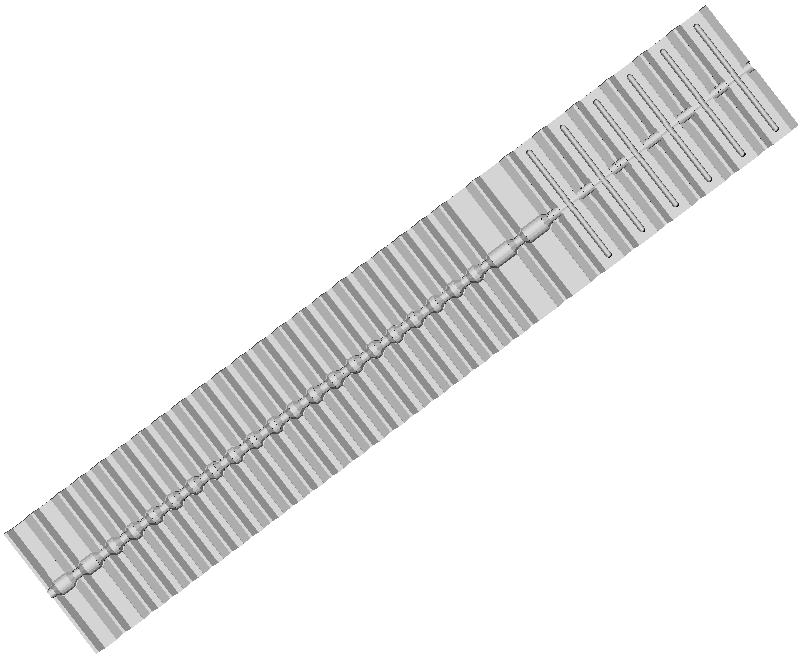

Figure A.7: The left side RF foil.

Detector supports

The detector supports are stainless steel structures to connect the RF box to the vacuum tank. The detector support from the left side of the VELO is shown in Fig. A.8 and is a mirror image of the right side detector support. The mass of these supports in the database is 59378.045 g and no production value is currently known. The detector supports were added by myself from schematic drawings to make the VELO geometry description more realistic.

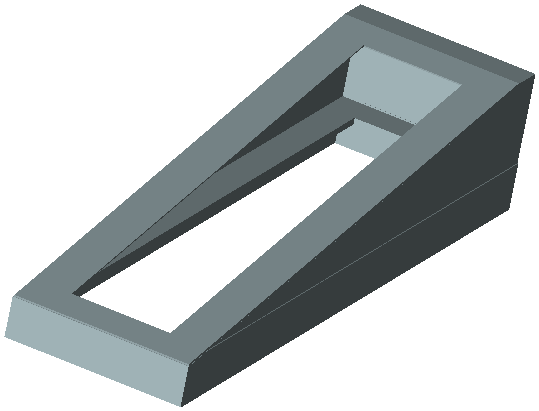

Figure A.8: The detector support on the left side of the VELO.

Constraint System

The VELO constraint system is a collection of carbon fibre elements that form a support for the VELO modules. The more complex supports between the pile-up sensors are also included in this volume. Figure A.9 shows the left side of the constraint system, and the right side is just a mirror image. The mass of the constraint system on each side is 1188.6 g and the combined mass at production is not currently known. I was responsible for adding the pile-up supports, which are visible in the bottom left of the figure.

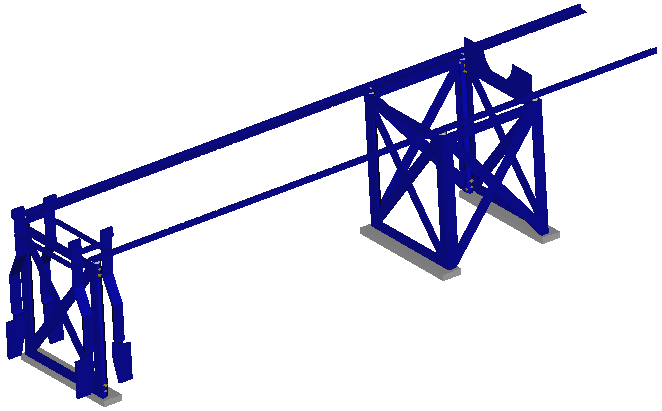

Figure A.9: The constraint system on the left side of the VELO.

A.2.3 VELO modules

The VELO module volumes contain the sensors, circuit boards and the supporting structures. The various elements are shown in Fig A.10 and are described below.

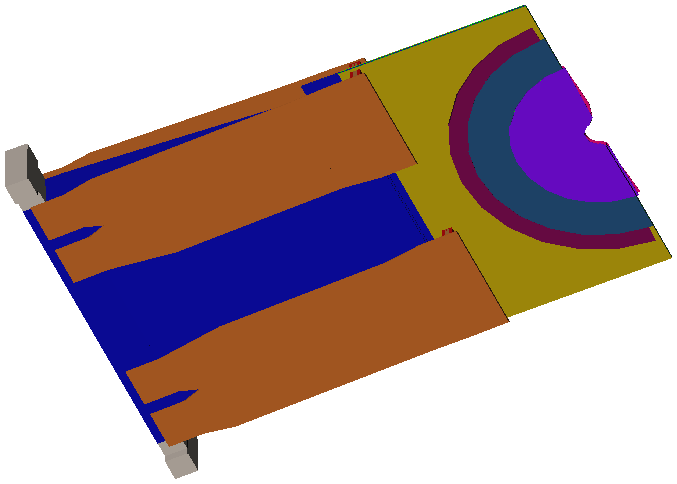

Figure A.10: A VELO module showing the paddle and base (blue), Kapton cables (orange), sensors (purple and pink)and hybrid (yellow).

R sensor

The VELO R sensor is a single volume of silicon, created from the union of half of a tube and two boxes. To make the sensors more realistic, I added two triangular subtractions to extend the circular cut out created by the tube, as can be seen in Fig. A.11 (left). The sensor is 0.3 mm thick and has a mass in the description of 2.14 g, while the average production mass was 2.252 g.

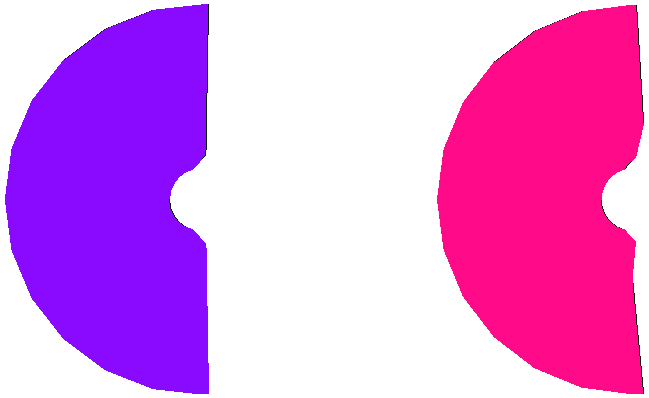

Figure A.11: The VELO R sensor (left) and the VELO ϕ sensor (right).

ϕ Sensor

The VELO ϕ sensor is slightly more complex than the R sensor. It is a union of half of a tube with four trapezoids to create the angled edge and is made from silicon. I added two subtractions to widen the circular cut as part of my improvements of the geometry description. The ϕ sensor can be seen in Fig. A.11 (right) and has a thickness of 0.3 mm and a mass in the geometry description of 2.14 g. The average mass at production was 2.096 g.

Hybrid

The VELO hybrid is made up from several elements, most of which are visible in Fig. A.12. The main part consists of a TPG graphite core that has a layer of carbon fibre on either side. Kapton circuits are placed on both sides and finally a thin layer of copper is used to model the numerous passive electronic components on each side. Semi-circular sections are used to represent pitch adapters and read out chips. The total mass of the hybrid, excluding the pitch adapters and read out chips, in the simulation is 54.364 g. The value at production was measured to be 49.2 ± 1.6 g.

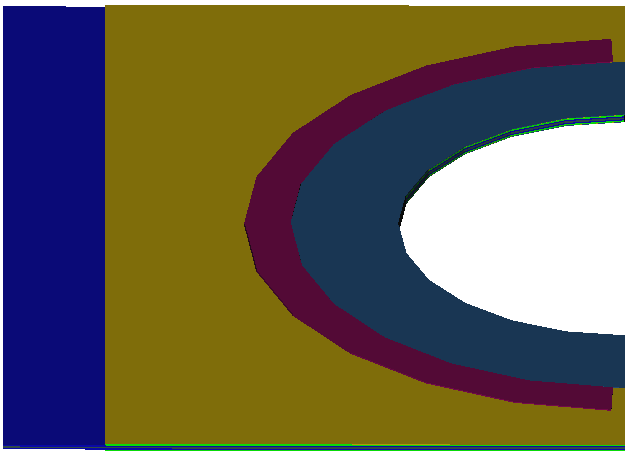

Figure A.12: The VELO hybrid showing the carbon fibre layer (blue), copper layer (yellow), read out chips (purple) and pitch adapters (grey-blue).

Paddle

The paddle is a carbon fibre structure that supports the VELO hybrid, and consists of many different volumes added together. The paddle is shown in Fig. A.13. The mass of the paddle in the geometry description is 43.340 g and was measured to be 43.9 ± 2.2 g at production.

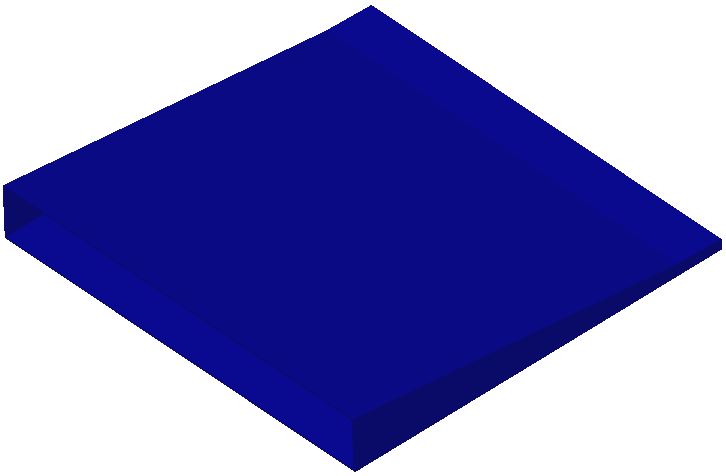

Figure A.13: The VELO paddle.

Base

The base connects the paddle to the constraint system and contains three sections, two Invar (steel with 36 % nickel content) feet and a carbon fibre centre. The base is shown in Fig. A.14 and has a mass in the simulation of 220.063 g which is much larger than the production value of 162.3 g.

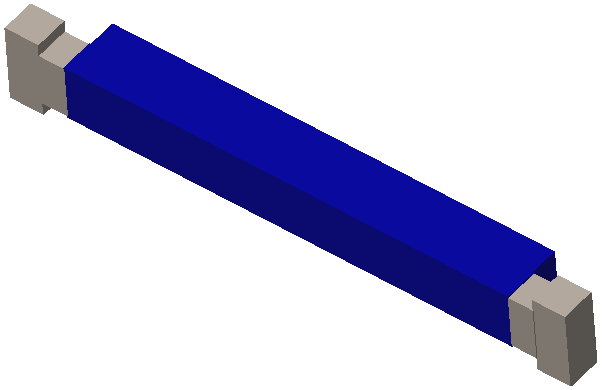

Figure A.14: The base of the VELO modules.

Kapton cables

The kapton cables are modelled as a single layer in the simulation because a more realistic description caused a significant slow down when executing the simulation. The single layer is an average of the true layered structure of the cables. The shape of the cables in the simulation can be seen in Fig. A.15. The mass of a single cable

in the geometry description is 13.529 g compared to an estimated production mass of approximately 13 g. The production mass is estimated because in reality the cables are much longer to route out of the VELO. I added the Kapton cables to the geometry description using schematic drawings to improve the simulation of the VELO modules.

Figure A.15: A VELO module Kapton cable.

Connector for Kapton cable

These connectors attach the Kapton cables to the VELO hybrid and consist of a liquid crystal polymer core and two beryllium-copper contacts. A connector is shown in Fig. A.16 and the simulated mass is 4.582 g. This compares favourably with the production mass of 4.55 ± 0.23 g. The connectors were added as a part of my work to improve the VELO geometry description.

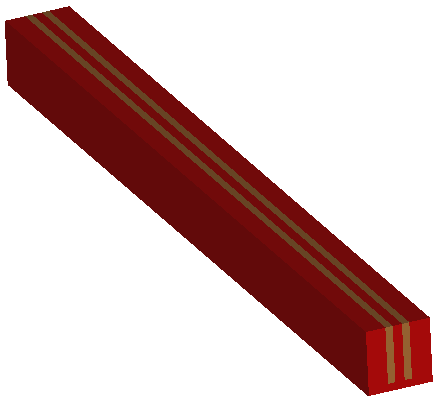

Figure A.16: The socket and plug to connect the cables to the hybrid.

A.2.4 Pile-up modules

The pile-up module volume contains the single R sensor, hybrid and support structures as shown in Fig. A.17. Everything, with the exception of the sensor, was added

as a part of my work to improve the simulated VELO detector description.

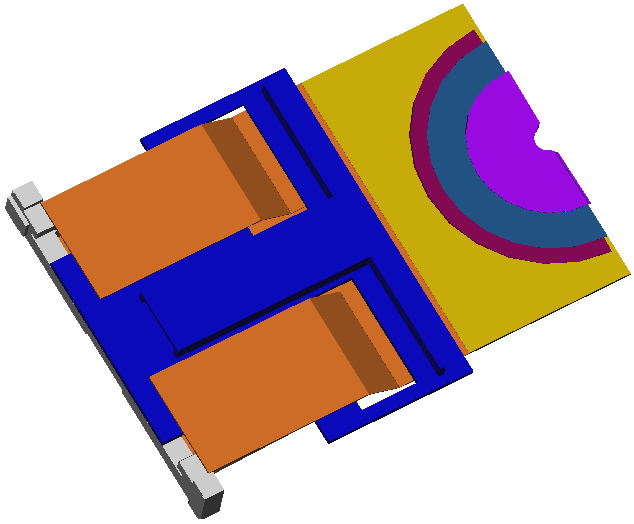

Figure A.17: A pile-up module showing the paddle (blue), base (grey), Kapton cables (orange), sensor (purple) and hybrid (yellow).

Pile-up Hybrid

The pile-up hybrid is almost identical to the VELO hybrid, Fig. A.12, but is missing the layers of kapton and copper on one side. An extra copper layer is included to account for a higher copper content with respect to the standard hybrid. The mass of the pile-up hybrid in the simulation is 45.668 g and while no production mass was available it should be well described as it is similar to the VELO hybrid. The pile-up hybrid was added by myself as part of my improvements to the geometry description.

Pile-up Paddle

The pile-up paddle is a support structure for the pile-up hybrids and consists of three sections, a base with holes in for the kapton cables to pass through and two braces as shown in Fig. A.18. The mass of the paddle in the database is 147.961 g and the production mass is not known. The pile-up paddle was another element that I added to the simulation.

Pile-up Base

The pile-up base is an aluminium structure that holds up the pile-up module. The base was added to the simulation as part of my work to improve the geometry

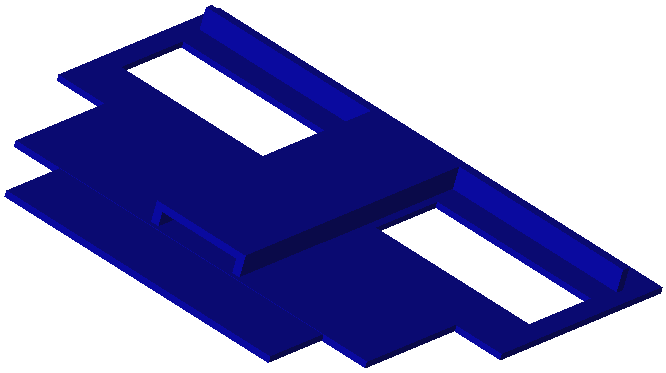

Figure A.18: The pile-up paddle.

description of the VELO from engineering schematics. Figure A.19 shows the base and it has a mass of 129.577 g in the simulation. The mass at production is not currently available.

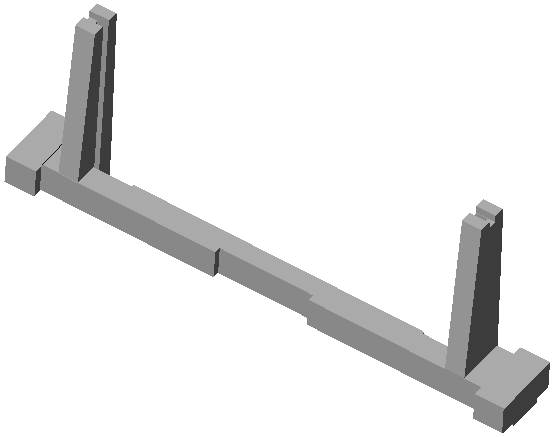

Figure A.19: The aluminium base of the pile-up modules.

Pile-up Cables

The pile-up Kapton cables come in two types, straight and bent, with two of each per pile-up module as shown in Fig. A.20. The mass of the four cables in the simulation is 51.885 g but no production mass is available. However, they are identical in structure to the VELO cables and so should be well described.

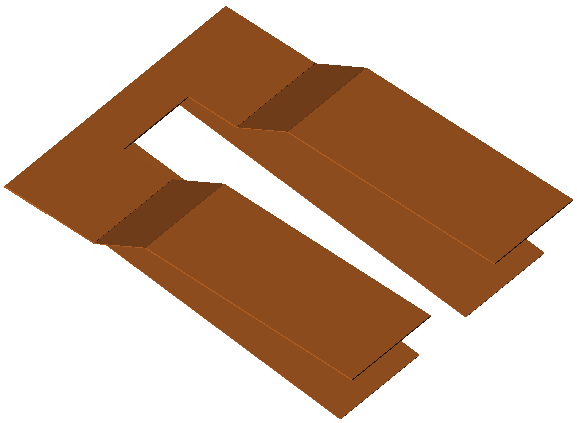

Figure A.20: The four Kapton cables on a pile-up module.

A.3 Material scan

The VELO geometry description is used in both the simulation and for real data to calculate effects such as multiple scattering. Therefore, it is important that the material in the geometry description agrees well with the actual VELO detector, at least inside the detector acceptance. To investigate the amount of material in the description, straight tracks from the interaction point were extrapolated through the VELO geometry description. It should be noted that these tracks were flatly distributed in pseudorapidity. The fraction of a radiation length seen by the track was calculated as it passed through the material.

The average material budget as a function of X_0 is shown for each VELO component in Fig. A.21. X_0 describes the average distance travelled by an electron to lose all but $1/e$ of its energy. Inside the LHCb acceptance the RF foil is the dominant contribution, providing 42.1 % of the VELO material seen by the tracks.

The amount of material seen by particles in the simulated VELO as a function of pseudorapidity, η, is shown in Fig.A.22. The average number of radiation lengths in the VELO is $0.217X_0$ for $1.6 < \eta < 4.9$. The peak at small η is mostly from the detector supports. Figure A.23 shows the material traversed by particles as a function of pseudorapidity and azimuthal angle, ϕ. The vertical structures are the RF foils and the black regions are from detector supports.

A.4 Summary

This appendix provides a brief summary of the geometry description of the VELO detector and the changes that I have made to it. For a more detailed review please

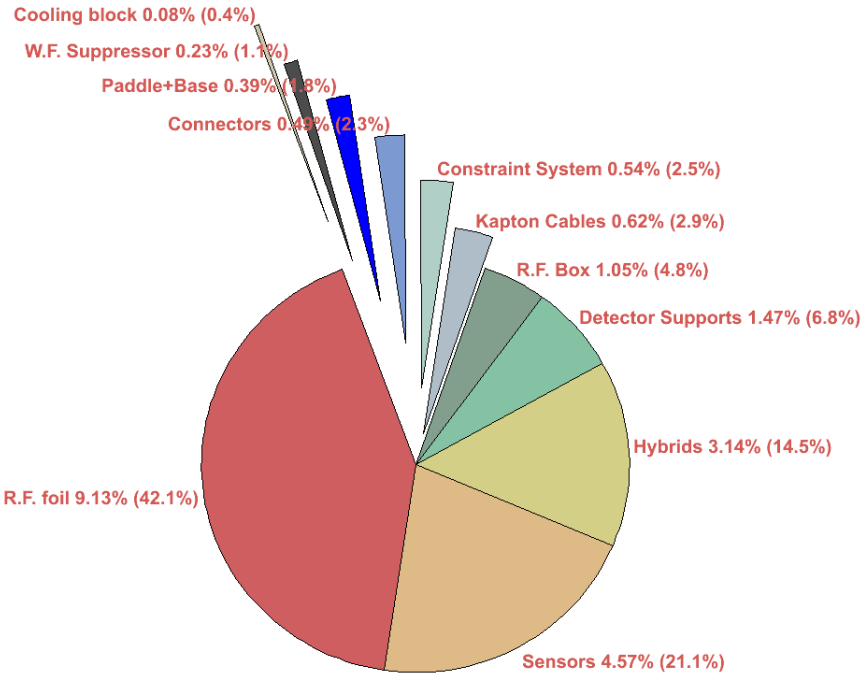

Figure A.21: The average material budget per component in the VELO as a percentage of X_0, with $1.6 < \eta < 4.9$. The numbers in brackets give this value as a percentage of the average VELO radiation length. The sum of the segments in the chart gives the total VELO material budget as $0.217X_0$. Reproduced from Ref. [98].

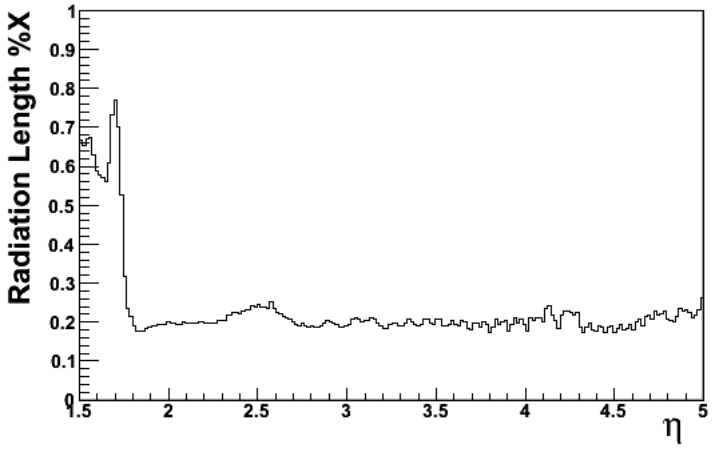

Figure A.22: Number of radiation lengths of material traversed by a particle passing through the VELO at a given value of pseudorapidity, η. Reproduced from Ref. [98].

see Ref. [98].

Table A.1 shows that there is, on average, a good agreement between masses

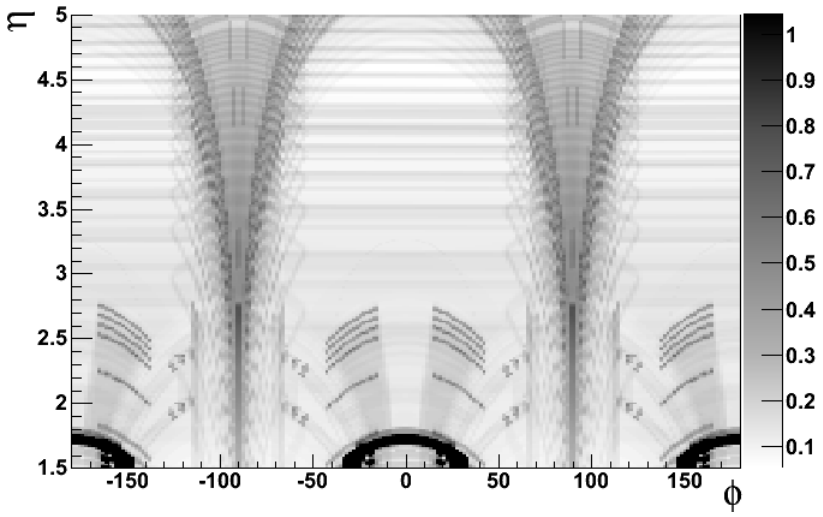

Figure A.23: Number of radiation lengths of material in the VELO as a two-dimensional function of pseudorapidity, η, and azimuthal angle, ϕ. Reproduced from Ref. [98].

in the simulation and in the real world. If all of the production masses had been available with uncertainties it may have looked better still. Some components of the geometry description show that there is still some work to be done to improve the database further following my changes. Following all of my updates the amount of material simulated in the VELO description is now $0.217X_0$.

Component	**Sim. Mass (g)**	**Mass (g)**	**Comments**
Wakefield Cone	13.22	38.7	Incomplete, see Sec. A.2.1
RF Box	4198.0	3899	No urgent problems
RF Foil	200.642	174	Not very good agreement
R Sensor	2.140	2.252	No urgent problems
Phi Sensor	2.140	2.096	No urgent problems
Hybrid	54.36	49.2 ± 1.6	Not bad agreement
Paddle	43.34	43.9 ± 2.2	Good agreement
Base	220.06	162.3	Not very good agreement
Kapton Cable	13.54	13	Estimate, see Sec. A.2.3
Connector	4.58	4.55 ± 0.23	Good agreement

Table A.1: A list of items in the VELO simulation comparing the simulated mass to the mass at production. Reproduced from Ref. [98].

Bibliography

[1] CDF collaboration, F. Abe et al., *Observation of top quark production in $\bar{p}p$ collisions*, *Phys. Rev. Lett.* **74** (1995) 2626–2631, [arXiv:hep-ex/9503002].

[2] D0 collaboration, S. Abachi et al., *Observation of the top quark*, *Phys. Rev. Lett.* **74** (1995) 2632–2637, [arXiv:hep-ex/9503003].

[3] DONUT collaboration, K. Kodama et al., *Observation of tau neutrino interactions*, *Phys. Lett.* **B504** (2001) 218–224, [arXiv:hep-ex/0012035].

[4] P. W. Higgs, *Broken Symmetries and the Masses of Gauge Bosons*, *Phys.Rev.Lett.* **13** (1964) 508–509.

[5] Particle Data Group, K. Nakamura et al., *Review of particle physics*, *J. Phys.* **G37** (2010) 075021.

[6] Nobel Prize in Physics, *http://www.nobelprize.org/nobel_prizes/physics/*, June 2012.

[7] R. Feynman and M. Gell-Mann, *Theory of Fermi interaction*, *Phys. Rev.* **109** (1958) 193–198.

[8] E. Sudarshan and R. Marshak, *Chirality invariance and the universal Fermi interaction*, *Phys. Rev.* **109** (1958) 1860–1860.

[9] T. Lee and C.-N. Yang, *Question of Parity Conservation in Weak Interactions*, *Phys. Rev.* **104** (1956) 254–258.

[10] C. Wu, E. Ambler, R. Hayward, D. Hoppes, and R. Hudson, *Experimental test of Parity Conservation in Beta Decay*, *Phys. Rev.* **105** (1957) 1413–1414.

[11] M. Gell-Mann and A. Pais, *Behavior of neutral particles under charge conjugation*, *Phys. Rev.* **97** (1955) 1387–1389.

[12] K. Lande, E. Booth, J. Impeduglia, L. Lederman, and W. Chinowsky, *Observation of Long-Lived Neutral V Particles*, *Phys. Rev.* **103** (1956) 1901–1904.

[13] J. Christenson, J. Cronin, V. Fitch, and R. Turlay, *Evidence for the 2 π decay of the K_L Meson*, *Phys. Rev. Lett.* **13** (1964) 138–140.

[14] W. Hou, *Source of CP Violation for the Baryon Asymmetry of the Universe*, *Int. J. Mod. Phys.* **D20** (2011) 1521–1532, [arXiv:1101.2161].

[15] BaBar collaboration, B. Aubert et al., *Observation of CP violation in the B^0 meson system*, *Phys. Rev. Lett.* **87** (2001) 091801, [arXiv:hep-ex/0107013].

[16] Belle collaboration, K. Abe et al., *Observation of large CP violation in the neutral B meson system*, *Phys. Rev. Lett.* **87** (2001) 091802, [arXiv:hep-ex/0107061].

[17] N. Cabibbo, *Unitary Symmetry and Leptonic Decays*, *Phys. Rev. Lett.* **10** (1963) 531–533.

[18] S. Glashow, J. Iliopoulos, and L. Maiani, *Weak Interactions with Lepton-Hadron Symmetry*, *Phys. Rev.* **D2** (1970) 1285–1292.

[19] M. Kobayashi and T. Maskawa, *CP-Violation in the Renormalizable Theory of Weak Interaction*, *Prog. Theor. Phys.* **49** (1973) 652.

[20] H. Yukawa, *On the interaction of elementary particles*, *Proc. Phys. Math. Soc. Jap.* **17** (1935) 48–57.

[21] L.-L. Chau and W.-Y. Keung, *Comments on the Parametrization of the Kobayashi-Maskawa Matrix*, *Phys. Rev. Lett.* **53** (1984) 1802.

[22] L. Wolfenstein, *Parametrization of the Kobayashi-Maskawa Matrix*, *Phys. Rev. Lett.* **51** (1983) 1945.

[23] C. Jarlskog and R. Stora, *Unitarity Polygons and CP Violation Areas and Phases in the Standard Electroweak Model*, *Phys. Lett.* **B208** (1988) 268.

[24] CKMfitter Group, J. Charles et al. *Eur. Phys. J.* **C41** (2005) 1–131. [hep-ph/0406184], updated results and plots available at: http://ckmfitter.in2p3.fr.

[25] R. Dalitz, *On the analysis of τ meson data and the nature of the τ meson*, *Phil. Mag.* **44** (1953) 1068–1080.

[26] LHCb collaboration, R. Aaij et al., *Search for CP violation in $D^+ \to K^-K^+\pi^+$ decays*, *Phys. Rev.* **D84** (2011) 112008, [arXiv:1110.3970].

[27] V. Anisovich and A. Sarantsev, *K matrix analysis of the $IJ^{PC} = 00^{++}$ wave in the mass region below 1900 MeV*, *Eur. Phys. J.* **A16** (2003) 229–258, [arXiv:hep-ph/0204328].

[28] I. Aitchison, *K-matrix formalism for overlapping resonances*, *Nucl. Phys.* **A189** (1972) 417–423.

[29] LHCb collaboration, *Road map for selected key measurements from LHCb*, Tech. Rep. LHCb-PUB-2009-029, CERN, Geneva, May, 2010.

[30] M. Gronau and D. London, *How to determine all the angles of the unitarity triangle from $B^0_d \to DK_S$ and $B^0_s \to D\phi$*, *Phys. Lett.* **B253** (1991) 483–488.

[31] M. Gronau and D. Wyler, *On determining a weak phase from CP asymmetries in charged B decays*, *Phys. Lett.* **B265** (1991) 172–176.

[32] D. Atwood, I. Dunietz, and A. Soni, *Enhanced CP violation with $B \to KD^0(\bar{D}^0)$ modes and extraction of the CKM angle γ*, *Phys. Rev. Lett.* **78** (1997) 3257–3260, [arXiv:hep-ph/9612433].

[33] BaBar collaboration, P. del Amo Sanchez et al., *Evidence for direct CP violation in the measurement of the Cabibbo-Kobayashi-Maskawa angle γ with $B^\mp \to D^{(*)}K^{(*)\mp}$ decays*, *Phys. Rev. Lett.* **105** (2010) 121801, [arXiv:1005.1096].

[34] Belle collaboration, A. Poluektov et al., *Evidence for direct CP violation in the decay $B \to D(*)K$, $D \to K_S\pi^+\pi^-$ and measurement of the CKM phase ϕ_3*, *Phys. Rev.* **D81** (2010) 112002, [arXiv:1003.3360].

[35] BaBar collaboration, P. del Amo Sanchez et al., *Measurement of CP observables in $B^\pm \to D_{CP}K^\pm$ decays and constraints on the CKM angle γ*, *Phys. Rev.* **D82** (2010) 072004, [arXiv:1007.0504].

[36] Belle collaboration, K. Abe et al., *Study of $B^\pm \to D_{CP}K^\pm$ and $D^*_{CP}K^\pm$ decays*, *Phys. Rev.* **D73** (2006) 051106, [arXiv:hep-ex/0601032].

[37] CDF collaboration, T. Aaltonen et al., *Measurements of branching fraction ratios and CP asymmetries in $B^\pm \to D_{CP}K^\pm$ decays in hadron collisions*, *Phys. Rev.* **D81** (2010) 031105, [arXiv:0911.0425].

[38] LHCb collaboration, *A measurement of the ratio of branching fractions:* $\frac{\mathcal{B}(B^\pm \to DK^\pm)}{\mathcal{B}(B^\pm \to D\pi^\pm)}$ *for* $D \to K\pi$, KK, $K\pi\pi\pi$ *and* $K^0_S\pi\pi$, . LHCb-ANA-2010-013; LHCb-ANA-2011-053.

[39] Heavy Flavor Averaging Group, D. Asner et al., *Averages of b-hadron, c-hadron, and* τ*-lepton Properties*, arXiv:1010.1589.

[40] S. Malde, *Charm inputs from CLEO-c for gamma measurements*, *PoS* **BEAUTY2011** (2011) 037.

[41] Belle collaboration, Y. Horii et al., *Evidence for the Suppressed Decay* $B^- \to DK^-, D \to K^+\pi^-$, *Phys. Rev. Lett.* **106** (2011) 231803, [arXiv:1103.5951].

[42] Babar collaboration, P. del Amo Sanchez et al., *Search for* $b \to u$ *transitions in* $B^- \to DK^-$ *and* $B^- \to D^*K^-$ *decays*, *Phys. Rev.* **D82** (2010) 072006, [arXiv:1006.4241].

[43] CDF collaboration, T. Aaltonen et al., *Measurements of branching fraction ratios and* CP*-asymmetries in suppressed* $B^- \to D(\to K^+\pi^-)K^-$ *and* $B^- \to D(\to K^+\pi^-)\pi^-$ *decays*, *Phys. Rev.* **D84** (2011) 091504, [arXiv:1108.5765].

[44] LHCb Collaboration, *Evidence for the suppressed decay* $B^\pm \to (K^\mp\pi^\pm)_D K^\pm$, .

[45] A. Giri, Y. Grossman, A. Soffer, and J. Zupan, *Determining* γ *using* $B^\pm \to DK^\pm$ *with multibody D decays*, *Phys. Rev.* **D68** (2003) 054018, [arXiv:hep-ph/0303187].

[46] J. Charles, A. Le Yaouanc, L. Oliver, O. Pene, and J. Raynal, $B^0_d(t) \to DPP$ *time-dependent Dalitz plots, CP violating angles* 2β, $2\beta + \gamma$, *and discrete ambiguities*, *Phys. Lett.* **B425** (1998) 375, [arXiv:hep-ph/9801363].

[47] T. Latham and T. Gershon, *A Method to Measure* $\cos(2\beta)$ *Using Time-Dependent Dalitz Plot Analysis of* $B^0 \to D_{CP}\pi^+\pi^-$, *J. Phys.* **G36** (2009) 025006, [arXiv:0809.0872].

[48] T. Gershon, *On the Measurement of the Unitarity Triangle Angle* γ *from* $B^0 \to DK^{*0}$ *Decays*, *Phys. Rev.* **D79** (2009) 051301, [arXiv:0810.2706].

[49] T. Gershon and M. Williams, *Prospects for the Measurement of the Unitarity Triangle Angle* γ *from* $B^0 \to DK^+\pi^-$ *Decays*, *Phys. Rev.* **D80** (2009) 092002, [arXiv:0909.1495].

[50] S. Nandi and D. London, *$B_s(\bar{B}_s) \to D^0_{CP} K\bar{K}$: Detecting and Discriminating New Physics in B_s–$\bar{B}_s$ Mixing*, arXiv:1108.5769.

[51] Belle collaboration, A. Kuzmin et al., *Study of $\bar{B}^0 \to D0\pi^+\pi^-$ decays*, *Phys. Rev.* **D76** (2007) 012006, [arXiv:hep-ex/0611054].

[52] BaBar collaboration, B. Aubert et al., *Measurement of branching fractions and resonance contributions for $B^0 \to \bar{D}^0 K^+\pi^-$ and search for $B^0 \to D^0 K^+\pi^-$ decays*, *Phys. Rev. Lett.* **96** (2006) 011803, [arXiv:hep-ex/0509036].

[53] BaBar collaboration, B. Aubert et al., *Search for $b \to u$ transitions in $B^0 \to D^0 K^{*0}$ decays*, *Phys. Rev.* **D80** (2009) 031102, [arXiv:0904.2112].

[54] BaBar collaboration, B. Aubert et al., *Search for $B^0 \to \phi(K^+\pi^-)$ decays with large $K^+\pi^-$ invariant mass*, *Phys. Rev.* **D76** (2007) 051103, [arXiv:0705.0398].

[55] BaBar collaboration, P. del Amo Sanchez et al., *Observation and study of the baryonic B-meson decays $B \to D^{(*)} p\bar{p}\,(\pi)(\pi)$*, arXiv:1111.4387.

[56] LHCb Collaboration, R. Aaij et al., *First observation of the decay $\bar{B}^0_s \to D^0 K^{*0}$ and a measurement of the ratio of branching fractions $\frac{\mathcal{B}(\bar{B}^0_s \to D^0 K^{*0})}{\mathcal{B}(\bar{B}^0 \to D^0 \rho^0)}$*, *Phys. Lett.* **B706** (2011) 32–39, [arXiv:1110.3676].

[57] Belle collaboration, A. Drutskoy et al., *Observation of $B \to D^{(*)} K^- K^{(*)0}$ decays*, *Phys. Lett.* **B542** (2002) 171–182, [arXiv:hep-ex/0207041].

[58] LHCb collaboration, J. Alves, A. Augusto et al., *The LHCb Detector at the LHC*, *JINST* **3** (2008) S08005.

[59] L. Evans and P. Bryant, *LHC Machine*, *JINST* **3 S08001** (2008).

[60] European Organization for Nuclear Research CERN, *http://public.web.cern.ch/public/*, March 2011.

[61] DELPHI Experiment, *http://delphiwww.cern.ch/*, March 2011.

[62] ATLAS collaboration, G. Aad et al., *The ATLAS Experiment at the CERN Large Hadron Collider*, *JINST* **3** (2008) S08003.

[63] CMS collaboration, S. Chatrchyan et al., *The CMS experiment at the CERN LHC*, *JINST* **3** (2008) S08004.

[64] ALICE collaboration, K. Aamodt et al., *The ALICE experiment at the CERN LHC*, *JINST* **3** (2008) S08002.

[65] LHC Programme Coordination, *http://lpc.web.cern.ch/lpc/*, February 2012.

[66] Linear Accelerator LINAC2, *http://linac2.home.cern.ch/linac2/default.htm*, March 2011.

[67] Proton Synchrotron Booster, *http://psb-machine.web.cern.ch/psb-machine/*, March 2011.

[68] Proton Synchrotron, *http://public.web.cern.ch/public/en/research/PS-en.html*, March 2011.

[69] Super Proton Synchrotron, *http://public.web.cern.ch/public/en/research/SPS-en.html*, March 2011.

[70] LHC public page, *http://public.web.cern.ch/public/en/research/AccelComplex-en.html*, February 2012.

[71] CERN Bulletin online article, *https://cdsweb.cern.ch/journal/CERNBulletin/2011/41/News%20Articles/1387895?ln=en*, February 2012.

[72] LHCb collaboration, *LHCb RICH: Technical Design Report*. Technical Design Report LHCb. CERN, Geneva, 2000.

[73] LHCb collaboration, *LHCb inner tracker: Technical Design Report*. Technical Design Report LHCb. CERN, Geneva, 2002.

[74] LHCb collaboration, *LHCb calorimeters: Technical Design Report*. Technical Design Report LHCb. CERN, Geneva, 2000.

[75] LHCb collaboration, *Hlt website http://lhcb-trig.web.cern.ch/lhcb-trig/HLT/HltDescription.htm*, March 2011.

[76] V. V. Gligorov, *A single track hlt1 trigger*, Tech. Rep. LHCb-PUB-2011-003, CERN, Geneva, Jan, 2011.

[77] R. Fruhwirth, *Application of Kalman filtering to track and vertex fitting*, *Nucl.Instrum.Meth.* **A262** (1987) 444–450.

[78] V. Gligorov, C. Thomas, and M. Williams, *The HLT inclusive B triggers*, Tech. Rep. LHCb-PUB-2011-016, CERN, Geneva, Sep, 2011. LHCb-INT-2011-030.

[79] G. Haefeli et al., *The LHCb DAQ interface board TELL1*, *Nucl. Instrum. Meth.* **A560** (2006) 494–502.

[80] M. Adinolfi, *System test of a three-column LHCb RICH-2 prototype detector*, *Nucl.Instrum.Meth.* **A553** (2005) 328–332.

[81] T. Sjostrand, S. Mrenna, and P. Z. Skands, *PYTHIA 6.4 Physics and Manual*, *JHEP* **0605** (2006) 026, [arXiv:hep-ph/0603175].

[82] D. Lange, *The EvtGen particle decay simulation package*, *Nucl. Instrum. Meth.* **A462** (2001) 152–155.

[83] Warwick EvtGen group, *http://evtgen.warwick.ac.uk/*, February 2012.

[84] GEANT4 collaboration, S. Agostinelli et al., *GEANT4: A Simulation toolkit*, *Nucl. Instrum. Meth.* **A506** (2003) 250–303.

[85] R. Brun and F. Rademakers, *ROOT: An object oriented data analysis framework*, *Nucl. Instrum. Meth.* **A389** (1997) 81–86.

[86] F. Alessio, *Overview of the lhcb experiment status and results*, .

[87] M. Feindt and U. Kerzel, *The NeuroBayes neural network package*, *Nucl. Instrum. Meth.* **A559** (2006) 190–194.

[88] M. Feindt, *A Neural Bayesian Estimator for Conditional Probability Densities*, *ArXiv Physics e-prints* (Feb, 2004) [physics/0].

[89] M. Pivk and F. R. Le Diberder, *SPlot: A Statistical tool to unfold data distributions*, *Nucl. Instrum. Meth.* **A555** (2005) 356–369, [arXiv:physics/0402083].

[90] Laura++ Dalitz plot fitting package, University of Warwick, documentation in preparation.

[91] W. Verkerke and D. P. Kirkby, *The RooFit toolkit for data modeling*, *eConf* **C0303241** (2003) MOLT007, [arXiv:physics/0306116].

[92] LHCb collaboration, R. Aaij et al., *Measurement of b hadron production fractions in 7 TeV pp collisions*, *Phys. Rev.* **D85** (2012) 032008, [arXiv:1111.2357].

[93] Belle collaboration, A. Kuzmin et al., *Study of $\bar{B}^0 \to D^0\pi^+\pi^-$ decays*, *Phys. Rev.* **D76** (2007) 012006, [arXiv:hep-ex/0611054].

[94] BaBar collaboration, P. del Amo Sanchez et al., *Dalitz-plot Analysis of* $B^0 \to \bar{D}^0\pi^+\pi^-$, arXiv:1007.4464.

[95] LHCb collaboration, R. Aaij et al., *Determination of* f_s/f_d *for* $7TeV/c^2$ *pp collisions and a measurement of the branching fraction of the decay* $B_d \to D^-K^+$, *Phys. Rev. Lett.* **107** (2011) 211801, [arXiv:1106.4435].

[96] LHCb collaboration, R. Aaij et al., *Observation of* CP *violation in* $B^+ \to DK^+$ *decays*, arXiv:1203.3662.

[97] LHCb collaboration, R. Aaij et al., *Measurements of the branching fractions of the decays* $B_s^0 \to D_s^{\mp}K^{\pm}$ *and* $B_s^0 \to D_s^-\pi^+$, arXiv:1204.1237.

[98] M. Whitehead, T. Latham, and T. Gershon, *Vertex locator simulated material description*, Tech. Rep. LHCb-INT-2010-054, CERN, Geneva, Oct, 2010.